ISBN 978-82-326-4582-4 (printed version)
ISBN 978-82-326-4583-1 (electronic version)
ISSN 1503-8181

Doctoral theses at NTNU, 2020:117

Karl Oskar Pires Bjørgen

Optical Study of Soot Characteristics of Biofuel Spray Combustion

Doctoral Thesis

Karl Oskar Pires Bjørgen

NTNU
Norwegian University of
Science and Technology
Faculty of Engineering
Department of Energy and Process Engineering

NTNU
Norwegian University of
Science and Technology

Doctoral theses at NTNU, 2020:117

NTNU

NTNU
Norwegian University of
Science and Technology

Karl Oskar Pires Bjørgen

Optical Study of Soot Characteristics of Biofuel Spray Combustion

Thesis for the degree of Philosophiae Doctor

Trondheim, March 2020

Norwegian University of Science and Technology
Faculty of Engineering
Department of Energy and Process Engineering

NTNU
Norwegian University of
Science and Technology

NTNU
Norwegian University of Science and Technology

Thesis for the degree of Philosophiae Doctor

Faculty of Engineering
Department of Energy and Process Engineering

ISBN 978-82-326-4582-4 (printed version)
ISBN 978-82-326-4583-1 (electronic version)
ISSN 1503-8181

Doctoral theses at NTNU, 2020:117

Printed by Skipnes Kommunikasjon as

Preface

The presented doctoral work was carried out at the Norwegian University of Science and Technology (NTNU) in Trondheim during the period of 2015-2019. Prof. Terese Løvås has been the main supervisor of the work, and Dr. David Robert Emberson has been the co-supervisor.

The position has been partially funded by Nordic Five Tech, which is a strategic alliance of the five leading technical universities in Denmark, Finland, Norway and Sweden. The conducted work has also been part of the center for environmental research Bio4fuels.

Abstract

Liquid biofuels for internal combustion engines will likely be part of the future solution for mitigating CO_2 emissions to the atmosphere. Several types of biofuels for compression ignition (CI) engines are being developed at the moment, made from sustainable feedstock such as waste animal fat, forest residue and algae. These fuels will only reach the consumer market if they become economically viable and meet the requirements set by authorities for fuel quality and hardware compatibility. Additionally, issues related to pollutant emissions of particulate matter and nitric oxides from CI engines must be considered, where advanced aftertreatment systems have been developed in order to comply to regulations. Particle matter emissions from CI engines poses a considerable challenge since expensive aftertreatment systems are needed and can over time reduce engine performance. By introducing biofuels, an opportunity to reduce the particulate emissions is offered. Biofuels can be designed to have low sooting tendencies and favorable combustion properties, such that clean combustion can be achieved. Biofuels can also be blended to diesel fuel gradually, where both well-to-wheel CO_2 emissions and pollutant emissions can be reduced. In order to achieve this, research needs to be conducted on combustion and emission characteristics of existing and novel biofuels.

An experimental suite has been developed, enabling detailed investigations on combustion and soot processes in CI engines fueled with biofuels. A redesigned engine with optical access to the combustion chamber has been commissioned, i.e. the optically accessible compression ignition chamber (OACIC), which enables direct optical measurements of a single CI spray. The OACIC is a reciprocating rapid compression machine designed to perform fuel comparison studies, allowing for fast fuel switching and high speed data acquisition. The intake air is heated and compressed, offering a range of engine-like thermodynamic conditions.

For the current work, the optical technique diffuse back-illuminated extinction imaging (DBIEI) of soot has been applied to the OACIC. The technique measures the optical density of in-flame soot, which can be related to the soot mass and concentration. Further development of the technique has been performed, including an improved method for correcting the flame luminosity interference on the measurement. Uncertainties related to beam steering have also been assessed in detail, which led to minimization of these effects in the current setup. In addition, a framework for dealing with non-ideal camera characteristics which occurs when subjecting an image sensor for rapid high and low light intensities has been developed and adapted to the DBIEI measurement. By combining DBIEI and high speed OH^* chemiluminescence imaging, in-flame soot and flame lift-off length

were simultaneously measured, providing information about in-flame soot mass and jet air entrainment. These measurements together offer detailed information on soot production, which can be used to validate numerical simulations and to help elucidate the complex processes behind soot formation and oxidation.

The experimental suite was applied to the investigation of combustion of biofuels:

An experimental study on in-flame soot in CI sprays of biodiesel surrogate fuels was conducted. The surrogate fuels in subject were methyl oleate, methyl decanoate, *n*-heptane and a 50/50% molar blend of *n*-heptane and methyl decanoate. One of the objectives of the study was to compare the surrogates to a commercially available rapeseed methyl ester (RME) biodiesel. In this way, a direct evaluation of the combustion and sooting characteristics was enabled. The sooting tendency and combustion characteristics of methyl oleate are similar to that of RME, since the major component in RME is methyl oleate. Methyl decanoate was observed to have a very low sooting tendency, which is explained by its high oxygen content. Methyl oleate proved to be a fitting surrogate fuel for biodiesel. However, the kinetic reaction mechanism for methyl oleate is very complex and computationally expensive. This makes methyl decanoate based surrogate fuels more fitting, since they have similar combustion chemistry to that of RME, due to the ester moiety.

Soot and combustion characteristics of hydrotreated vegetable oil (HVO), RME and diesel fuel were measured in the OACIC. The study showed that diesel fuel produced the highest level of in-flame soot, while HVO and RME produced similar levels. The higher in-flame soot concentration observed for diesel fuel was explained by its aromatics content. HVO produced slightly more in-flame soot than RME, which was likely due to the lack of fuel-bound oxygen in HVO.

An investigation of the possible utilization of glycerol as a soot-reducing additive in diesel fuel has been conducted, including experimental and numerical work. Glycerol is a byproduct of the biodiesel production process, where a possible value stream would be to sell it directly as a fuel additive. The main advantage of using glycerol as a fuel is its high oxygen content, potentially reducing particulate emissions. However, the disadvantages of having a low reactivity, high viscosity, and being immiscible with diesel fuel were uncovered. Adding glycerol to diesel resulted in an observed increase of the carbon monoxide concentration in the exhaust, which was due to glycerol's low reactivity. In addition, a decrease in particulate matter emissions and in-flame soot was observed. Numerical simulations showed a reduction of soot precursors and an increase in CO concentration after adding glycerol to *n*-heptane. The reduction in soot precursors is explained by the added oxygen to the fuel.

Acknowledgements

I would like to thank my supervisor Professor Terese Løvås for giving me the opportunity to develop as a researcher. Your guidance and knowledge has truly helped me reach my goals. I appreciate your enthusiasm for scientific work, and of course your great sense of humor, making every coffee meeting joyful.

My greatest gratitude is to be given David Emberson, who I have had a great time with throughout my PhD, both as a colleague and a friend. We have probably discussed and solved a million problems together, and I will definitely miss those "carefree" days we had in the lab listening to your weird music.

I am very grateful to have been part of a wonderful research group such as Comkin, consisting of hardworking, caring, smart and fun people. Christoph: the Norwegian speaking Italian with a German accent. Thanks for all the loooong and interesting conversations, and of course all the weightlifting to our favorite CD. Fredrik: the mathematician, the family man, the skier, the hobo, the spy; a man with many sides. Thanks for all the times you sneaked up on me while I was peacefully working in my office. Ning: a living legend and a quote generator, "be efficient". Thank you for reminding me that there is more in life than personal relationships. Tian: the prince and rightful heir of Comkin. Thank you for all the interesting discussions, your interest is really limitless. Jingyuan: thank you for the interesting conversations and for teaching me some Chinese. Corinna: thank you for appointing me lunch break boss and for reestablishing coffee routines. Michał: it has been great having you as a colleague, I especially enjoy hearing about the amount of firewood you have in Trolla. Ahfaz: thanks for all those meaningful and meaningless conversations, it has been wonderful sharing office with you. I hope to see you on a beach in San Diego in 40 years, be there. Kathrin: from not joining for lunch in the beginning, to becoming the most popular Comkin member. Thank you for standing together with me as a fellow experimentalist against the modelers, and for giving advises on anything I may ask for. Jonas: I am grateful that I got to know you below 23°C, where you are a very pleasant person to be with.

For the extended Comcake++ group, including Matias, Vladimir, Lorenzo, Luca, Silje, Donghoi and Shareq, Florian and Jan, I am happy to have had so many nice moments together with you, including barbecues, Christmas dinners and countless lunches.

Lastly, I wish to thank my beloved Ingrid for her love, patience, and for always supporting me.

Scientific contributions

Selected articles

This thesis is based on the work presented in the following articles:

I. Karl Oskar Pires Bjørgen, David Robert Emberson, Terese Løvås.
Diffuse Back-Illuminated Extinction Imaging of Soot: Effects of Beam Steering and Flame Luminosity.
Published in SAE Technical Paper Series (15.1.2019)

II. Karl Oskar Pires Bjørgen, David Robert Emberson, Terese Løvås.
Optical Measurements of In-Flame Soot in Compression-Ignited Methyl Ester Flames.
Published in Energy and Fuels (5.7.2019)

III. Karl Oskar Pires Bjørgen, David Robert Emberson, Terese Løvås.
Combustion and Soot Characteristics of Hydrotreated Vegetable Oil Compression-Ignited Spray Flames.
Submitted to Fuel (9.12.2019)

IV. David Robert Emberson, Jan Wyndorps, Ahfaz Ahmed, Karl Oskar Pires Bjørgen, Terese Løvås.
Detailed Examination of the Combustion of Diesel/Glycerol Emulsions in a Compression Ignition Engine.
Submitted to Fuel (24.3.2020)

The author's contribution to the selected articles

The author has performed the following work for each selected publication:

I. Bjørgen has developed the methodology, conducted the experiments and written the manuscript. Dr. Emberson has provided scientific guidance and assisted with the experiments. Prof. Løvås has been a scientific advisor throughout the work and provided valuable feedback on the manuscript.

II. Bjørgen has designed the scientific outline of the study, performed the experimental campaign, developed post-processing tools used for the analysis, and written the manuscript. Dr. Emberson has been a scientific advisor and assisted with his experimental expertise. Prof. Løvås has contributed with scientific discussions in the early and late phases of the work.

III. Bjørgen has performed the scientific analysis and discussion of this work. Bjørgen has also conducted the experiments. Dr. Emberson has assisted scientifically to both the discussion and to the experimental campaign. Prof. Løvås has been a scientific advisor of this work and assisted with the outline of the manuscript.

IV. The early phase design of this scientific study has been developed by Dr. Emberson, Dr. Ahmed and Wyndorps. Wyndorps conducted the experimental campaign and analysis of this work under the supervision of Dr. Emberson and Bjørgen, as part of his Master thesis. Dr. Ahmed conducted the kinetic study and the analysis. Bjørgen has contributed to the post-processing of the optical results, and provided scientific feedback on the final manuscript. Prof. Løvås has been a scientific advisor of the work. Dr. Emberson and Dr. Ahmed coordinated the writing of the manuscript.

Additional contributions

In addition to the publications selected for this thesis, several other scientific contributions have been made during the doctoral education:

- Vladimir Krivopolianskii, **Karl Oskar Pires Bjørgen**, David Robert Emberson, Sergey Ushakov, Vilmar Æsøy, Terese Løvås. *Experimental Study of Ignition Delay, Combustion, and NO Emission Characteristics of Hydrogenated Vegetable Oil.*
  Published in SAE International Journal of Fuels and Lubricants (1.2.2019)

- **Karl Oskar Pires Bjørgen**. *Diffuse Back-Illuminated Extinction Imaging of Soot: Effects of Beam Steering and Flame Luminosity.* SAE International Powertrains, Fuels and Lubricants. USA, San Antonio. September 2018 (oral presentation).

- **Karl Oskar Pires Bjørgen**. *Diffuse Back-illuminated Imaging of Soot in an Optical Reciprocating Rapid Compression Machine.* Nordic Flame Days. Sweden, Stockholm. October 2017 (oral presentation).

- David Emberson, **Karl Oskar Pires Bjørgen**, Terese Løvås. *Arctic Biodiesel Performance and PM Number Emissions.* International Conference on Modeling and Diagnostics for Advanced Engine Systems (COMODIA). Japan, Okayama. Juli 2017 (conference article).

- **Karl Oskar Pires Bjørgen**, David Robert Emberson, Terese Løvås. *Detailed In-Flame Soot Characteristics of Diesel, HVO and FAME Using Extinction Imaging.* 37th International Symposium on Combustion. Ireland, Dublin. July 2018 (visual presentation).

- **Karl Oskar Pires Bjørgen**, David Emberson. *Soot Characterization: Combined Sampling and Optical Techniques*. Thermo and Fluid Dynamic Processes in Direct Injection Engines (THIESEL). Spain, Valencia. September 2018 (visual presentation).

- **Karl Oskar Pires Bjørgen**, David Emberson. *Assessment of L.E.D Diffused Backilluminated Soot Extinction to Use in Reciprocating Rapid Compression Machine*. 8th European Combustion Meeting. Croatia, Dubrovnik. April 2017 (visual presentation).

- **Karl Oskar Pires Bjørgen**, David Emberson. *A Novel Optical Experimental Suite for CI Combustion Characterization*. Thermo and Fluid Dynamic Processes in Direct Injection Engines (THIESEL). Spain, Valencia. September 2016 (visual presentation).

- **Karl Oskar Pires Bjørgen**, David Robert Emberson, Terese Løvås. *Combustion Characterization of Second-generation Biofuels for Arctic Conditions in Compression-ignition Engines.* 36th International Symposium on Combustion. South Korea, Seoul. July 2016 (visual presentation).

Contents

Abbreviations and Symbols

Abbreviations

AHRR	Apparent heat release rate
ASTM	American Society for Testing and Materials
BSFC	Brake specific fuel consumption
BTL	Biomass-to-liquid
CAD	Crank angle degree
CFD	Computational fluid dynamics
CFR	Cooperative fuel research
CI	Compression ignition
CR	Compression ratio
CVV	Constant volume vessel
DBIEI	Diffuse back-illuminated extinction imaging
DBM	Dibutyl maleate
DPF	Diesel particulate filter
ECN	Engine Combustion Network
EGR	Exhaust gas recirculation
EN	European Standard
FAME	Fatty acid methyl ester
FLOL	Flame lift-off length
FT	Fischer-Tropsch
FWHM	Full width half mean
GTL	Gas-to-liquid
HACA	Hydrogen abstraction C_2H_2 addition
HP	*n*-heptane
HTL	Hydrothermal liquefaction
HVO	Hydrotreated vegetable oil
IDT	Ignition delay time
IEA	International Energy Agency
IQT	Ignition quality tester
IVC	Intake valve closing
LED	Light emitting diode
LIF	Laser induced fluorescence
LTC	Low temperature combustion
MD	Methyl decanoate
MO	Methyl oleate
NTNU	Norges Teknisk-Naturvitenskaplige Universitet
OACIC	Optically accessible compression ignition chamber
OD	Optical density
OEM	Original equipment manufacturer
PAH	Polycyclic aromatic hydrocarbon

PDF	Probability density function
PID	Proportional integral derivative
PLII	Planar laser induced incandescence
PM	Particulate matter
PPCI	Partially-premixed compression ignition
RCM	Rapid compression machine
RME	Rapeseed methyl ester
SAE	Society of automotive engineers
SCR	Selective catalytic reduction
SI	Spark-ignition
TC	Thermocouple
TDC	Top dead center
THC	Total hydrocarbon
TPGME	Tripropylene glycol methyl ether
TSI	Threshold sooting index
UHC	Unburned hydrocarbon
UV	Ultraviolet
YSI	Yield sooting index

Symbols

$(A/F)_{st}$	Stoichiometric air-fuel mass ratio (-)
λ	Wavelength (m)
$\overline{\phi}$	Cross-sectional averaged equivalence ratio (-)
ρ_a	Ambient gas density (kg m^{-3})
ρ_f	Fuel density (kg m^{-3})
τ	Transmittance (-)
τ_H	Jet ignition delay time (s)
θ	Spray spreading angle ($^\circ$)
C_a	Nozzle area contraction coefficient (-)
D	Thermal diffusivity (m^2 s^{-1})
d	Nozzle orifice diameter (m)
f_v	Soot volume fraction (-)
H	Flame lift-off length (m)
I_0	Incident light intensity (-)
I_f	Flame luminosity intensity (-)
I_t	Transmitted light intensity (-)
K	Path-averaged dimensional extinction coefficient (m^{-1})
k	Local dimensional extinction coefficient (m^{-1})
k_e	Dimensionless extinction coefficient (-)
KL	Soot optical density (-)
L	Path length (m)
n	Polytropic coefficient (-)
P	Ambient gas pressure (Pa)

S_L	Laminar flame velocity (m s^{-1})	x	Axial distance from nozzle (m)
T_a	Ambient gas temperature (K)	x^+	Characteristic spray length scale (m)
U	Jet exit velocity (m s^{-1})	Z_{st}	Stoichiometric fuel mixture fraction (-)
V	Volume (m^3)		

1. Introduction

The world is in need of CO_2 neutral energy resources and technologies in order to replace petroleum-based fuels. The combined CO_2 emissions in 2016 from passenger car vehicles and road freight transport made up 18.3% of the total CO_2 emissions coming from fuel combustion [64]. In order to reduce the CO_2 emissions in the automotive sector, introduction of biofuels in internal combustion engines has been a major focus area over the past decade [12]. In 2017, biofuel production reached 143 billion litres, which equated to around 3% of the global fuel production [62]. The biofuel production was mainly composed of bioethanol and biodiesel, although hydrotreated vegetable oil (HVO) has gained in popularity over the recent years, accounting for 14% of the combined biodiesel and HVO production in 2017 [62].

Replacing petroleum-based fuels with biofuels for the existing car fleet is an effective way of reducing the CO_2 emissions in the automotive sector [67], although life cycle assessments of biofuels are hard to perform and usually impose large uncertainties [43]. For example, when considering the production of bioethanol and biodiesel, their environmental impacts are dependent on the production and utilization of their by-products. When not using these resources, their environmental impact can be similar to their petroleum equivalents [49]. In addition to the well-to-wheel CO_2 emissions from biofuels, the economical aspect plays an important role. The prices of biofuels must be competitive with regards to their petroleum-based equivalents, which is especially hard to achieve during periods with low oil prices. Additionally, the production of biodiesel and bioethanol is mainly from food-based feedstocks which require land area. This has shown to increase food prices in the local region, which is not sustainable in the long run [5]. The positive environmental impact of biofuels is higher if non-food feedstock is used, also known as advanced biofuels or second-generation biofuels [145]. Advanced biofuel is mainly based on sustainable feedstock such as municipal solid waste and forestry, which is in large abundance in many countries.

The worldwide production of biofuel is expected to increase in the coming years, but the latest reports show that the increase per year is lower than expected [62]. Forecasts made by the International Energy Agency (IEA) for year 2023 predict that 4% of the energy demand in the transport sector will be represented by biofuels, which corresponds to 90% of the renewable energy used in the transport sector. Biodiesel and HVO will make up one-third of the biofuel production growth, while fuels such as bioethanol will make up the rest. The increased production of biofuels will mainly be driven by Brazil, China and India after having announced large investment plans for biofuel production in 2020. However, in the same period, Europe is expected to reduce its biofuel share due to weaker policy support for conventional biofuels. In the future energy outlook, only sustainable biofuels are included, which will require increased investments and policies on advanced biofuels. However, the predictions point towards that production of advanced biofuels are expected to remain low, accounting for only 1% of biofuel production in 2023. Despite stronger policy support, slow development is mainly due to technical difficulties and high production costs, forcing existing plants to stop production.

In Norway, an explosive increase in the number of light duty electrical vehicles (EVs) has been observed from 2013 [63]. In 2018, 46% of new cars sold in Norway were EVs, having the highest market share in the world. This increase is mainly a result of government policies on tax reduction and other benefits for electrical car owners in Norway. So, why focus on combustion of biofuels in the automotive sector, when the internal combustion engine vehicles are being replaced by EVs? Firstly, the EVs sold are almost exclusively light duty vehicles, where heavy duty EVs are not expected to be rolled out in a large scale any time soon, as they are still facing challenges connected to the electrical infrastructure, vehicle weight and time required for charging/swapping batteries[1] [2]. Secondly, the electrical power that drives the EVs should be of low CO_2 emissions, which is not the case for most countries today. Lastly, CO_2 emission reductions are needed as soon as possible, where developing countries will not likely increase the electrical share in their car fleet in near future, and even if they did, the energy powering the EVs would not likely be of low carbon origin. For heavy duty vehicles, introducing biofuels to the existing car fleet is a relatively quick solution for reducing CO_2 emissions. In the future, a combination of EVs and hybrid vehicles running on non-fossil fuels, e.g. biofuels in internal combustion engines, will therefore play a key role in the CO_2 reduction scheme of the transport sector, where the vehicle benefits from advantages of both technologies [128].

The well known and biggest challenge related to internal combustion engines is

[1] complete charging of a 300 kWh battery medium-freight truck takes six hours with DC fast charging at 50 kW [63].

the emission of pollutants, where cities today are facing serious problems related to poor air quality, affecting the population's health (e.g. New Delhi, India [65]). Hence, research on alternative fuels and internal combustion engines are needed for dealing with these issues.

The internal combustion engine

The compression ignition (CI) engine was invented by the French-German engineer Rudolph Diesel in the late 19th century. The first CI engine was a four-stroke engine with a vertical single cylinder. Diesel stated in 1912 that "a remarkable fact is that the first diesel engines, built in 1896-1897, are still working, without any change in their fuel consumption", giving an early indication that the diesel engine was a durable technology [28], see Figure 1.1. The first CI engines ran mainly on oils, both petroleum and bio-based. During the Paris exhibition in 1900, a small diesel engine was presented running on Arachis oil (peanut and earth-nut oil), which according to Diesel ran so smoothly that few people actually were aware of it. At the time, Diesel predicted that vegetable oils might become important in the future saying that "motor power can still be produced from the heat of the sun, which is always available for agricultural purposes, even when all our natural stores of solid and liquid fuels are exhausted". One of his key arguments for using bio-oils was that colonies could be independent from importation of petroleum oils. Some years before the introduction of the CI engine, the spark ignition (SI) engine was invented. The SI engine was lighter than the CI engine at the time, making it more suitable for use in aviation, while the CI engine became widely used for power generation or in ships due to its higher thermal efficiency.

Over the past century, SI and CI engines have constantly been developed and improved, where the main focus has been on increasing thermal efficiency and reducing pollutant emissions. The main driver for reducing the specific fuel consumption in engines has been sudden increases of the oil price, while today, the largest concern is the climate change caused by atmospheric CO_2. The main reason for choosing CI engines over SI engines is the higher compression ratio (CR) achieved in CI engines. In a SI engine, the compression ratio is limited by knock and throttling losses [51]. Knock occurs when the premixed air-fuel mixture autoignites before reaching top dead center (TDC), resulting in a limit to the maximum compression ratio that can be used, which in turn results in a lower thermodynamic efficiency. In a CI engine this is avoided since fuel is directly injected close to TDC and autoignites after mixing with the ambient gas in the chamber.

However, there are major drawbacks of CI engines as well. The injected fuel is only partially mixed with the air, forming local fuel-rich regions in the flame, which lead to soot formation. The soot is further oxidized in a high temperature

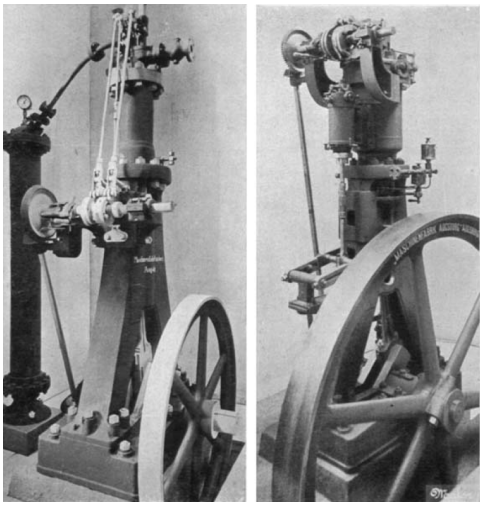

Figure 1.1: Left: first experimental diesel engine, 1893. Right: later experimental design 1895-96. [28]

mixing-controlled flame, where NO_x is produced [26]. The production of NO_x is mainly formed via the thermal Zeldovich mechanism [166], where the production rate exponentially increases with temperature. In an SI engine, the near stoichiometric premixed gas is ignited by a spark, where the flame burns volumetrically with a very high temperature, normally producing high concentrations of NO_x and little soot.

The air pollution from internal combustion engines was already in 1940 becoming a major issue. In the Los Angeles basin, smog was causing people to have breathing problems and sight was limited by the thick fog. In 1952, Haagen-Smit [48] demonstrated that the smog was a result of nitric oxides and hydrocarbons being exposed to sunlight, connecting it to exhaust gas emissions from cars. In the 1960s, the US introduced an air pollution control scheme, limiting the emissions from certain cars models. From the 1990s, the pollutants from CI engines have dramatically dropped in levels. This is mainly a result of strict policies introduced by the EU, the US and Japan. In Europe, the emission standard EURO 1/I[2] started in 1992, where NO_x, particulate matter (PM), CO and unburned hydrocarbons (UHCs) were restricted. In the following decades, leading up to today, a six-stage scheme with gradually increasing emission control has been implemented. For light duty passenger cars, the maximum allowed NO_x emission level has been decreased by 84% since EURO 3 in 2000, and PM has been decreased

[2] Arabic numerals are for light duty vehicles and roman numerals are for heavy duty vehicles.

by 90% during the same period [35], see Figure 1.2. For heavy duty vehicles, the relative decrease in NO_x and PM was similar. These regulations forced original equipment manufacturers (OEMs) to invest heavily in research and development such that they were able to meet the stringent requirements. Investments in engine design, fuel design and novel aftertreatment equipment evolved rapidly as a result of this.

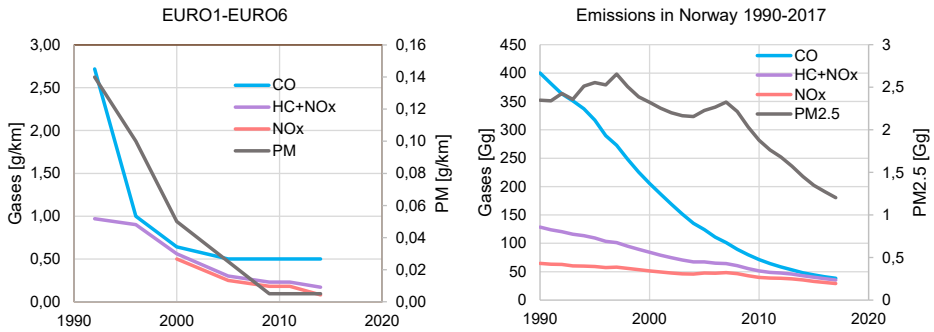

Figure 1.2: Left: European emission standard EURO 1-EURO 6 (1992-2014) for light duty passenger cars [35]. Right: total pollutant emissions in mass from on-road transportation in Norway between 1990 and 2017 [34].

Ultrafine soot particles are known to be a health hazard as they penetrate into the blood stream through the lungs. Acting like Trojan horses, they carry with them volatile or non-volatile toxic chemicals condensed on the particle surface, reaching organs and cell compartments that could not be reached without the solid particles [144]. The ultimate consequence for humans exposed to PM over time is damage of genomic DNA, and thereby the potential of developing mutations and ultimately tumors.

The main contributions to the decrease of pollutants emitted from CI engines have been higher fuel injection pressure, adjustments to fuel injection timing, higher intake pressure, lower intake temperatures, improved combustion chamber geometry and exhaust gas recirculation (EGR) [26]. However, the stringent pollutant targets have made it necessary to aftertreat the combustion products with advanced equipment onboard the vehicle. For NO_x emissions in CI engines, the most commonly used aftertreatment system now is the selective catalytic reduction (SCR) system, which reduces the NO_x to N_2 and H_2O by addition of urea [78]. The SCR is often used in combination with EGR, which lowers the flame temperature by mixing the intake air with exhaust gases [94].

For reduction of PM emissions, a diesel particulate filter (DPF) is added to the

exhaust system. The filter has the capability of reducing the particulate number by 2-3 orders of magnitude under normal operating conditions [18]. However, issues related to clogging of the filter can occur, where PM accumulates on the filter, creating a back pressure which increases the fuel consumption of the engine. One solution to this problem is to continuously remove the soot by the use of high temperature exhaust together with high concentrations of NO_2 (passive regeneration) [47]. This normally requires a catalyst which oxidizes NO to NO_2, which further is used to burn the soot particles. Another way is to burn off the soot with elevated exhaust temperatures by injecting fuel into the exhaust stream or by post-injection in the cylinder (active regeneration) [7]. During the active regeneration, an increase in particulate number is observed, usually with larger diameter particles [18]. A continuous (passive) regeneration is desirable since it does not require a periodic burnout cycle, which consumes fuel and increases emissions. In order to facilitate continuous passive regeneration, a high exhaust temperature, high reactant concentration (carbon and O_2) and a high oxidation rate of the soot particles are desired. However, this becomes hard to achieve during low load or idle conditions, and a combination of the two techniques are often chosen in order to balance PM control and cost.

Ideally, no soot should be formed in the engine that would have to be filtered out, or emitted to the ambient. This is however difficult to achieve in a CI engine, but is constantly a target for researchers and OEMs worldwide. Different strategies for soot reduction in CI engines have been proposed, including ultra high injection pressure combined with micro orifices [119, 152], oxygenated fuel additives [107, 45, 99, 97], injection strategies [98] and change of combustion mode (e.g. partially-premixed compression ignition low temperature combustion [PPCI LTC] [103]).

The initial formation of soot is still not fully understood, as the chemical and physical processes still lack knowledge, resulting in shortcoming of a predictive and reliable model for soot formation [140, 66]. In addition to soot in CI engines, the understanding of soot formation is also important in applications such as production of carbon blacks, which is used in ink, tires, plastics and coatings. Furthermore, emission of black carbon into the atmosphere has shown to accelerate climate warming in form of increasing the absorbing effects of the sunlight in the atmosphere and on snow/ice covered surfaces on earth [15]. The black carbon effect on the climate has been identified as the second most important human emission in terms of climate forcing, where CO_2 is the primary factor. On-road and off-road CI engines are found to be some of the largest contributors to black carbon emissions. In the future, the likely continuation of using CI engines, combined with the added complexity of using alternative fuels such as biofuels, emphasizes

the need to understand more about the in-flame and tail-pipe soot processes.

Summarizing, there are three major reasons for studying soot in CI engines:

- reducing the amount of PM emissions, resulting in improved air quality for both human health and climate change purposes;
- reducing in-cylinder soot, resulting in an increase of the engine thermal efficiency by avoiding regeneration of the DPF;
- increasing the understanding of the physical and chemical processes connected to the formation of soot in spray flames, facilitating the two former arguments, and benefiting other applications connected to soot formation.

1.1 Objectives

The primary goal of this doctoral project has been to obtain knowledge about soot production in biofuel spray flames, and to develop equipment and techniques that enable research on alternative fuels in CI engines. The project has been focused on investigating soot and combustion characteristics in biofuel spray flames using state-of-the-art optical techniques. The objectives set to be achieved are:

- to develop a research test rig for investigating CI engine combustion and to perform optical measurements of in-flame combustion characteristics;
- to further develop a measurement technique for high temporally and spatially resolved in-flame soot concentrations;
- obtaining quantitative data on in-flame soot from surrogate fuels relevant for fatty acid methyl esters (FAME) fuels;
- increasing the knowledge about combustion and soot characteristic of potential future biofuels.

1.2 Organization of the thesis

The thesis is organized in six chapters, where the current chapter presents the motivation and objectives of the work. In Chapter 2, relevant theory and background are presented, covering spray combustion, soot fundamentals and biofuels for CI engines. Chapter 3 presents important aspects of the newly constructed experimental test rig, where operational and physical characteristics are presented. The optical techniques used for measuring combustion and soot characteristics are presented

in Chapter 4, including a brief review of optical techniques used for measuring in-flame soot. A summary of all results is presented in Chapter 5, where **Article I** presents development and application of diffuse back-illuminated extinction imaging of soot, **Article II** compares combustion and soot characteristics of biodiesel surrogate fuels and real biodiesel, **Article III** presents detailed combustion and soot characteristics of HVO, and **Article IV** investigates glycerol as a soot reducing additive in CI engines. Finally, conclusions based on the results are given in Chapter 6, where also an outlook is given.

2. Theory

2.1 Spray combustion

2.1.1 Fuel injection

In a CI engine, the combustion occurs in a multiphase flow where the liquid fuel is injected into the ambient gas. The injector nozzle can have several holes with diameters ranging from 0.2-1 mm. The main target is to get the fuel to mix with the ambient gas as quick as possible, such that autoignition can occur quickly. In order to achieve this, a high injection pressure is needed, normally up to 2500 bar in modern cars[1]. As the fuel is injected, it breaks up and forms a conical spray. The break up of the liquid happens in two steps, the primary break-up and the secondary break-up, see figure 2.1. The primary break-up consists of large ligaments and droplets, forming a dense spray near the nozzle hole. This is mainly driven by internal nozzle mechanisms such as cavitation and turbulence. The secondary break-up breaks the droplets and ligaments into smaller droplets and is mainly driven by aerodynamic forces occurring because of the high velocity between the liquid and gaseous phase [16, 83]. The exit velocity of the fuel is normally between 300-500 m/s, resulting in the droplets becoming much smaller than the hole diameter, which is called the atomization regime. The resulting droplet size in the spray is determined by several factors. Increasing the injection pressure or decreasing the nozzle hole diameter, reduces the atomized droplet size [51]. Fuel properties are also important, where a lower viscosity or a lower surface tension also decreases the droplet diameter. These effects are less significant at higher injection pressures.

The size of the liquid droplets in the spray are in the range of 20 to 100 μm in diameter. As the droplets are exposed to the hot ambient gas, three effects come into play, i.e. deceleration due to aerodynamic drag, heat transfer from the ambi-

[1] For instance the CRS3-25 common-rail system from Bosch GmbH

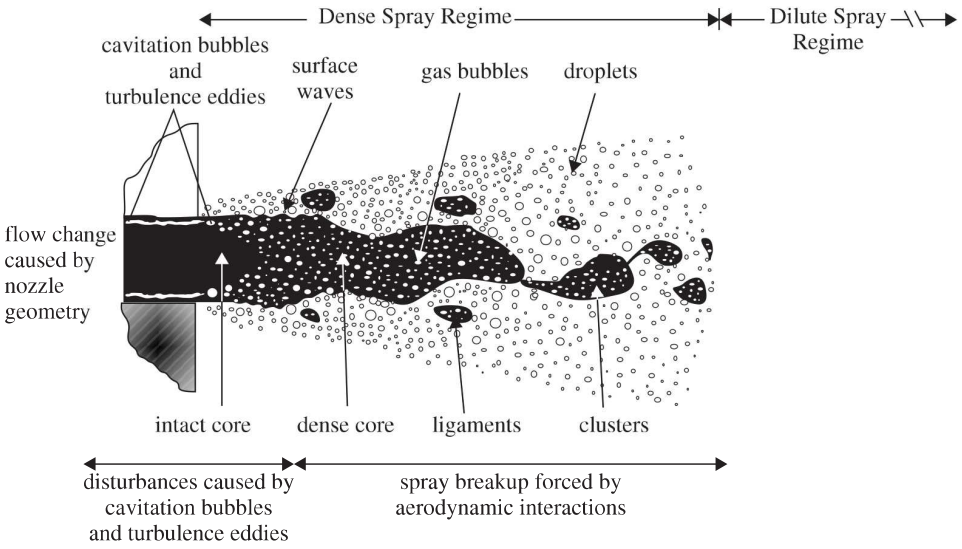

Figure 2.1: Diesel injection close to the nozzle hole [83].

ent to the droplet, and mass transfer of vapor fuel from the droplet to the ambient [51]. The evaporated fuel mixes with the hot ambient gas, eventually forming a combustible mixture. The evaporation of the fuel droplets also has a cooling effect on the air-fuel mixture, which affects the combustion process [68]. The evaporation characteristics are usually assessed by measuring dispersion and penetration length of the vapor and liquid phase, either for a non-reacting case using an inert gas or a reacting case using an oxidant as ambient gas. By injecting into an ambient gas with similar thermodynamic conditions as found in an engine, the vapor phase cone angle of the jet and the temporal development of the penetration length can be measured, giving information about the amount of entrained gas and the evaporation properties of the spray, e.g. [114, 8, 157]. Based on a simplified model for a non-reacting, non-vaporizing jet, Naber and Siebers [104] derived the relations for the vapor penetration length over time. Also from these relations, the cross-sectional mean equivalence ratio at any axial distance from the nozzle hole was derived.

2.1.2 Premixed combustion phase

The evaporated fuel cools the gases down to below the ignition temperature limit [53], however, as the mixing of fuel vapor and ambient gas continues, the temperature of the fuel-air mixture increases. The higher temperature of the fuel-air mixture initiates low temperature reactions, which can be detected by a moderate pressure increase, or low emission of OH* chemiluminescence from the cool flame

[123]. This period is known as the first stage ignition period. Chain-branching reactions consume fuel and produce radicals, which in turn increases the temperature and pressure to the point where second stage ignition is initiated. The start of second stage ignition is usually characterized by a sudden significant increase in heat release rate, which is accompanied by a significant increase in OH* chemiluminescence emission, which is mainly driven by decomposition of hydrogen peroxide and the resulting production of OH radicals which accelerates the process [154, 149]. In experiments, the time between start of injection and start of second stage ignition is called the ignition delay time (IDT). By the time second stage ignition has started, the fuel and air have had time to mix, forming a premixed mixture, which burns volumetrically. Figure 2.2 shows the temporal development of a single spray diesel combustion event, where second stage ignition is detected by broadband chemiluminescence and shadowgraph, marking the start of premixed combustion phase.

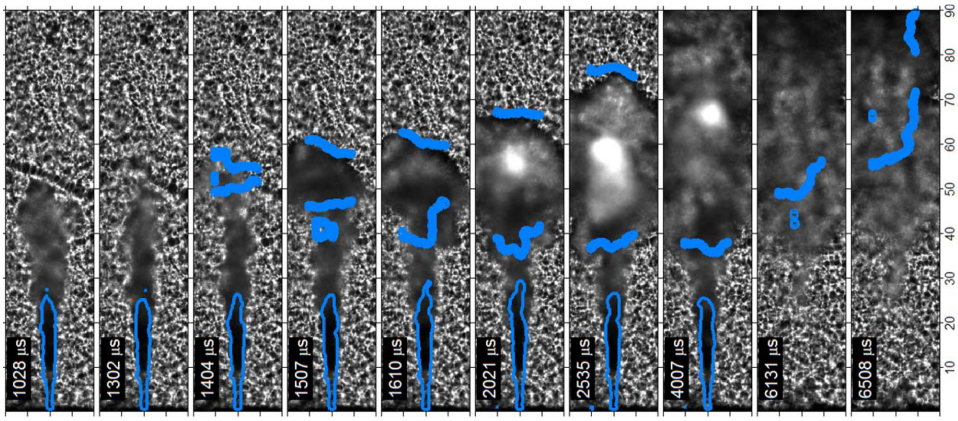

Figure 2.2: A combustion event for a diesel injection, measured by the technique shadowgraph, overlaid on simultaneous chemiluminescence imaging and Mie-scatter imaging (blue contours), showing the high temperature reaction zones and the liquid phase, respectively. The premixed combustion phase is shown for 1404-2021 μs. The length scale is in mm, and the time scale is time after start of injection. The figure is adapted from [123].

The initial premixed mixture is usually fuel-rich, typically having equivalence ratios of 2-3 [59]. This results in the formation of soot precursors such as acetylene and benzene from fractions of the fuel molecules, and eventually the formation of soot particles. Generally, soot starts to form for equivalence ratios of 2-3 and above [41].

During the premixed combustion phase, both fuel and oxygen in the central part of the flame are consumed, eventually resulting in low concentrations of oxygen. This results in the leading edge of the premixed flame having less oxidation of soot

precursors and soot particles, leading to a high concentration of soot. At the same time, a diffusion flame is formed surrounding the jet, i.e. between the products of the premixed flame and the ambient gas. The central part of the flame consists of small soot particles, while the soot particles are larger at the jet periphery and at the head vortex. However, the soot volume fraction is generally not lower in the central part of the jet [25].

2.1.3 Mixing-controlled combustion phase

The transition from the premixed phase to the mixing-controlled phase happens relatively smoothly. If the injection rate profile and the ambient conditions are stable, the spray flame will stabilize during this phase. The overall heat release rate is generally lower than that during the premixed phase, since it mostly burns at the periphery of the jet, which is limited by turbulent mixing of fuel vapor and ambient gas.

In the stabilized spray flame, the injected fuel evaporates and mixes with the surrounding ambient gas. After a time delay, the air-fuel mixture ignites at a distance from the injector hole, also known as the flame lift-off length (FLOL). Just downstream of the FLOL, a partially premixed region is formed, where the central part of the jet is fuel-rich, while the periphery is fuel-lean, resulting in less intense reactions in the center compared to those found in the peripheral regions, see [25, 80, 121] for conceptual models of the spray flame during the mixing-controlled phase. In the peripheral regions of the jet, a near stoichiometric mixture is present resulting in a high heat release zone. Since this region is defined as having a fuel-rich side and a fuel-lean side, it can be characterized as a diffusion flame. As the partially premixed region close to FLOL reacts, the products that are formed based on the air-fuel mixture at FLOL determine the downstream soot precursor formation rate. A richer mixture at FLOL leads to higher pyrolysis reaction rates, producing higher concentrations of soot precursors. Higher temperatures have also shown to increase soot production in CI sprays, even for conditions where mixing prior to FLOL was kept equal [79]. This suggests that the soot produced downstream of FLOL is being formed in a diffusion-like flame, since an increased soot production rate indicates that the pyrolysis rate increases more than the oxidation rate for elevated temperatures, which is usually observed in diffusion flames [41]. After the formation of soot precursors, nucleation of soot particles takes place after a small delay. This delay is dependent on the initial fuel structure, mixture temperature, and equivalence ratio. For fuels with unsaturated hydrocarbons, or aromatic content, soot nuclei are produced earlier.

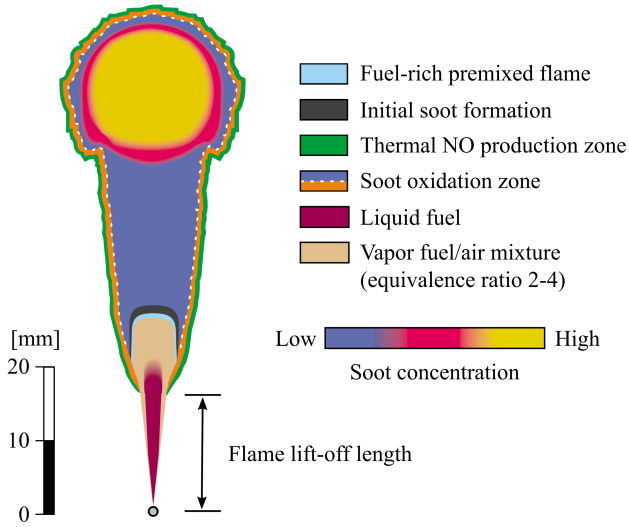

Figure 2.3: Conceptual model of a CI spray during the mixing-controlled period. Adapted from [25].

Flame lift-off length

An important feature of the mixing-controlled phase is the point where the flame stabilizes, defining the FLOL. The mechanisms behind the stabilization of the FLOL can be explained in two different ways. Based on gas-jet theory, Peters explains the stabilization of FLOL in a partially premixed flame by premixed flame propagation, where the balance between the jet velocity and the turbulent flame speed defines the axial distance from the injector tip to FLOL (H) [118]:

$$H \sim \frac{U Z_{st} D}{[s_L(Z_{st})]^2}, \tag{2.1}$$

where U is jet exit velocity, Z_{st} is stoichiometric fuel mixture fraction, D is thermal diffusivity, and $s_L(Z_{st})$ is laminar flame speed for a stoichiometric mixture. This shows that a higher jet exit velocity increases the FLOL, while higher laminar flame speeds decreases FLOL. However, this theory is based on gas jets injected into an ambient with similar density to the injected gas, and combusting under atmospheric pressure and temperature, resulting in the jet being isothermal up to the FLOL. This differs from the CI spray combustion case where the spray is non-isothermal, vaporizing upstream of FLOL, and influenced by the ambient gas density on mixing of the spray [134].

While the first approach is based on the laminar flame speed and the thermal diffusivity, the second approach is based on ignition delay time. Pickett et al. [122] measured the FLOL of large-hydrocarbon fuels having different cetane numbers, observing that the FLOL decreased with increasing cetane numbers, despite having similar premixed flame speeds. Further analysis showed that the timescale for jet mixing from the injector hole to the FLOL collapsed to an Arrhenius-type expression,

$$\tau_H = 9.19 \cdot 10^6 \cdot exp(6534/T_a) \cdot \rho_a^{-0.96} \cdot Z_{st}^{-1.89} \tag{2.2}$$

where τ_H is the calculated jet mixing time scale, representing the residence time from start of injection to start of ignition at FLOL. T_a is ambient gas temperature in K and ρ_a is ambient gas density in kg/m^3. The ignition delay times were also found to follow an Arrhenius-type expression, which concludes that the FLOL is governed by an ignition chemistry based mechanism. In practice, this means that an observed increase in ignition delay time leads to a longer FLOL. This relation also explains trends observed in high pressure spray combustion, like increasing FLOL with increasing orifice diameter and ambient gas oxygen concentrations [135].

A summary of the effects on FLOL in a CI spray under quiescent conditions is given below [134, 135]:

- Ambient gas temperature and density have strong non-linear relationships to the FLOL, where a higher temperature or density results in a shorter FLOL. Using Peters theory, the change in FLOL due to temperature and density can be explained by corresponding change in laminar flame speed and thermal diffusivity. In addition, the density has an effect on spray development, also affecting the FLOL.
- A smaller orifice diameter results in a shorter FLOL.
- A higher injection pressure result in a longer FLOL.
- The FLOL is inversely proportional to the ambient gas oxygen concentration, i.e. an increased oxygen concentration decreases the FLOL.

Air entrainment

The FLOL is as mentioned a very important parameter affecting the amount of air mixed in prior to ignition, i.e. determining the equivalence ratio at FLOL. The

equivalence ratio at FLOL affects the soot production in the spray flame during the mixing-controlled period, e.g. where a low equivalence ratio can result in sootless combustion (leaner lifted flame combustion [120]). The FLOL is again affected by several parameters such as ambient thermodynamic conditions, nozzle geometry, injection pressure and fuel specifics. Naber and Siebers [104] developed a spray penetration model for a non-reacting and non-vaporizing spray, which also provides the cross-sectional averaged equivalence ratio ($\overline{\phi}(x)$) at any axial distance from the injector tip. This can be applied to the CI spray upstream of FLOL in order to estimate the equivalence ratio at FLOL. The model is given as

$$\overline{\phi}(x) = \frac{2 \cdot (A/F)_{st}}{\sqrt{1 + 16\,(x/x^{+})^{2} - 1}}, \tag{2.3}$$

where $(A/F)_{st}$ is the stoichiometric air-fuel mass ratio, x^{+} is the characteristic length scale of the spray, i.e.

$$x^{+} = \sqrt{\frac{\rho_f}{\rho_a}} \frac{\sqrt{C_a} \cdot d}{0.75 \cdot tan(\theta/2)}. \tag{2.4}$$

x is axial distance from the injector orifice, ρ_f is fuel density, ρ_a is ambient gas density, C_a is nozzle area contraction coefficient, d is orifice diameter, and θ is spreading angle of the spray. As seen, the equivalence ratio at FLOL ($x = H$) is affected by the value of H, i.e. a longer FLOL leads to a lower equivalence ratio and vice versa.

For changes in oxygen concentrations in the ambient gas (e.g. when applying EGR) the amount of oxygen entrained into the spray upstream of FLOL is affected. For a lower oxygen concentration in the ambient gas, a lengthening of the FLOL occurs, which can be seen from Equation 2.2, since Z_{st} decreases. This results in more ambient gas being mixed in upstream of FLOL. However, the lower concentration of oxygen in the ambient gas results in less oxygen being mixed in, counterbalancing the FLOL lengthening effect [135]. The resulting effect on the equivalence ratio at FLOL is therefore small, and for some conditions even negligible [120].

For the case of decreasing the ambient gas density, the FLOL is lengthened, which allows for more air to be mixed in upstream of FLOL. At the same time, the air entrainment rate decreases with decreasing ambient gas density, due to decreased mixing. These effects counterbalance each other, making the equivalence ratio at FLOL nearly insensitive to changes in ambient gas density [134].

For decreasing orifice diameters, the FLOL has been shown to shorten, resulting in less time for air entrainment upstream of FLOL. However, with decreasing diameters, the air entrainment rate increases linearly with decreasing diameters, consequently increasing the equivalence ratio at FLOL for decreasing diameters [134].

The air entrainment is therefore mostly affected by changes in ambient gas temperature, injection pressure and injector orifice diameter. Changes in the ambient gas oxygen concentration and density have minor effects.

2.2 Soot fundamentals

Soot is defined as solid carbon particles, usually consisting of aggregates or agglomerates[2] of smaller primary soot particles. These particles are formed in flames combusting under fuel-rich conditions, where oxygen is limited for oxidation. The initial building block of soot is known to be polycyclic aromatic hydrocarbons (PAHs), which are formed under these conditions.

The formation and oxidation of soot are complex, involving both chemical and physical mechanisms. Detailed reviews on these topics are given by Calcote [17], Glassmann [41], and Richter and Howard [129], while Tree and Svensson [148] provide a brief review of soot processes in CI engines. A summary of the soot processes is given here.

2.2.1 Pyrolysis

The initial step of soot formation occurs in gas phase under fuel-rich conditions. Gas phase fuel molecules undergo pyrolysis due to high temperatures and the lack of oxygen in the mixture, resulting in decomposition and atomic rearrangement of the fuel molecule into soot precursors. The pyrolysis process is generally endothermic, making the rates highly temperature dependent. The rates are also heavily dependent on the fuel concentration, i.e. the equivalence ratio. These pyrolytic products are usually unsaturated hydrocarbons, in particular acetylene (C_2H_2) and PAHs such as benzene (C_6H_6). The soot precursor production rate is balanced by oxidation reactions, where the precursors are mainly attacked by OH radicals. The oxidation rate is also highly temperature dependent, actually increasing more compared to the pyrolysis rate for elevated temperatures. This results in premixed flames sooting less than diffusion flames for elevated temperatures, because the soot precursor formation region in a premixed flame has access to oxygen, while in a diffusion flame, soot precursor formation occurs in regions not containing

[2] Agglomerates are assemblages of particles, and aggregates are pre-nucleation structures in any state that in turn may develop into agglomerates [109].

oxygen [41].

2.2.2 Nucleation

As the soot precursors are further subjected to high temperatures and long enough residence times, small nuclei are formed, having diameters of $\sim$1.5 nm [129]. According to Glassman et al. [42], there is a general mechanism for soot production that is only dependent on the choice of kinetic pathways to intermediates. The choice of pathways are mainly affected by temperature and fuel molecule structure, resulting in the fuel's propensity to form soot particles being determined primarily by the initial formation rates of the first and second ring structures. The subsequent mechanisms controlling nucleation and further particle growth remain unchanged and are fast compared to the former mechanisms, making the initial formation rate of aromatic ring species important for the total soot production. This is also important since the incipient soot formation concentration determines the final soot volume fraction. Predicting soot production rates in simulations can therefore be limited to the calculation of important soot precursor concentrations [155, 113].

In particular, hydrogen radicals, vinyl (C_2H_3) and acetylene are important species connected to the initial soot formation. The H atom and acetylene regulates the PAH growth rate by hydrogen abstraction and acetylene addition, also known as the HACA[3] sequence [37]. Acetylene is the most stable hydrocarbon in the post-reaction zone of the flame, and hence the most abundant species, making it an important species in the soot formation process. The HACA mechanism is also observed to be dominant for high temperature pyrolysis of aromatic fuels like benzene, where direct combination of benzene molecules initially occurs, but eventually follows the HACA sequence and forms acetylene. This sequence is observed for all hydrocarbon fuels, emphasizing the importance of acetylene in soot formation. The further combination of PAHs results in large three dimensional structures, eventually resulting in solid phase carbon nuclei.

2.2.3 Surface growth

After the formation of soot nuclei, the solid phase carbon reacts further with gas phase acetylene and PAH. The addition of these species results in mass growth, but not in particle number increase. As the particle grow in size, they also collide with each other, also known as coalescence, where two particles result in a single spherical particle with a larger diameter. The particles can also agglomerate, meaning that individual particles can collide and stick to each other, forming clusters of primary particles.

[3] hydrogen abstraction C_2H_2 addition.

2.3 Biofuels for compression ignition engines

Alternative energy resources for CI engines have been sought for since the first CI engine was developed. The development of biofuels was initially driven by petroleum oil shortage, such as during the Second World War (1939-1945) and during the energy crises in the 1970s [73]. In recent times, the motivation has mainly been to reduce greenhouse gas emissions. The first bioderived fuel used in a CI engine was neat vegetable oil. However, operational problems due to the high viscosity caused major problems to the combustion, such as poor spray atomization and engine deposits. As a consequence, chemical processes for upgrading the vegetable oil were needed. Alternative techniques such as the Fischer-Tropsch (FT) process has also been used to convert gas produced from biomass into liquid fuel, resulting in a diesel-like fuel, often referred to as biomass-to-liquid (BTL) fuel. The commercially available end products existing today, after upgrading the biomass via several processing routes, can be classified as:

- methyl esters, made from vegetable oil converted to biodiesel via transesterification;
- paraffins (mixture of straight and branched alkanes), produced from vegetable oil via hydrotreating, i.e. HVO, or biomass converted to gas and processed to liquid fuel via the FT process.

A distinction must be made between conventional and advanced biofuels, also known as first and second generation biofuels, respectively. Advanced biofuels require the feedstock to originate from non-food crops or industrial waste and residue, and to be capable of significantly reducing greenhouse gas emissions compared to their fossil alternatives. The feedstock can also not directly compete with food and feed crops for agricultural purposes [62].

2.3.1 Biodiesel

Vegetable oils from several plant sources have been used in the production of biodiesel. The feedstock is normally determined based on geography, climate and economics, where for instance rapeseed oil is produced in Europe, soybean oil in the US and palm oil in countries with tropical climate. The variation of feedstock used for biodiesel results in a large variation in fuel properties [74, 75].

The production process

The production of biodiesel is based on the chemical process of transesterification, where an ester is produced from another ester through interchange of organic

groups with an alcohol [112], see Figure 2.4. Vegetable oil consists of triacylglycerols, i.e. an ester consisting of three long-chain fatty acids connected via glycerol, which is split into three alkyl ester molecules by adding an alcohol. The most commonly used alcohol for biodiesel production is methanol, resulting in triacylglycerol and methanol producing methyl esters and glycerol. The process can be performed by simply mixing the reactants, however, the process is usually catalyzed by acids or bases, where bases have shown to be the most effective catalyst. The end product is a mixture of methyl esters and glycerol, which are in two separate phases, making it easy to separate them by gravity or centrifugation, resulting in glycerol as a byproduct.

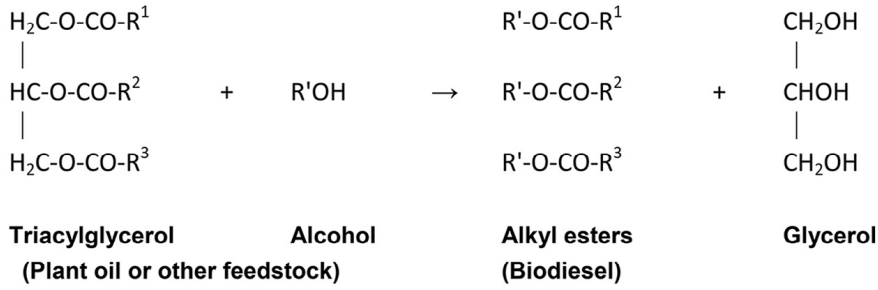

Figure 2.4: Production of biodiesel via transesterification. A vegetable oil (triacylglycerol) and an alcohol reacts and produce alkyl esters [76].

Fuel properties

The varieties of methyl esters include differences in chain length, degree of unsaturation, and location of double bonds, resulting in different fuel properties of the resulting biodiesel. The carbon chain length of a typical methyl ester molecule in biodiesel is in the range of 16-18, and is highly dependent on the feedstock. The cetane number of individual methyl esters decreases with increasing unsaturation and increases with carbon-carbon chain length. Typical components found in biodiesel such as methyl palmitate (C16:0)[4], methyl stearate (C18:0), methyl oleate (C18:1) and methyl linoleate (C18:2), have cetane numbers of approximately 75, 87, 60 and 40, respectively, showing the strong correlation between cetane number and unsaturation [165]. Comparing methyl palmitate (C16:0) and methyl stearate (C18:0) also shows that the cetane number increases from 75 to 87 by adding two carbon atoms to the alkyl chain. The same trends are found for heat of combustion, melting point and viscosity. Generally, the properties of biodiesel

[4]The alkyl chain length is given as the first number, while the number of double bonds in the alkyl chain is given as the second number.

are fairly similar to that of diesel fuel, where the main differences are found in the lower heating value (∼14% by mass lower than diesel), viscosity (higher), oxidative stability (lower), cold flow performance (lower) and lubricity (higher) [74].

Combustion and emission characteristics

The combustion emission characteristics of biodiesel compared to diesel fuel in CI engines have been reviewed by Lapuerta et al. [85]. An increase in brake specific fuel consumption (BSFC) is found for biodiesel compared to diesel fuel, which generally is proportional to the lower heating value of biodiesel. This means that the thermal efficiency is generally not affected by powering with biodiesel compared to diesel fuel, since the product of lower heating value and BSFC remains unchanged. The fuel-bound oxygen content in biodiesel, approximately 10% by weight, has large effects on the emissions from biodiesel in CI engines. Regulated emissions like CO and UHC are usually found to be considerably lower compared to diesel fuel due to the presence of oxygen.

PM emissions are also found to decrease with increasing content of biodiesel in diesel fuel. This is also attributed to the oxygen content in biodiesel. However, studies measuring the PM size distribution when fueling with biodiesel show that the particulate number in the nucleation mode of biodiesel PM is higher than that of diesel fuel [153]. Ultrafine particles penetrate easier in the respiratory and circulatory system [144], acting as Trojan horses for condensed toxic compounds, causing adverse health effects on peripheral regions of the body.

A slight increase in NO_x emissions is found for the case of biodiesel compared to diesel fuel, although not consistent for all studies. The increase in NO_x is often explained by the advanced start of ignition for biodiesel, resulting in a faster overall combustion event, leading to higher temperatures [54]. However, the increase in NO_x concentration is likely a result of many factors, such as injection timing, ignition delay, adiabatic flame temperature or radiative heat loss, resulting in various results and explanations, and consequently making it hard to reach a consensus on this matter.

2.3.2 Hydrotreated vegetable oil

HVO has become a promising alternative fuel over the past decade. The Finnish oil refining company Neste Oyj[5] was the first company to produce HVO in a large scale, and is currently the largest producer of HVO in the world. The first production facility started in 2007, now having a capacity of 2.6 million tons annually (3.3 million m^3 per year) [111]. HVO has grown in popularity because of its good

[5]Neste means "liquid" in Finnish.

combustion and emission performance in CI engines. In addition, the fuel can be directly used in a CI engine up to 50% blending ratio with diesel fuel without any modifications [33, 86].

The production process

The feedstock of HVO can be the same as that of biodiesel, which means that both fuels can or cannot be termed as advanced biofuels, depending on their feedstock. Starting with vegetable oil, the triacylglycerol is hydrotreated with hydrogen resulting in di-glycerides, mono-glycerides and acids [58]. The following step converts the intermediates into normal-alkanes through decarboxylation, decarbonylation and hydrogenation. Some of the normal-alkanes also undergo isomerization and cracking, leading to isomerized and lighter alkanes in the product. The result is a mix of normal and isomerized alkanes with carbon chain length of 15-18. The fuels are therefore free from aromatics and oxygen, having a relatively high cetane number. Since the molecular structure of HVO is similar to that of gas-to-liquid (GTL) and BTL, the following summary of fuel properties, combustion and emission characteristics also partially applies to GTL and BTL.

Fuel properties

The resulting fuel properties of HVO are similar to that of diesel fuel, where the largest difference is found for density and cetane number. In fact, the density and the cetane number are the only properties limiting HVO from complying to the European Standard for diesel fuel (EN 590). Instead, HVO fits in to the standard EN 15940 for paraffinic fuels, together with synthetic fuels such as GTL and BTL. Operationally, in CI engines tuned for diesel fuel, the main limiting factors are low lubricity, high cetane number and poor cold flow properties of HVO, which can be solved by tuning the engine, or using additives in HVO to deal with the low lubricity and cold flow properties [86]. The lower heating value of HVO is slightly higher than that of diesel fuel ($\sim$3%), while the density is lower ($\sim$8%), resulting in $\sim$5% lower energy content per volume for HVO, leading to 5% higher BSFC [1]. Another important difference of HVO is the boiling point (at 90% distilled fraction), which is lower than for diesel fuel, resulting in faster evaporation during injection of the fuel.

Combustion and emission characteristics of HVO are reviewed in **Article III**.

2.3.3 Other biofuel processing routes

Fischer-Tropsch process

For producing liquid diesel fuel from biomass, a possible route is the FT process. The FT process uses synthetic gas (syngas), which is a mixture of carbon monoxide

and hydrogen ($CO+H_2$), with help from catalysts to produce a wide range of paraffins. The bioderived syngas is produced from gasification using steam, oxygen and treated biomass. The biomass can be any carbonaceous material, for instance lignocellulosic material from forestry or agricultural residue. The thermochemical gasification process is complicated and can be split into the partially overlapping steps: drying, where the bound water is released from the biomass as steam; thermal decomposition, i.e. pyrolysis and devolatilization, where CO_2, H_2O, H_2, CH_4 and CO are released; reactions leading to the conversion of biomass to char; and gasification of solid chars, where syngas is produced from solid char reacting with surrounding gases [91].

The syngas resulting from the gasification process is cleaned and conditioned before used in the FT reactor. The conditions in the reactor can have pressures of 10-40 bar, and can either operate in low temperature (200–240°C) or high temperature (300–350°C) range, depending on the desired product yield distribution [142]. For the production of a diesel-like product, cobalt (Co) catalysts are used in a slurry reactor at low temperatures, yielding linear waxes ($>C_{20}$), which are further hydrocracked to shorter paraffins, constituting the FT diesel fuel. A schematic flow sheet of the FT process is shown in Figure 2.5. The low temperature FT process has the advantage of having a high yield of FT diesel fuel and containing no aromatics, which is beneficial for use in CI engines. However, similar to the HVO, the density of the resulting fuel is too low for being an on-specification fuel according to the diesel standard EN 590 [88].

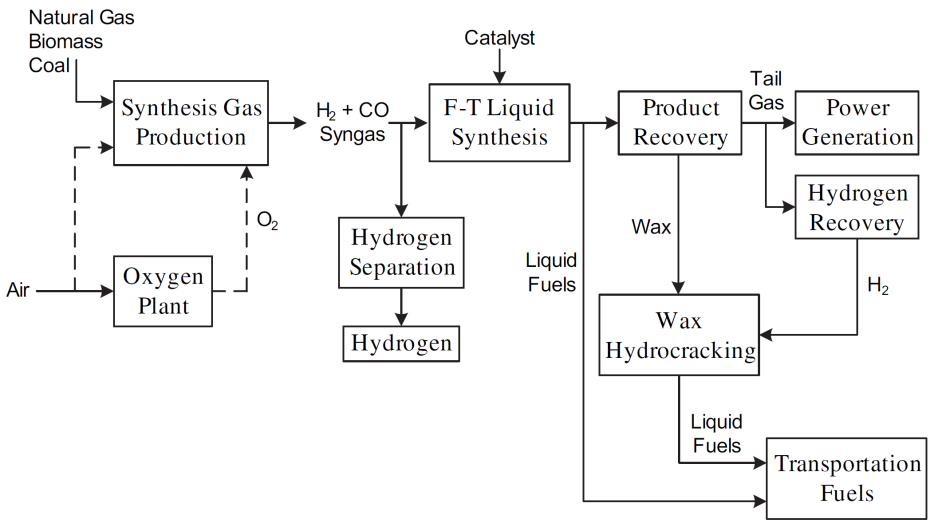

Figure 2.5: Fischer-Tropsch process flow sheet [40].

A major disadvantage of the FT synthesis is the unavoidable production of a wide range of hydrocarbon products, which requires upgrading and forcing the producer to make use of all streams in order to be economically viable, making the production facility complex. An additional problem is the large amounts of heat produced, since the conversion process is exothermic. The range of products are influenced by feed gas composition (H_2/CO), temperature, pressure, and the type of catalyst used. Consequently, the development and optimization has been heavily focused on heat removal and temperature control, and finding the most efficient catalysts [142].

As mentioned, the resulting FT fuel from low temperature FT is characterized by having no aromatics, a relatively low density ($\sim$770-780 kg/m^3 [88]) and a high cetane number ($\sim$70-85 [40]). FT diesel fuel has shown to have good properties and can be blended with diesel fuel in order to improve emissions and combustion characteristics. In general, FT fuels show a reduction in NO_x and PM emissions compared to diesel fuel [4]. In addition, if the FT fuel is biomass derived, the well-to-wheel CO_2 emission is reduced compared to fossil based fuel [40].

Fast pyrolysis

Production of bio-crude, i.e. bio-based oil, can be achieved from fast pyrolysis. Pyrolysis is a thermochemical process carried out at atmospheric pressure at temperatures ranging from 300 to 700 °C, where biomass is rapidly heated in the complete absence of oxygen. The products from the process consists of liquid bio-crude, biochar and gases. The resulting composition of the yield is determined by several parameters such as pyrolysis temperature and heating rate. The produced bio-crude contains a mixture of complex hydrocarbons with large amounts of oxygen and water, resulting in a low lower heating value, typically around 20 MJ/kg (dry basis) [10]. Fast pyrolysis is characterized by high heating rates (10-200 °C/s) and short residence times ($<$2 s). By further increasing the heating rate (10^3-10^4 °C/s) and reducing the residence time ($<$0.5 s), flash pyrolysis is achieved, which results in a higher liquid yield [10]. The feedstock used for production of bio-crude from fast pyrolysis can involve lignocellulosic biomass [69] or algae [21].

In order for the bio-crude to be used as transportation fuel, upgrading is needed. The pyrolysis oil could be blended with diesel fuel or biodiesel as an emulsion. However, Lee et al. [89] concluded that using wood pyrolysis oil as an emulsion causes operational problems such as clogging of injectors and deposits in the fuel system. There are not many studies investigating upgraded fast/flash pyrolysis fuels in internal combustion engines. Van de Beld et al. [150] studied fast pyrolysis oil from pine wood and tested both neat pyrolysis oil and partially upgraded pyrolysis oil via hydrotreating and hydrocracking in a CI engine. The neat pyrolysis

oil required elevated inlet air temperature or increased CR to achieve satisfactory combustion because of its poor ignitability. The study concluded that combustion of neat pyrolysis oil in CI engines has many disadvantages connected to acidity, low heating value, low cetane number, high water content, and high sensitivity to re-polymerization, which leads to clogging of the fuel system. The upgraded fuel was easier to ignite and produced lower CO and higher NO_x emissions, as a result of more complete combustion. However, the upgraded fuel remained acidic, requiring modification to the fuel system.

Hydrothermal liquefaction

Conversion of biomass to liquid biofuel can also be achieved via hydrothermal liquefaction (HTL). The process produces bio-crude which has a higher energy content, higher viscosity and contains less oxygen than pyrolysis oil. The product is not suitable as transportation fuel directly, and therefore needs upgrading to diesel-like fuels, e.g. via hydrotreating or catalytic cracking [44], similar to pyrolysis bio-crude. HTL is a thermal depolymerization process where large hydrocarbon molecules are cracked and oxygen is removed. The reactions are carried out under high temperature and pressure, such that the water present in the biomass is either in a subcritical or supercritical state, and consequently acts as a solvent, reactant and catalyst. The biggest advantage of HTL compared to fast pyrolysis, is that the process is unaffected by the moisture content in biomass, whereas in a pyrolysis process, the presence of water requires heat in order to vaporize, consequently affecting the process economy [3]. The HTL process mimics the process of fossil oil and natural gas formation, which happens over millions of years, while HTL has very short residence times of 15-30 minutes [131]. The short time affects the bio-crude quality, which is rather poor compared to fossil crude oil. The HTL process can be characterized by moderate temperatures (200-400°C) and high pressures (50-200 bar), where the high pressure can be considered as a drawback since it requires large initial investments for high pressure equipment. The feedstock used in HTL is flexible and can consist of woody biomass, industrial wastes, food wastes or algae. However, the chemical composition of the feedstock has a large impact on the product yield [29].

Combustion of HTL fuels in CI engines has not been studied by many. Nabi et al. [105] investigated the combustion and emission characteristics of a crude lignocellulosic HTL fuel blended with diesel fuel up to 30% by volume. The results showed no significant change in engine performance, while total hydrocarbon (THC) and NO emissions were found to be higher and PM emissions were lower. Hossain et al. [55] created a microalgae HTL bio-crude surrogate fuel and tested it with blends of diesel in a CI engine. The surrogate fuel consisted of 20% xylene, 15 % cyclopentanone, 45 % undecane, 10 % butanol and 10 % dioctyl-

phthalate by mass. Comparing the surrogate blends with diesel, the results showed no significant reduction in engine performance, a decrease in PM and CO emissions, and an increase in NO_x emissions. Chen et al. [19] investigated combustion characteristics of a upgraded HTL fuel made from food processing waste blended with diesel fuel in a CI engine. The bio-crude was upgraded via distillation and esterification, resulting in a mixture of alkanes, esters and cycloalkanes, where the composition was dependent on the process operating condition. Engine tests with blends of 10% and 20% by volume upgraded HTL fuel with diesel showed promising results with regards to performance and emissions.

2.4 Fuel effects on spray combustion

As biofuels are emerging into the future market, the fuel composition becomes important for the combustion and emission characteristics in CI engines. The composition has an impact on the macroscopic spray characteristics, i.e. spray penetration, air entrainment rate, spreading angle and spray atomization, which in turn, affects combustion characteristics like heat release, ignition delay time, FLOL and flame temperature. Macroscopic characteristics are interlinked with combustion characteristics, consequently affecting in-flame pollutant formation such as soot, NO_x, carbon monoxide and THC (Figure 2.6). The molecular composition of biofuels depends on the feedstock, production process and upgrading process, where the main groups of molecules are alkanes, cycloalkanes, aromatics, and esters. In commercial diesel fuel, a mixture of all these exist, making diesel fuel combustion extremely complex. The following sections will highlight the molecular composition's effect on the characteristics listed above.

2.4.1 Cetane number

The cetane[6] number is a measure of ignitability, where higher values indicate a shorter ignition delay time for the fuel in a CI engine. In order to determine the cetane rating, ignition delay times of fuels are measured in an IQT[7] or a CFR[8] engine, and compared to ignition delay times of blends of *n*-hexadecane and heptamethylnonane (cetane number of 100 and 15, respectively) [165]. In the IQT, the derived cetane number is measured, while in the CFR engine, the cetane number is measured. The physical time delay between start of injection and ignition is important since it determines the time for fuel and air to mix, thereby also the portion of fuel that burns during the premixed combustion phase. During the mixing-controlled phase, the cetane number has shown to correlate with the FLOL [122], where a higher cetane number decreases the FLOL. The cetane number is

[6] Cetane is *n*-hexadecane, which has cetane number rating of 100.
[7] Ignition Quality Tester by Advanced Engine Technology Ltd. (ASTM D 6890).
[8] Cooperative Fuel Research engine by CFR Engines Inc. (ASTM D 613).

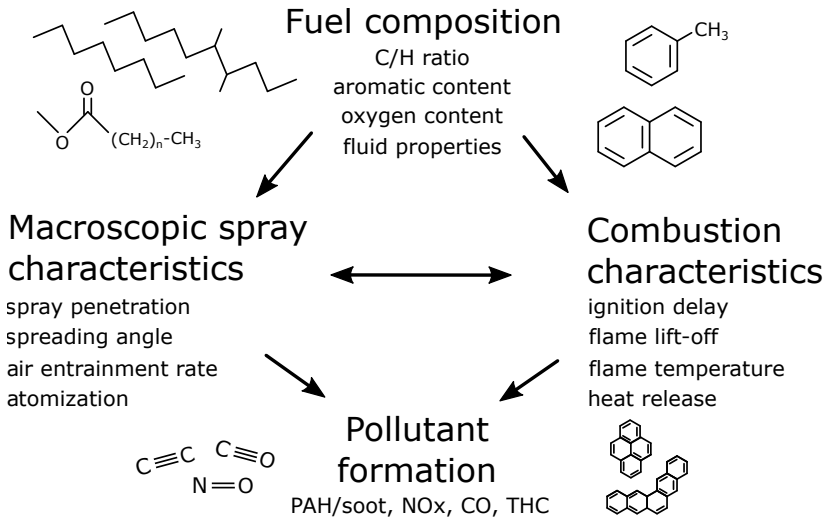

Figure 2.6: Fuel composition effects on spray combustion and pollutant formation.

closely related to the number of carbon-carbon bonds in a paraffinic fuel, where larger numbers lead to higher reactivity. The relatively high content of aromatics in diesel fuel reduces reactivity. For instance, the aromatic compounds toluene, 1-methylnaphthalene and tetralin has cetane numbers of −5-18, −7-0, and 13, respectively [165]. For alkanes, *n*-heptane and *n*-dodecane have cetane numbers of 52-56 and 80-87.6. Unsaturation or branching in the fuel molecules generally leads to a lower cetane number. The cetane number of a fuel blend can be estimated based on the volumetric composition by linear combination of the individual cetane components, although the potential errors associated to the resulting blend's cetane number are amplified [165].

The cetane number has been found to correlate closely with NO_x emissions from CI engines [84]. A lower cetane number increases the ignition delay, hence increases the heat release rate during the premixed combustion phase, which consequently increases thermal NO_x formation. For PM emissions, the opposite is observed, where increasing the cetane number increases PM [108]. This can be explained by the reduction of the almost smoke-free premixed phase duration and thereby increasing the duration of the soot producing mixing-controlled period.

2.4.2 Oxygen content

Fuel-bound oxygen affects combustion chemically since added oxygen facilitates complete combustion, and thereby results in less soot, CO and THC emissions.

Several studies have been focused on the fuel-bound oxygen effect on engine performance and emissions, since an improvement of emission characteristics can be achieved. However, adding oxygen to the fuel also results in a reduced volumetric heating value, hence a higher BSFC [30, 9]. Blending diesel fuel with highly oxygenated additives has shown to reduce PM emissions effectively [57]. Härtl et al. [57] studied 14 different oxygenated additives in diesel fuel in a CI engine, observing strong evidence for reduction of soot emission for increased oxygen content.

The reduction of soot in the exhaust due to increased amount of fuel-bound oxygen is related to the in-flame processes in the combustion chamber. According to Dec's conceptual model for spray combustion, soot production during the quasi-steady period is mainly driven by combustion processes similar to those in premixed flames. This was verified by Kitamura et al. [72] and Westbrook et al. [155], where a kinetic study using homogeneous constant pressure reactors corresponding to the partially premixed region at FLOL was performed for heptane/oxygenate fuel blends. An increase of oxygen content in the fuel showed a reduction of soot precursors in the reactor model, which would correspond to a reduction of in-flame soot. From literature, both diffusion flames and premixed flames have shown to suppress soot inception when increasing fuel oxygen content [32, 61]. In general, the addition of oxygenates to the fuel in a premixed system, or an increase of oxidizer, increases the amount of available oxygen, hence shifting the equivalence ratio closer to stoichiometric.

However, not all of the oxygen present in the mixture is equally effective in reducing soot production, here also the structure of the oxygenated molecule plays a role. Mueller et al. [100] found that tripropylene glycol methyl ether (TPGME), having a -C-O-C- moiety, was more effective in reducing soot compared to dibutyl maleate (DBM), having ester moiety -O-(C=O)-, regardless of the fuel oxygen ratio[9]. The reason for the lower production of soot precursors with the TPGME blend compared to the DBM blend, was that DBM produced CO_2 directly, thereby "wasting" oxygen atoms, whereas TPGME did not produce CO_2 directly, and could therefore use all its oxygen to inhibit soot precursor production. The bonds in CO_2 are strong and do not break under high temperatures in the flame, thereby making the oxygen atom unavailable. This illustrates that the fuel's structure plays an important role to the effectiveness of soot reduction.

The presence of oxygen in the fuel can also affect the FLOL, as observed by Manin et al. [97]. An increased amount of oxygen in the fuel led to longer FLOL for the same ignition delay times, which was hypothesized by the authors to be due to the

[9]Fuel oxygen ratio is defined as the ratio between the moles of oxygen present in the fuel molecule and the moles of oxygen needed for stoichiometric combustion of one mole fuel.

difference in location of the stoichiometric contour lines of the spray. According to Peters [118], the FLOL is stabilized by the laminar burning velocity and the spray velocity, where a higher spray velocity moves the FLOL downstream. At the stoichiometric contours in the flame, high concentrations of OH^* are produced, hence marking where the FLOL is located. For oxygenated fuels, the stoichiometric contours are located closer to the spray central axis, where also higher spray velocities are expected. Assuming that the laminar burning velocities are similar between the fuels[10], the FLOL stabilizes further downstream due to higher spray velocities. This hypothesis is also supported by the ignition based theory for FLOL stabilization [122], where having the same ignition delay between the oxygenated and non-oxygenated fuel, but different FLOLs, can be explained by different velocities of the fluid parcel traveling from the injector to the point of ignition. Since the stoichiometric contour is located in a region with higher fluid velocities for the oxygenated fuel, a greater distance is traveled, hence longer FLOL.

2.4.3 Unsaturation

The degree of unsaturation of the fuel molecules affects the combustion and pollutant emissions in CI engines. Most of the studies performed in CI engines that investigate the effect of fuel unsaturation have been conducted with various types of biodiesel, since their degrees of unsaturation vary greatly, depending on their feedstock. An increase in the degree of unsaturation results in decreased reactivity, hence a longer ignition delay and a longer premixed phase duration. Increasing the premixed phase duration causes a decrease in PM emissions, however, observations of increased PM emissions due to increased unsaturation are observed [77, 127, 11]. The two opposing effects are not balanced, suggesting that the increase in sooting tendency due to higher degree of unsaturation is dominating over the effect from combustion phasing.

Das et al. [23] measured the yield sooting index (YSI) for several esters with varying structures and chain lengths. The authors found that the introduction of a double bond on the alkane chain of the ester increased the sooting tendency compared to the saturated counterpart. In some cases the increased sooting tendency due to the double bond was even larger than the benefit of having oxygen atoms in the molecule, which was concluded by comparing the YSI of the unsaturated and saturated ester against an equal chain length alkane. The location of the double bond was also observed to have an impact on the sooting tendency [71], where 1-decene with a double bond located at the end, and 5-decene with a centrally located double bond yielded 9% and 52% higher soot volume fraction compared to

[10]Not necessarily true for the fuels tested in [97], since oxygenated fuels generally have higher laminar flame speeds.

n-decane, respectively.

Other properties of biodiesel that changes with an increased unsaturation are: heat of combustion (-), viscosity (-), melting point (-), lubricity (+) [75].

2.4.4 Aromatic content

Since aromatics are highly unsaturated, their presence in a fuel yields lower cetane number and higher tendency to produce soot [161], which are both undesirable in a CI engine. The maximum allowed content of PAH in diesel fuel is 11% by mass (EN 590). An increase in sooting tendency of aromatics is observed for increased branching and increased number of aromatic rings, equivalent to more carbon-carbon bonds and higher unsaturation. In diesel fuel production, aromatics are naturally present in the product. Due to the clear correlation of the aromatics content and PM emissions, authorities have imposed maximum allowed content, forcing producers to lower the aromatic content via hydrotreating [20, 36], which is costly. A consequence of reducing the aromatic content is poorer lubricity and higher cetane numbers. However, improved lubricity can be achieved by adding additives.

2.5 Surrogate fuels

The molecular composition of real fuels can be highly complex, depending mostly on the feedstock, the available production processes, regulations and economics. The feedstock defines the base composition of the fuel, where fuel upgrading can be applied in order to achieve optimal properties. In total, the entire production process must result in being profitable for the fuel company, provide a competitive and high quality fuel to the customer, and at the same time comply to regulations. The fuel standards are set by authorities, which regulate the fuel properties based on pollutant emissions and hardware compatibility. The standards limit key properties of the fuel, and define the level of upgrading a producer must undertake. The resulting fuel composition can therefore vary greatly, only requiring that the specified properties are within the regulated intervals. This poses problems to the research community: firstly, because the fuel is not clearly defined; and secondly, because the composition is too complex for modeling purposes. One way to circumvent this issue is to define a simplified composition, resembling target properties of the fuel. This is often referred to as a surrogate fuel, which depending on the method of investigation, is composed of one to five different molecules. For computational fluid dynamics (CFD) modeling purposes related to combustion, it is mainly limited the kinetic reaction mechanism, where a complex fuel composition requires many species and reactions, making it computationally demanding to perform simulations. Experiments are also important with regards to surrogate fu-

els; since they are used for validation of their kinetic reaction mechanisms, and the use of surrogate fuels in experiments enables comparison of results from different test rigs, avoiding effects due to an unknown fuel composition.

Several surrogates for diesel fuel has been proposed. The most simple and most used surrogate for diesel is *n*-heptane [126], followed by *n*-decane and *n*-dodecane, where detailed high and low temperature reaction mechanisms have been developed [22, 156]. In order to mimic properties like sooting tendency, inclusion of aromatics are needed in the diesel surrogate, where a two-component mixture consisting of an alkane and an aromatic is commonly used. As an example, Lemaire et al. [90] investigated the in-flame soot volume fraction in a turbulent spray flame using diesel fuel and a diesel surrogate consisting of 80% *n*-decane and 20% 1-methylnaphthalene, matching the threshold sooting index (TSI) of the surrogate fuel to the real fuel. Other properties that are important to match are heating value, cetane number, volatility or H/C ratio.

Since EN 590 allows for biodiesel to be blended in diesel fuel, it is important to identify potential surrogate fuels for biodiesel and to study them in detail, see **Article II**.

3. Experimental Setup

The need for detailed measurements of in-flame soot and combustion characteristics led to the construction of an experimental rig with optical access to the high pressure spray flame during the period of 2015-2018 in the Motorlab of the Department of Energy and Process Engineering at the Norwegian University of Science and Technology (NTNU). In addition, the optical techniques used have been adapted to the specific experimental setup and further developed in order to yield trustworthy data. The motivation behind this work is to enable state-of-the-art research on combustion of alternative fuels in CI engines, with the future aim of combining simulations with experimental results in order to elucidate the complex processes inherent in CI spray combustion.

The processes of high pressure spray combustion in engines can be characterized as fast, small in dimension, highly stochastic, and having large spatial and temporal temperature/pressure/density variations. These characteristics make it very challenging to study the flame in CI engines. Optical access to the combustion chamber of a CI engine is hard to achieve, although several research institutions have made such test rigs [102, 151, 87]. The optical engines usually have problems with heat transfer, sooty windows, gas leakage, windows cracking, vibrations, repeatability, etc. In addition, optical access to the combustion chamber of a real engine requires modification of the engine in order for windows to be installed. One usual design is to have a quartz piston crown, enabling optical access to the sprays from below. Additional windows on the sides of the chamber enable light or laser-based techniques such as laser induced fluorescence (LIF) for species concentration measurement, laser induced incandescence or light/laser extinction for soot measurement, where a laser beam or sheet enters through a side window, crosses the spray, and produces signals which can be measured through the piston crown window.

Another alternative used by the engine research community is the constant vol-

ume vessel (CVV). The engine-like thermodynamic condition in the CVV can be achieved from two techniques. The pre-combustion technique uses an ignitable gas mixture that is ignited by a spark, which raises the temperature/pressure/density inside the chamber [124, 117, 82][1]. Thereafter, during the cool down period, fuel is injected when the desired condition has been reached. The repetition rate of the CVV with pre-combustion is usually relatively low (∼600 s between tests [6]). The second approach is to heat the oxidizer inside the vessel with electrical heaters. The latter technique limits the maximum achievable temperature, typically 900 K [6], and requires relatively long time to change between temperature targets.

Instead of a CVV, a constant pressure vessel can be used, where the gas is heated and compressed, and flows through the chamber [130]. This allows for a high injection repetition rate, i.e. 1-3 Hz. However, limitations to the maximum temperature and pressure, long time to switch between temperature targets and high installation costs are major drawbacks [6].

The rapid compression machine (RCM) is a frequently used device for studying high pressure combustion. The RCM has a single cylinder, often with optical access to the combustion chamber, where a single compression stroke generates the engine-like thermodynamic conditions. The repetition rate is limited by the compression stroke's ability to reset itself after a combustion event, making it relatively slow. Today, RCMs are mostly used for accurate ignition delay time and post-combustion species measurement in a premixed charge, which is used for validation of kinetic mechanisms [146]. However, they are also used for spray combustion investigation, where some include the expansion stroke in order to mimic an engine more accurately [132, 143]. Reciprocating rapid compression machines also exist [70, 13, 110], which are usually two-stroke engines fitted with a redesigned engine head, working as the combustion chamber. These enable high repetition rates where the expansion stroke is included.

When comparing optical engines to CVVs, they have higher repetition rates, are generally more similar to real engines in terms of flow field and thermodynamics, have lower thermodynamic repeatability, offer less accurate temperature/density estimation and have poorer optical access. The RCMs in comparison to optical engines generally have lower repetition rates, offer high thermodynamic repeatability, but suffers from vibrations at the end of the compression stroke [6].

For the current work, the choice of building a reciprocating RCM with optical access was made, mainly due to its high repetition rate, the capability of measuring gas concentrations and PM in the exhaust, and the relatively low complexity of

[1]The CVV described by Krivopolianskii et al. [82, 81] is located at NTNU, Department of Marine Technology.

experiment preparation and operation. The original motivation behind the test rig was to enable fuel comparison studies, where fuel switching and measurement with various conditions could be performed in short time. In addition, a big advantage of such a machine compared to an optical engine is that a single free spray combustion event is enabled, whereas in an optical engine, spray-to-spray and spray-wall interactions are present, making it difficult to compare fuels directly to each other. The alternative way of measuring free spray combustion is using CVV, or single stroke RCM, where the above mentioned advantages would not be included.

3.1 Optically accessible compression ignition chamber

The Optically Accessible Compression Ignition Chamber (OACIC) is based on a four-stroke CI engine with a single cylinder, see dimensions and details in Table 3.1. The OACIC is based on a four stroke single cylinder Lister CS engine, where the engine head and the intake/exhaust system are redesigned, see Figure 3.1.

The engine head has two windows allowing for line of sight optical access through the combustion chamber and the spray, where the windows are made out of fused-silica, resulting in 50 mm diameter optical access. The potential candidates for window material were fused-silica, quartz, borosilicate and sapphire. The choice of using fused-silica as window material was made due to its excellent transmittance in the ultraviolet (UV) spectrum, and its properties during thermal loading, where the stresses induced by thermal expansion are less than that of for instance borosilicate [60]. In addition, an investigation using schlieren imaging showed that quartz yielded artifacts in the measurement compared to fused-silica.

The combustion chamber is connected to the cylinder volume via an interchangeable throat, allowing for modification of the flow field and the CR. For the current throat design (see Appendix A.3), the flow field in the chamber close to TDC has shown to have a slight rotational motion. The rotational axis of the flow is parallel to the central axis of the cylindrical chamber volume. In Figure 3.1, the chamber volume is shown, where the bulk flow has a rotational motion rotating counter clock-wise with an angular speed of the $\sim$25°/ms. This was estimated from measurements using the diffuse back-illuminated imaging system with a small aperture, which induces schlieren effects. This measurement only provided a rough estimation.

The OACIC is operated in skip-firing mode, normally skipping 10 cycles, meaning that there are 10 motoring cycles before each combustion cycle. This ensures that no post-combustion gases from previous combustion cycles are present during the subsequent combustion cycle. Due to this, the OACIC is not capable of maintaining stable operation on itself, and is therefore driven by an electrical mo-

tor connected to the crank shaft. In order to obtain a constant speed, a flywheel is mounted onto the crank shaft, providing rotational momentum for the compression stroke. The crank case of the OACIC is not filled with engine oil, as would be expected in an ordinary engine. This is to avoid contaminants to the combustion chamber over the piston rings. Instead, small amounts of lighter lubricants are applied to the cylinder liner regularly.

3.1.1 Fuel system

The installed injector is a solenoid-driven common rail injector from Bosch, fitted with a single hole nozzle with an angle of 62 degrees with respect to the central axis, see Figure 3.1. The high pressure fuel system consists of a fuel pump driven by compressed air, capable of supplying injection pressures up to 1500 bar. The total volume of the fuel system is small, which minimizes fuel waste during fuel switching and requires very small amounts of fuel for testing, allowing fuels of limited quantity to be tested. A minimum total fuel volume of 200-400 mL is needed for a complete combustion test in the OACIC. In order to keep the injector temperature stable, it is water-cooled by a jacket fitted around the injector (not shown in Figure 3.1).

Table 3.1: Specifications of the OACIC.

Engine type	Lister CS, 4-stroke, single-cylinder
Bore/Stroke	130 mm/140 mm
Displaced volume	1.85 L
Compression ratio	15.9
Injector	Bosch CR second generation
Injector nozzle	Single hole 0.12 mm DSLA124P1659 62° wrt. central axis
Engine speed	500-700 rpm

3.1.2 Intake system

In order to achieve thermodynamic conditions similar to that found in real engines, the intake air is boosted and heated. The air is first drawn into a large settling box, which also acts as a volume flow meter, using an orifice plate. Thereafter, the air enters a roots-type compressor, which compresses the air up to a maximum pressure of 1.55 bar. After the compressor, the air is led into a settling tank in order to dampen pressure oscillations caused by the OACIC and the compressor. Before entering the OACIC, the air is heated by a 2 kW electric flow heater, capable of

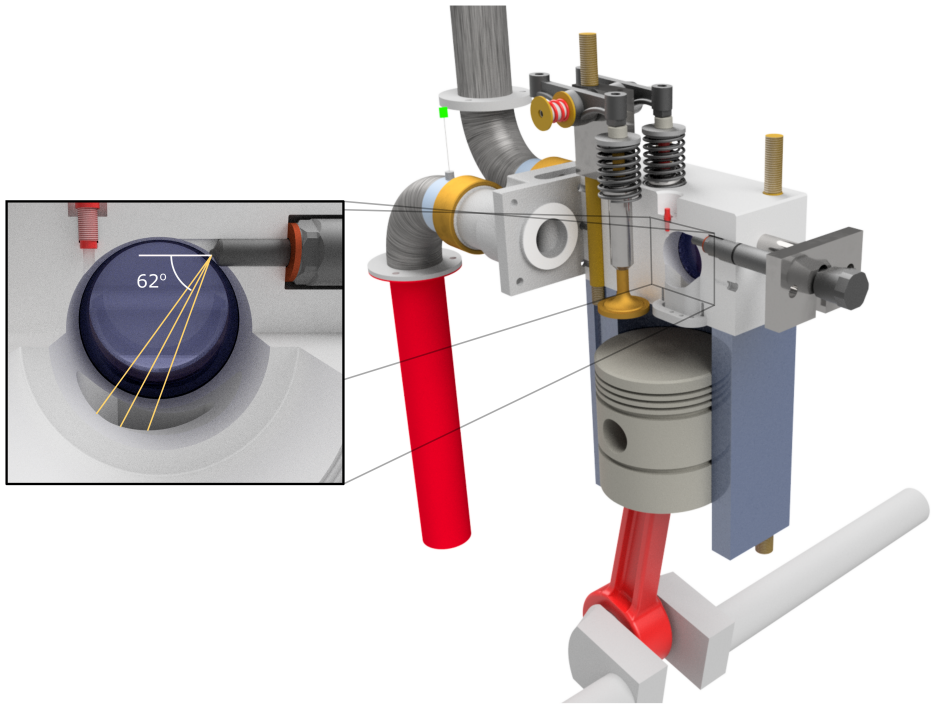

Figure 3.1: The OACIC with a cross-section of the engine head, including a close-up look of the combustion chamber and the location of the spray.

heating it up to 160°C during normal operation.

3.1.3 Sensors and control

Several sensors are installed for operating the rig and to acquire data for analysis. This involves pressure transducers, thermocouples and a shaft encoder. An overview of the most important sensors installed on the OACIC are shown in Table 3.2. The test rig is controlled by LabVIEW via National Instruments hardware, which also handles the data acquisition. The injection is triggered by a predefined position on the crank shaft measured by the shaft encoder, which also triggers other devices such as high speed cameras and backlighting. The shaft encoder reads 3200 signals for one revolution, resulting in a resolution of 0.1125 crank angle degrees (CAD), i.e. 37.5 μs when running at 500 rpm. The intake air temperature and pressure are controlled using PID regulators, ensuring stable intake conditions.

The injection pressure fluctuates during operation due to the fuel pump. In order to increase the repeatability of the injection pressure between each injection, the fuel

injection is only triggered once the injection pressure is within a predefined interval. Measurements performed with target injection pressure of 1000 bar resulted in a measured standard deviation of 20 bar, i.e. 2%, when triggering the injection within $\pm$10 bar.

Table 3.2: Sensors installed on the OACIC. "Synchronized" means that the sample rate is synchronized with the shaft encoder signals. (TC = thermocouple)

Measured parameter	Type of sensor	Sample rate
In-cylinder pressure	Kistler 6052C	Synchronized
Temperature close to chamber wall	Type K TC	100 Hz
Intake air absolute pressure	Kistler 6011	Synchronized
Intake air temperature	Type K TC	100 Hz
Position and speed of crank shaft		3200 reads per rev
Injection pressure		Synchronized
Exhaust gas temperature	Type K TC	100 Hz
Volume flow of intake air	Differential pressure	100 Hz

3.1.4 Thermal management and operation

During operation of the OACIC, the engine head is neither cooled nor heated. The cylinder liner is heated to 90°C by installed cartridge heaters, and constantly kept at this temperature. Before conducting measurements, the OACIC is run until a stable temperature of the engine head is reached, typically close to 100°C for a thermocouple located 21 mm from the internal chamber wall. A typical run when measuring 10 injections lasts for approximately 4 minutes, resulting in the temperature measured close to the combustion chamber wall (21 mm from the wall) increasing slightly over that period, typically $<$20°C. In order to obtain information about the inner wall temperature, separate tests were performed using a modified injector. A thermocouple was installed in the center of the injector body to measure the temperature close to the injector tip during motoring. The temperature reached a stable temperature of $\sim$160 °C after approximately 90 seconds, see Figure 3.2. Hence, the warm up period before combustion measurement was set to 90 seconds.

3.2 Thermodynamic conditions

The thermodynamic conditions in the combustion chamber were estimated using a first law model with ideal gas law, and accounting for piston motion. The software used was LOGEresearch [93], where the temporal development of volume, pressure, temperature and density of the ambient gas are calculated. Input parameters

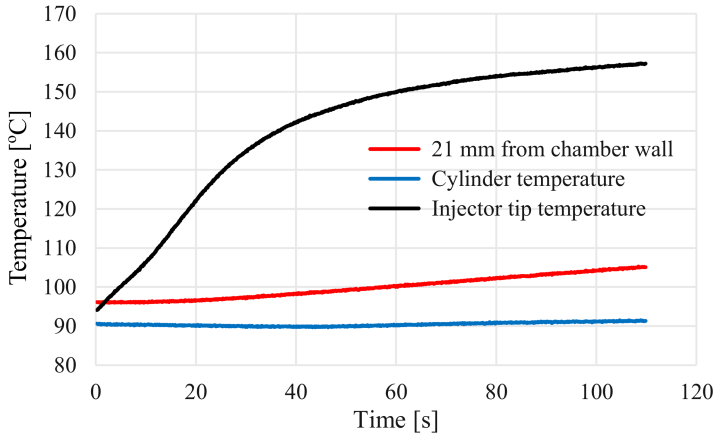

Figure 3.2: Temperature development in the OACIC during operation.

from measurements were in-cylinder pressure, intake pressure, intake temperature, engine speed and engine dimensions.

Figure 3.3 shows the in-cylinder pressure during motoring of the OACIC. The inlet valve closes at 177 CAD before TDC. In the figure, a close up look at the spread of the pressure at TDC is shown, resulting in a 0.09 bar standard deviation for the 361 motored cycles displayed here, which was found to be representative of all conditions. Since the in-cylinder pressure sensor is a differential pressure transducer, it provides a relative pressure, and needs to be matched with an absolute value. The intake pressure is measured in the intake manifold and is a high speed sensor synchronized with the in-cylinder pressure. This allows measurement of the pressure at the time of intake valve closing (IVC), resulting in a relatively accurate measure of the pressure inside the cylinder before the compression stroke starts. The intake air temperature is measured with a low sample speed and is not cycle resolved, resulting in an average inlet temperature measurement. The standard deviation of the measured inlet temperature was 0.2-0.8 K, depending on the temperature setpoint.

The thermodynamic conditions inside the chamber are estimated based on the measured quantities mentioned and a model, where heat transfer from the walls are accounted for using the Woschni correlations. By using the model to calculate the in-cylinder pressure based on the original engine dimensions and the measured thermodynamic condition of the intake air, the modeled pressure always yields a higher pressure than the measured pressure at TDC. The pressure at TDC calculated by the model is higher since air leakage is not included. In order for the

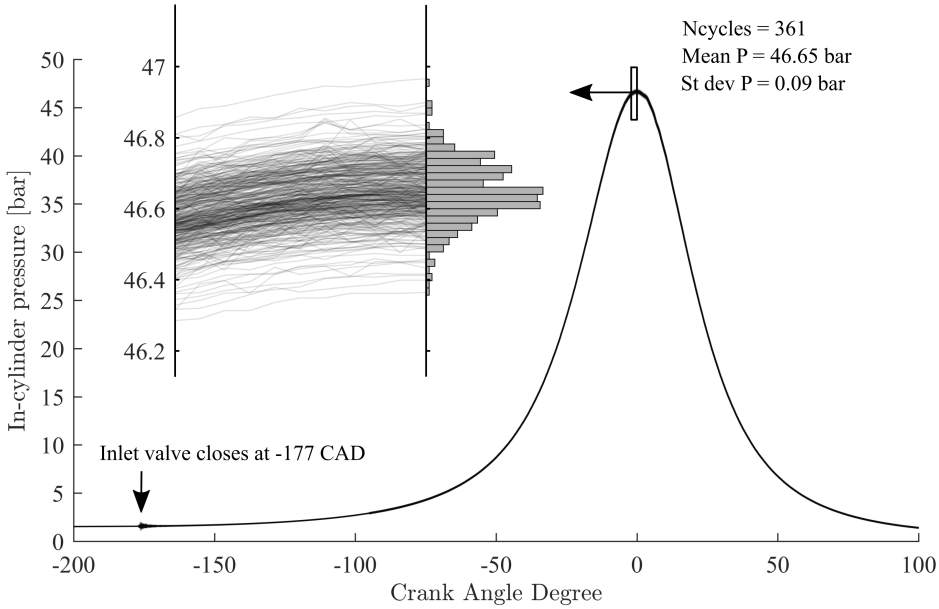

Figure 3.3: In-cylinder pressure in the OACIC for 361 consecutive motored cycles running at 500 rpm. The displayed histogram represents the distribution of the pressure at TDC, having a standard deviation of 0.09 bar.

two pressures to match, the model needs to reduce its air mass during the cycle. Ideally, a mass loss model would be implemented, where transient mass loss during the cycle is accounted for. Instead, reducing the CR was performed such that the modeled and measured pressures matched. This obviously did not result in the correct trapped air mass, but gave a good estimation of the density and temperature in the cylinder near TDC.

This procedure was performed for several conditions, spanning the entire operation range of the OACIC, where the reduced CR needed for matching the pressures was calculated for each run. A constant value of the reduced CR between the different conditions indicated that the relative mass loss was not changing between the conditions. The average value of the reduced CR was then used in the model for calculating the inlet pressure, inlet temperature and in-cylinder pressure needed for the wanted conditions. In this way, the operating conditions for experimental campaigns having for instance constant ambient gas density and varying temperatures were calculated.

The reduction in CR was from 15.9 to $\sim$12.5, meaning that the mass of the air leakage during compression was 20% of the trapped mass in the case of no leakage.

The leakage occurs mainly through the piston ring gaps. The piston ring gaps were found to have an impact on the reduced CR, where larger gaps increased the mass loss, hence resulting in a further reduced CR. The reduced CR can therefore change after maintenance of the OACIC and must be estimated regularly. The resulting conditions for combinations of the highest and lowest possible inlet temperature and pressure are displayed in Table 3.3. The maximum temperature, pressure and density achieved in the OACIC at TDC are $\sim$1000 K, 50 bar and 22.34 kg/m^3, respectively.

The uncertainty related to the calculated ambient gas conditions is based on uncertainties from the individual input parameters: intake temperature and pressure, the total volume of the chamber, heat transfer calculation, in-cylinder pressure measurement, and the estimation of mass loss. As most of the related uncertainties are difficult to evaluate, they are not quantified, but instead described. The inlet temperature is as mentioned measured in the inlet manifold, where an uncertainty based on the thermocouple temperature measurement is present, typically $\pm$1% of the measured temperature[2]. In addition, the air measured in the air manifold is only an estimation of the air temperature inside the cylinder at IVC, where heat transfer from the air manifold walls affects the air as it moves into the cylinder. The inlet pressure also has an associated measurement uncertainty and is equally affected by heat transfer. The heat transfer's effect on the trapped mass at IVC is difficult to estimate. This is likely more significant for low inlet temperatures where the difference between the engine walls and the air is larger, causing heating of the air. The dimensions of the chamber are based on the machine drawings of the OACIC, which might deviate from reality. Errors in the dimensions result in wrong CR input, resulting in wrong pressure at TDC for the modeled case. In addition, the cycle-to-cycle mass loss might vary. The result of the cycle-to-cycle variation in the actual inlet temperature, inlet pressure, mass loss and inlet valve opening and closing is observed as the measured pressure variation. Many of the mentioned uncertainties are difficult to quantify, which makes it difficult to evaluate the total uncertainty on the estimated ambient gas temperature and density at TDC.

3.3 Combustion analysis

As the fuel is injected into the chamber, it mixes with the air and ignites. The combustion process is observed as a pressure rise in the cylinder, see Figure 3.4. The steep increase in the beginning is due to the rapid expansion of the combustion gases, which is a consequence of second-stage ignition. First-stage ignition is characterized by a much smaller heat release rate, and hence a smaller pressure

[2] 95% confidence interval in kelvin [106].

Table 3.3: The span of thermodynamic conditions achievable in the OACIC at TDC. Minimum/maximum achievable inlet temperature and pressure are 30/150°C and 1.0/1.55 bar.

Inlet T [°C]	30	30	150	150
Inlet P [bar]	1.00	1.55	1.00	1.55
T at TDC [K]	777	778	1001	1006
P at TDC [bar]	32.24	50.09	29.76	46.35
ρ at TDC [kg/m^3]	14.4	22.3	10.3	16.0

increase [53]. Ignition delay time is often defined as the time between start of injection and start of second-stage ignition. After the premixed burn phase, the transition to the mixing-controlled burn phase is characterized by a lower heat release rate, consequently having a slower rise in observed pressure. The large oscillations observed are caused by pressure waves created inside the chamber, and not noise from the sensor. The waves are reflected by the walls and affect the pressure measurement severely. The oscillations have the largest amplitude and the highest frequency close to TDC, while they both decay in the expansion stroke, due to the increase in volume. A signal filter, such as Fourier filter, can be applied to the pressure curve in order to smooth the pressure signal. However, care should be taken when applying a filter to the period close to time of ignition, since information about time of ignition can be affected. To overcome this, two types of filters can be applied to the period before and after ignition, thereby preserving the time of ignition in the smoothed signal.

In Figure 3.4, the in-cylinder pressure traces of *n*-heptane for 10 injections along with the mean pressure trace is shown. The pressure-based ignition delay time is defined here as the first large increase in pressure, found from the differential of the pressure increase. In the period between start of injection and ignition, the pressure signal can be seen to drop slightly (not clear in the figure due to the scale). This is due to evaporation of the fuel spray, which requires heat, hence affecting the pressure.

In order to calculate the apparent heat release rate (AHRR) of the combustion process, the measured pressure signal needs a filter applied. The AHRR calculated from the observed pressure equals the difference between the heat release rate from combustion and the heat transfer rate to the walls. The procedure for calculating the combustion heat release rate can be found in Heywood [51].

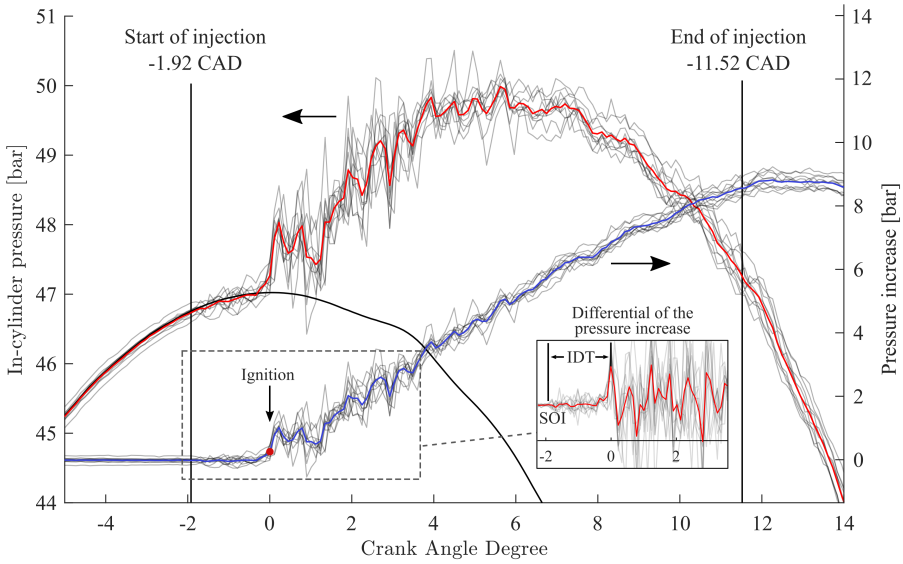

Figure 3.4: Combustion in the OACIC with *n*-heptane as fuel. The red curve shows the calculated mean in-cylinder pressure for 10 combustion cycles, the blue curve shows the mean pressure difference between the combustion cycles and the motored cycles. Injection pressure of 1000 bar, injection duration of 4.48 ms, inlet pressure 1.555 bar, inlet temperature of 408 K, pressure at TDC for the motored pressure 47.02 bar. The calculated thermodynamic condition in the chamber was 979 K and 16.6 kg/m^3.

3.4 Exhaust analysis

On the exhaust manifold of the OACIC, sample ports are installed, making it possible to analyze exhaust gases and PM. Two analyzers were available for this measurement, the Horiba MEXA-ONE-RS for exhaust gas concentrations and the Cambustion DMS 500 for PM. Both analyzers are equipped with heated lines, and have a relatively fast sampling rate of approximately 1 Hz.

As mentioned, under normal operation, the OACIC is skip-fired. This poses a problem to the measurement of the exhaust gases, since the exhaust analyzers are not able to resolve each cycle. Hence, the measurement becomes an average of the cycles, including combustion and motored cycles. If the number of skipped cycles between each combustion cycle is fixed, a method for estimating the actual exhaust gas and PM concentrations for a single combustion cycle can be applied. This method is described by Donkerbroek et al. [31]. However, this technique is hard to implement in the OACIC, since the skip-firing does not have a fixed interval due to the unstable injection pressure. For instance, after skipping 10 cycles, it waits

until the injection pressure is within the predefined range before injecting, resulting in skipping a minimum of 10 cycles. A compromise could be done where the "wait for injection pressure" function is turned off, resulting in a fixed skipping interval. However, this results in a large variation of the injection pressure between the combustion cycles. The most obvious solution to this would be to fire the OACIC continuously, however, the high heat transfer from combustion increases the wall temperature in the chamber quickly, making the measurement erroneous, and can also cause damage to the OACIC.

The Horiba analyzer is equipped with four analyzers for measuring CO/CO_2, O_2, NO/NO_x and THC concentrations. The analyzers' methods and ranges are given in Table 3.4.

Table 3.4: Analyzers installed in the Horiba gas concentration analyzer.

Gas measured	Method	Range
CO/CO_2	Non-dispersive intrared	0-20 vol-%
O_2	Magneto-pneumatic detection	0-25 vol-%
NO/NO_x	Chemiluminescent detector	0-10.000 ppm
THC	Flame ionization	0-60.000 ppm (carbon-based)

The PM analyzer is capable of measuring the PM size distribution and the total number of particles in the exhaust stream. The analyzer uses a differential mobility spectrometer, which is based on the principle of measuring how far charged particles travel in an electrical field. Traveling inside a column, their paths are deflected, causing them to collide onto electrometers. The distance traveled by the particles is a function of the charge on the particle and the aerodynamic drag, which is used to determine the size of the particle in terms of the mobility diameter.

Along with knowing the number of particles measured for each size interval, a size distribution is obtained. The Cambustion was installed on the OACIC. However, a large number of particles with very small diameters was measured, which was not consistent with PM measurements done in a conventional CI engine. These particles were suspected to originate from the cylinder lubricant. The main problem with the small diameter peak was that it was highly inconsistent, changing in character between runs and even during a run. In future work, experimentation with different cylinder lubricants should be performed, in order to eliminate the small diameter peak.

4. Optical Techniques

The previous chapter described the experimental test rig, where optical measurements are made possible in CI spray combustion. The current chapter provides a short overview of techniques that are commonly used for measuring in-flame soot. Following the review, the optical techniques used in this work are presented, including diffuse back-illuminated extinction imaging (DBIEI) and OH^* chemiluminescence imaging.

4.1 Measurement of in-flame soot

For measuring in-flame soot, optical techniques like natural luminosity measurement, two-color pyrometry, planar laser induced incandescence (PLII) and laser/light extinction, can be applied. The principles of the mentioned techniques are based on radiation emitted from the hot glowing soot particles, while extinction is based on attenuation of incident radiation. PLII is the only technique which is considered intrusive, i.e. the in-flame soot is affected by the measurement, which could result in measurement bias.

4.1.1 Natural luminosity

In literature, for measuring in-flame soot, natural luminosity is most commonly used as it is inexpensive and easy to apply. Natural luminosity is also referred to as natural incandescence, broadband radiation of soot or flame luminosity. The measurement consist simply of measuring the broadband radiation emitted by hot glowing soot particles present in the flame, i.e. the flame luminosity. However, when imaging a flame, one should be aware of the impact of self-absorption, where the light emitted by particles inside the flame are attenuated by surrounding particles. Hence, the measured light is the result of light emission and absorption of all particles in the flame [116]. The spectrum of the flame is broadband, meaning that it covers the entire visible wavelength range. In addition to soot incandescence, gas phase radiation is also present, mostly by water and CO_2 in the infrared spectrum

[38], while soot radiation is dominating in the visible spectrum. This technique gives a qualitative measurement of the amount of soot present in the flame and should not be directly linked to quantitative data such as soot volume fraction. The natural luminosity signal read by the sensor is a function of soot volume fraction and temperature. The signal is proportional to the soot volume fraction, but has a strong non-linear relation to the soot temperature [99], where the hottest particles give the strongest signal. This creates a bias in the measurement where for instance a flame with same soot volume fraction, but different adiabatic flame temperatures, yields a higher natural luminosity signal for the hottest flame.

4.1.2 Two-color pyrometry

Two-color pyrometry measures the temperature and optical density of soot particles. The technique is based on the soot particle emissivity, which is the ratio between the gray body and the black body emissive power, where the emissivity is a function of the particle temperature. The emissivity can be related to the optical density for a certain wavelength through an empirical relation found by Hottel and Broughton [56]. This relates the temperature of the particle to the optical density. By measuring the flame in two wavelengths, the temperature can be calculated, which in turn is used for calculating the optical density. A full explanation can be found in [167]. In order to calculate the temperature of the soot particles, a calibration of the sensor using a black body emitter with known temperature must be performed, which introduces new sources of error. The empirical relation is also a limiting factor, where a model constant is dependent on the size and refractive index of soot and the light wavelength, requiring careful consideration. In addition, the same issue of self-absorption as mentioned above applies, where a thorough assessment must be made in order to achieve reliable quantitative results [116].

4.1.3 Planar laser induced incandescence

The advantage of the two techniques mentioned above is that they both can be applied in experimental rigs with limited optical access. However, if the optical access to the combustion chamber is good, PLII can be applied. PLII is based on using a laser sheet in order to heat soot particles to temperatures much higher than the combustion induced temperature. In this way, the laser induced incandescence becomes much stronger than the natural luminosity, such that a CCD/CMOS sensor only detects the particles subjected to laser radiation. An accurate physical model including optical properties of the measured soot is needed in order to obtain the soot volume fraction and primary particle size distribution in the two-dimensional plane [133]. Common issues related to PLII are interference of PAH fluorescence excited by the laser, unwanted non-linearity between laser induced incandescence signal and soot volume fraction, the influence of the laser sheet

profile on the laser induced incandescence signal as a function of laser energy, and signal trapping [136]. A big advantage of using PLII for soot measurement is that it provides a two-dimensional local soot volume fraction measurement. The biggest disadvantage of applying PLII to CI spray combustion is that the repetition rate is low, which is limited by the laser. In addition, this technique is intrusive, since the soot particles are heated by the laser, causing them to experience sublimation, consequently reducing particle size. PLII has been used in diesel engine studies [80, 27, 87], but is usually limited to a single measurement per combustion cycle because of the low repetition rate.

4.1.4 Light extinction

Due to the limited temporal resolution of PLII, alternative techniques have been explored by the engine community over the past years, where a reliable, quantitative, two-dimensional and high-speed measurement of soot was desired. Two-dimensional DBIEI was found to be a suitable technique, but needed further developing for CI spray application. The technique is based on extinction of light, where the light source entering the combustion chamber is diffused in order to eliminate beam steering effects, also known as schlieren effects. Previous development and application of DBIEI have mainly been for laminar diffusion flames under atmospheric pressure [46, 141, 162], where the issues related to beam steering was less severe than for high pressure turbulent flames. Beam steering issues in diesel spray combustion application were studied for laser extinction by Musculus and Pickett [101], where a laser beam through the soot cloud was investigated. Beam steering effects were also highlighted as an issue when DBIEI was applied to liquid penetration length measurements [125, 95], where the fuel vapor at the liquid spray tip caused problems in defining the liquid penetration length. The same group applied in 2013 the DBIEI technique to soot measurements [96, 139], inspired by the optical setup for diffuse back-illumination by Ghandhi and Heim [39], high speed measurement of soot was achieved, although beam steering was still not completely abated. The problems of beam steering in DBIEI in diesel sprays were thoroughly addressed by Westlye et al. [158], which provided a theoretical framework for dealing with them. More details regarding beam steering effects are included in Section 4.2.3 and **Article I**.

In order to obtain the soot volume fraction from a DBIEI measurement, an ensemble averaged measurement must be performed. The ensemble-averaged line-of-sight measurement of the soot optical density can be considered as axisymmetric, which in turn allows for a tomographic deconvolution [24]. A comparison between two deconvolution techniques; inverse radon and onion-peeling, is provided in [163]. The deconvolution yields the local dimensional extinction coefficient distribution, which in turn can be used for calculating the local soot volume fraction.

Additional uncertainties are added when converting to the soot volume fraction, since it requires optical and physical knowledge of the soot particles measured [137]. In addition to beam steering, uncertainties connected to the strong influence of flame luminosity on the measurement are important to be aware of. As the soot volume fraction is based on an ensemble-averaged measurement, the easily obtained ensemble-averaged flame luminosity can be used in order to correct for the influence. However, for measuring instantaneous optical density distributions, the flame luminosity must either be corrected for or completely suppressed by filters by having a high flame luminosity to light source intensity ratio (I_f/I_0). From the instantaneous optical density distribution of soot, the total soot mass can be also be calculated [138].

As mentioned, the optical density of soot can also be measured by two-color pyrometry. A comparison between two-color pyrometry and DBIEI is provided in [115, 164]. The main conclusion reached in these studies was that two-color pyrometry generally shows a lower optical density of soot compared to DBIEI due to self-absorption within the flame, where self-absorption was especially strong for high values of optical density. DBIEI was therefore concluded to yield the most reliable quantitative data compared to two-color pyrometry. Interesting work was conducted by the same research group, where Xuan et al. [163] combined the methodologies of two-color pyrometry and DBIEI in order to simultaneously measure the soot volume fraction and flame temperature.

4.2 Diffuse back-illuminated extinction imaging

As illustrated above, DBIEI for measuring soot in high pressure CI sprays is a relatively new technique, where optimization is still needed. The setup requires no calibration, but highly accurate alignment and characterization of the optical setup, which is crucial for yielding satisfactory results. This section briefly explains the issues related to the technique and how they were resolved for the current work. More details can be found in **Article I**.

The technique is based on using a diffused light source as back-illumination. The light is directed through the combustion chamber, which gets attenuated by the soot particles in the flame, and is measured by a CMOS sensor on the opposite side of the chamber, requiring a line-of-sight optical access through the chamber. The attenuation occurs as a result of light scattering and absorption. The optical density[1] (KL) can be calculated by the Beer-Lambert law [14] from the transmittance, i.e. the ratio between the transmitted and the incident radiance of the

[1] KL is the product of the path-averaged dimensional extinction coefficient K and the path length L.

light (I_t/I_0), see Equation 4.1. The soot volume fraction (f_v) can be calculated based on knowing the local dimensional extinction coefficient k. See Zhao and Ladommatos [167] for derivation of the relation between optical density and soot volume fraction, given in Equation 4.2. As mentioned, optical and physical properties of the measured soot are needed, i.e. the dimensionless extinction coefficient k_e. A detailed evaluation of these properties for soot typically present during the quasi-steady period in CI diesel sprays can be found in [137].

$$\tau = I_t/I_0 = e^{-\int_L k(x)dx} = e^{-KL} \tag{4.1}$$

$$f_v = \frac{K\lambda}{k_e} \tag{4.2}$$

The current optical setup is shown in Figure 4.1 and an overview of the optical components used is given in Table 4.1. The light emitting diode (LED) light is collected by two small condensing lenses, which direct the light onto a collimating lens. The collimated light is thereby directed onto the engineered diffuser, which diffuses the light. The working principle of the engineered diffuser is that microlenses on the diffuser surface uniformly spread the light within a specific angle, in this case 15°. The exit distribution has been observed to be very sensitive to the incoming angle of the light, emphasizing the importance of characterizing the output light distribution. The diffused light is further guided through the chamber and is measured by the camera. The characterization of the light distribution and why it is important, is addressed in Section 4.2.3.

4.2.1 Light source

The light source used was a red LED (628 nm). In DBIEI, the light source should be as powerful as possible, such that the ratio between the incident light intensity and the flame luminosity becomes as large as possible. In this way, the flame luminosity will have less of an impact on the measurement. This can be achieved in two ways, either by filtering of the LED and flame luminosity light, or by increasing the power of the LED.

When choosing filter for the objective lens, it should be as narrow as possible and centered with the LED wavelength distribution. The aim is to maximize the LED light throughput, while minimizing the broadband flame luminosity, see Figure 4.2. The figure shows two bandpass filters used in this work, where filter 1 has a wide bandwidth of 70 nm FWHM[2], while filter 2 has a narrow bandwidth of 10

[2] full width half mean

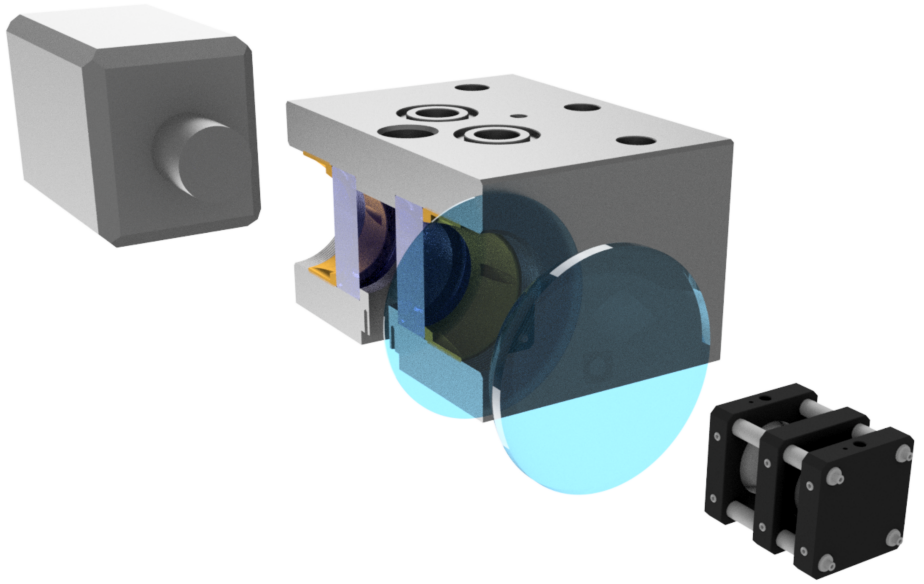

Figure 4.1: The optical setup used for DBIEI.

nm FWHM. When filtering the LED and flame light with the filters, the light transmitted to the camera is given in the lower graph, where the wavelength distribution of the LED and flame light can be compared. Integrating these curves results in the total radiation received by the camera. Comparing the ratio between the LED light and the flame luminosity for filter 1 and 2, one can see that filter 2 has a 3 times higher ratio, i.e. 0.92 versus 0.31, meaning the flame light is suppressed by a factor of 3 compared to filter 1. This was also confirmed by measurements of the flame luminosity, comparing the LED light with the flame luminosity for both filters.

Increasing the power of the LED light is the most important step. In this work an in-house LED driver was designed based on the work of Willert et al. [159, 160]. The LED driver is essentially a pulse generator, which allows high current to pass through the LED over a very short duration, and where the ramping up and down times are relatively short compared to the pulse duration. The measured current flowing through the LED during nominal operation in pulsed mode was in the magnitude of 100 A. Normal pulse duration was in the order of 1-2 μs, pulsing at a frequency of 50 kHz, equating to a duty cycle of 5-10%. According to the specifications of the LED, the current passing through the LED is far above its rated current, which according to the manufacturer might cause irreversible damage to the LED. However, since the duty cycle is kept relatively low and the LED is only

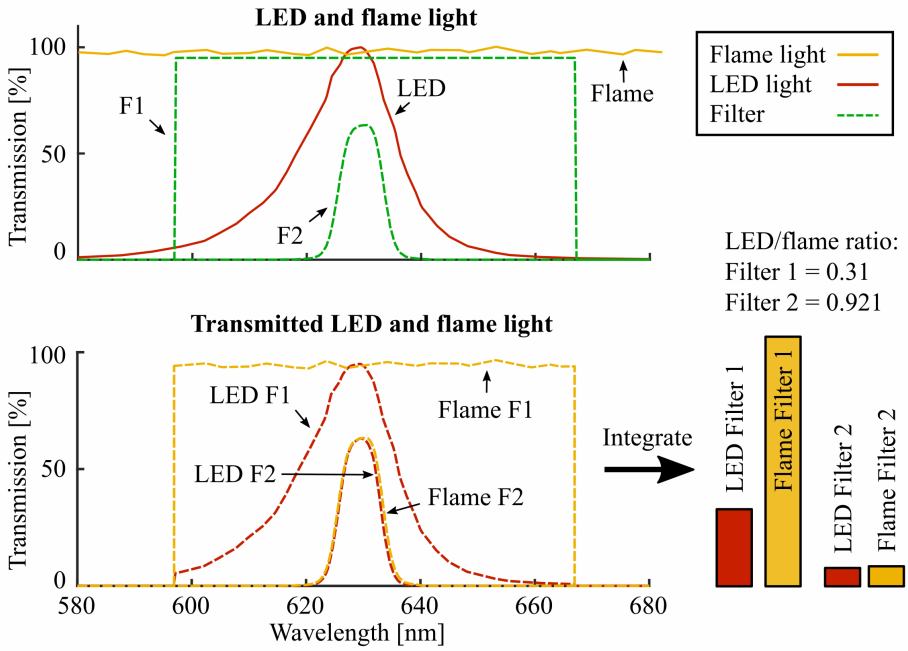

Figure 4.2: Upper graph: the wavelength distribution of the LED light, the flame luminosity, filter 1 transmission (F1) and filter 2 transmission (F2). Bottom graph: the corresponding transmitted LED light and transmitted flame luminosity with using filter 1 and filter 2, respectively. Integrating the curves in the bottom graph results in the bar plot displayed on the bottom right-hand side, showing the total radiation received by the imaging sensor from the flame and LED after being filtered by filter 1 and 2. Filter 1 = FWHM 70 nm and filter 2 = FWHM 10 nm.

pulsed for a short time duration, i.e. 5-10 ms, it does not get overheated. See Appendix A.2 for more information about the design.

Another important aspect of the light source is stability over time and between cycles. The DBIEI measurement requires an incident light image in order to calculate the optical density, i.e. I_0. The variation in the incident light and the transmitted light due to LED instability can be considered as random error. This can be quantified by investigating the stability of the LED, shown in Figure 4.3. The LED intensity drops to about 96% of the initial intensity after 6 ms. However, the drop is consistent, only having a relative variation of 0.2% from the mean curve. The deviation from the mean intensity curve for the transmitted and incident light results in an uncertainty on the calculated KL. Assuming the extreme cases of $\tau = (0.998I_t)/(1.002I_0)$ and $\tau = (1.002I_t)/(0.998I_0)$, they result in an uncertainty of ± 0.004 on the calculated value of KL, which can be neglected.

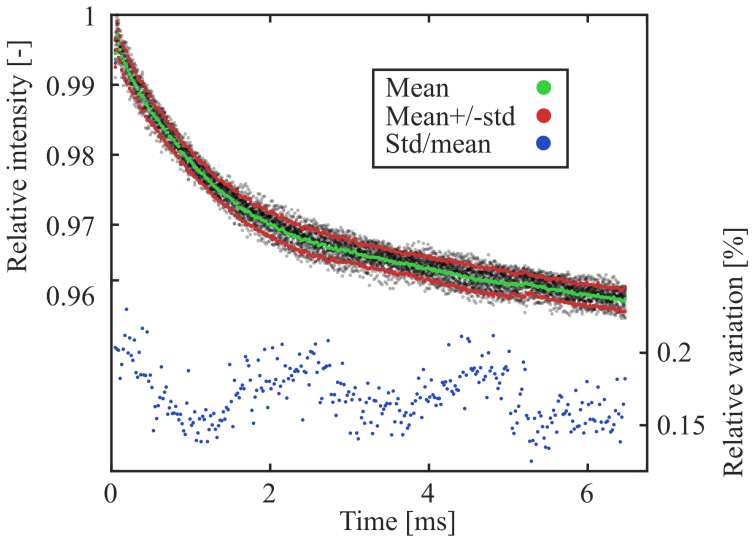

Figure 4.3: The intensity level of the LED during nominal operation for 20 cycles. The relative variation is given as the sample standard deviation divided by the mean curve, showing a maximum variation of 0.2%.

The choice of center wavelength of the LED is also important to consider. For instance, the flame luminosity is stronger in the green spectrum compared to the red spectrum, which motivates the choice of using a red filter, hence a red LED. The optical density of soot is also wavelength dependent, where light with shorter wavelengths has a lower transmittance through a particle cloud. DBIEI will therefore have a more restricted soot concentration measuring range for shorter wavelengths. This can be investigated by comparing two KL measurements having different light source wavelengths, i.e. λ_1 and λ_2, resulting in $(KL)_1$ and $(KL)_2$, respectively. If the same flame is measured, the soot volume fractions of both measurements are the same and Equation 4.2 can be used to derive:

$$\frac{(KL)_1}{(KL)_2} = \frac{k_{e,1}}{k_{e,2}} \frac{\lambda_2}{\lambda_1}. \tag{4.3}$$

By assuming that k_e is the same for both wavelengths, Equation 4.3 shows that $(KL)_1/(KL)_2$ becomes higher when $\lambda_1 < \lambda_2$. Comparing green light (λ_1 = 520 nm) with red light (λ_2 = 628 nm), the ratio becomes 1.21, meaning that KL is 21% higher for the green light, which in turn is a lot for a high sooting flame, since the scale is logarithmic. As an example, if $(KL)_2$ = 4, then $(KL)_1$ = 4.84, which equates to a transmittance of τ_2 = 1.8%, and τ_1 = 0.79%, which is 2.3 times less

transmitted light when using green light as the light source. In addition, gas phase molecular absorption of large PAH can occur for shorter wavelengths, therefore motivating the choice of having longer wavelengths [50]. However, the k_e has been shown to be wavelength dependent [96, 137], where $k_{e,1} < k_{e,2}$ for $\lambda_1 < \lambda_2$, which to some degree counterbalances the increase in KL. Based on these positive effects on DBIEI when choosing longer wavelengths, combined with the thorough analysis of the optical properties of soot at 623 nm by Skeen et al. [137], the choice of using a red LED was made.

4.2.2 Flame luminosity correction

Despite the efforts of increasing the power of the LED and the careful choice of filter, a complete suppression of the flame luminosity influence on the measurement was not achieved. For high sooting flames, this is very hard to achieve, and requires a very high power light source in order to have flame luminosity levels below the read noise level of the camera, 0.2-0.4% of the dynamic range (10-15 counts out of 0-4095 counts, i.e. 12 bit camera). This means that the LED backlight read by the camera must have a 300-400 times higher intensity than the maximum flame luminosity intensity. In the current optimized setup, the camera reads approximately 5-10 times higher intensity for the LED backlight compared to the flame, which is for the highest sooting case, i.e. using diesel fuel at the hottest condition (Figure 4.4). This poses a problem to the measurement, since the flame luminosity is superposed to the transmitted signal. Techniques for correcting flame luminosity effects are presented in **Article I**.

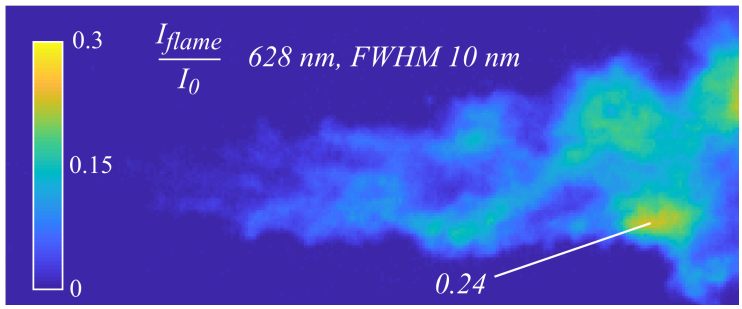

Figure 4.4: The ratio between flame luminosity and the incident backlight (I_f/I_0), for the highest sooting case using diesel fuel. The maximum value of I_f/I_0 in this frame was 24%.

4.2.3 Beam steering

The use of a diffused backlight is an important aspect of DBIEI. In high pressure combustion chambers with flames, large density gradients are present due to large

temperature gradients, which are equivalent to large refractive index gradients. According to Snell's law, when a light beam travels between two substances with different refractive indices, the speed of light changes. If the light beam has an incident angle relative to the normal of the boundary, a change in direction at the transition occurs. This is the fundamental principle behind the techniques schlieren and shadowgraphy, which are used for detecting density gradients in gases. For DBIEI, this effect is unwanted, since it induces false attenuation which cannot be distinguished from the optical density observed due to extinction of soot. One way to abate beam steering effects is to use a diffused backlight, see Figure 4.5.

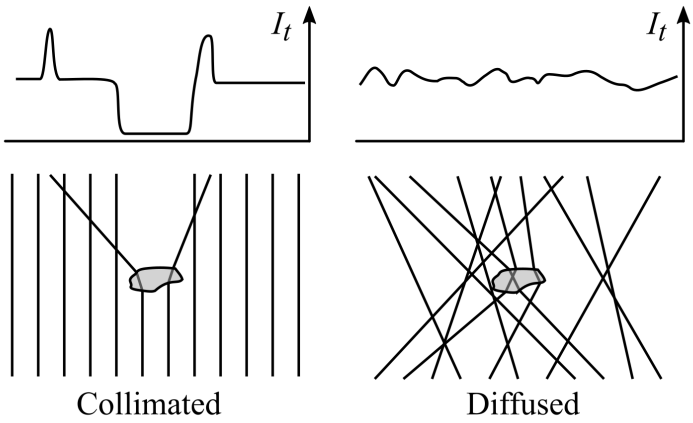

Figure 4.5: Conceptual illustration of a collimated and diffused light source, where a density gradient is present, deflecting the light beams. I_t is the resulting light intensity observed on the opposite side.

The diffused light can be viewed as a collection of light beams with arbitrary angles, while collimated light is a collection of light beams that all have the same angle. If a substance, which creates a refractive index gradient, is placed between a white wall and a collimated light source, it will be visible on the wall as a "shadow", because the parallel light beams passing through the substance are deflected from their original path. For the same case, but having a diffused light source, the substance is not visible on the wall, since the deflected light beams are replaced by other light beams.

In DBIEI, characterization of the diffused light source is necessary. Westlye et al. [158] concluded with help of a theoretical framework, that the diffused light source should be extended, spatially uniform with a constant radiance, and have constant radiance of all angles within the spreading angle of the engineered diffuser. In order to verify this for the current setup, a measurement of the angular radiation

distribution was performed and is presented in **Article I**. The acceptance angle, limited by the objective lens, was also measured in order to dimension the setup accordingly.

When considering the light collected by a single pixel on the imaging sensor, this is determined by the acceptance angle (also called collection angle). The acceptance angle is the angle subtended by the aperture diameter and the focal point in the measurement plane, hence this angle is set by the focal distance and the aperture diameter. The light read by the pixel is therefore received from an area on the diffuser surface, which is determined by the distance from the focal plane to the diffuser surface and the acceptance angle. As the light is subjected to density changes in the chamber, the light is redirected from its original path, which results in light being received from another part of the diffuser surface, and at a different angle. If the displaced collection area on the diffuser has the same radiance as the original collection area, i.e. before it was steered, it will not affect the total intensity read by the pixel for the steered case. However, if the radiance in the displaced area on the diffuser is different than the original, this will be read as a variation in intensity. Therefore, it is important to design the setup according to the expected level of beam steering, which essentially determines the minimum spreading angle of the engineered diffuser.

Figure 4.6 shows two measurements of a sootless premixed combustion using the DBIEI, with aperture of f/1.2 (wide aperture) on the left hand side and f/5.6 (narrow aperture) on the right hand side. The corresponding images below show the intensity variation calculated from the difference between a combustion image and a non-combustion image, for the wide and narrow aperture, respectively. The narrow aperture case shows how the measurement is highly affected by the large density gradients present inside the chamber, while the wide aperture case shows no intensity change due to combustion. Additionally, beam steering effects can be observed for the wide aperture case along the periphery of the measurement domain, which is due to a nonuniform angular distribution in this region caused by the walls. This emphasizes the importance of understanding and characterizing the optical setup for DBIEI measurements.

4.3 OH* chemiluminescence imaging

As mentioned in Chapter 2, the in-flame soot production during the mixing-controlled period is dependent on the amount of air mixed in prior to ignition at the flame light-off length. Ignition points in the flame can be defined as high heat release zones, which burn at near stoichiometric conditions, and consequently under high temperatures [52, 134]. The stoichiometric zones in a typical hydrocarbon flame burn with such high heat release rates that ground state hydroxide (OH) is elec-

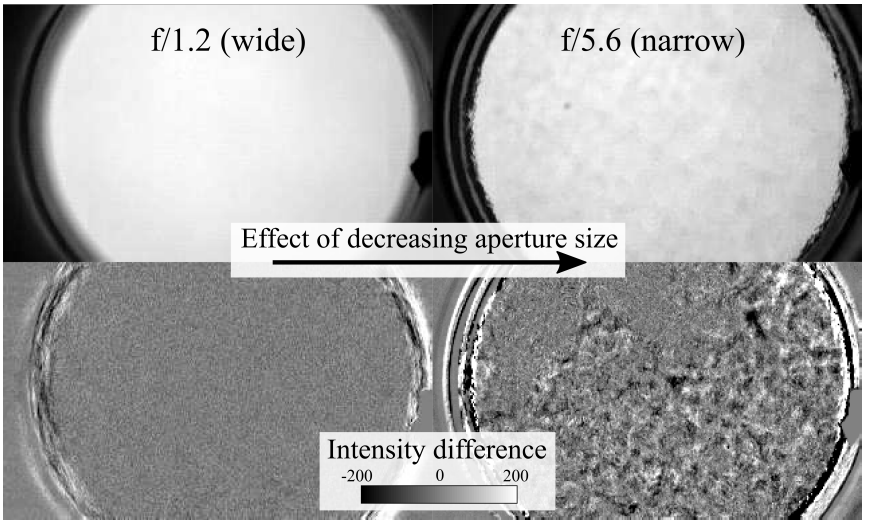

Figure 4.6: The effect of beam steering when changing the aperture of the objective lens from wide to narrow, measuring the diffused backlight during sootless premixed combustion. The top images shows the diffuse backlight through the chamber measured with wide and narrow aperture for the same combustion mode. The bottom images show the difference in intensity from a combustion case to a non-combustion case using the wide and narrow aperture.

tronically excited, primarily through the reaction $CH + O_2 \rightarrow CO + OH^*$. As OH^* returns to the ground state OH, an emission is released, also known as chemiluminescence. The time scale of this process is in order of 1 μs, typically faster than transport processes, making it a well-suited marker for the high heat release rate zones in the flame [38]. A thorough analysis of the determination of FLOL in a CI spray is given in [52]. They conclude that 310 nm natural luminosity, i.e. measuring the OH^* chemiluminescence, is an excellent marker for FLOL. More details on the definition of the FLOL and the light based ignition delay time used in the current work are provided in **Article II** and **Article III**.

In this work, a gated image intensifier was used to image the flame in the narrow UV light spectrum of 310 nm 10 nm FWHM. The OH^* chemiluminescence measurement was synchronized with the DBIEI, where the same field of view was imaged via a dichroic mirror[3]. With help of image alignment calibration, the two measurements were overlaid, making it possible to analyze both in-flame soot production and high heat release zones simultaneously. For instance, this allowed for a frame-to-frame analysis of the transient effects of the FLOL on soot produc-

[3]reflecting wavelengths above 500 nm and transmitting below 500 nm.

tion. In addition, a light-based ignition delay time could be determined from this technique, following the definition provided by Lillo et al. [92].

As an example, Figure 4.7 shows a simultaneous measurement of OH* chemiluminescence and KL between 1.74 ms and 2.3 ms after start of injection for *n*-heptane.

Table 4.1: List of optical components used in the setup. Note that the listed components are the components that yielded the best result, and are not used in all the campaigns included in this work. R = reflected light, T = transmitted light.

Component	Manufacturer/Name	Specification
DBIEI components		
Photodiode	Thorlabs/PDA36A-EC	350-1100 nm
LED	Luminus Devices/SST-90-R	628 nm, 15 nm FWHM
Aspheric lenses	Thorlabs/ACL25416U-A	25 mm diam
Collimating lens	-/-	100 mm diam, f/1.0
Engineered diffuser	RPC Photonics/EDC-15-15132-A	100 mm diam, 15°
Fused silica windows	UQG/Spectrosil	62 mm diam
Beamsplitter	Knigth Optical/BAE14507	VIS, R= 50%/T= 50%
High speed camera	Photron/FASTCAM SA1.1/SA5	-
Objective lens	Nikon/Nikkor	50 mm, f/1.2
Close-up lens	Canon/-	500 diopters
Bandpass filter	Knight Optical/630DIB50	630 nm, 15 nm FWHM
Neutral density filter	Hoya/-	OD 2-8
OH components*		
Gated intensifier	Lambert Instruments/HiCATT 18	-
UV objective lens	Nikon/Nikkor	105 mm, f/4.5
Dichroic mirror	Knight Optical/500FDL1500-C	R<500 nm, T>500 nm
Bandpass filter	Edmund Optics/34-980	310 nm, 15 nm FWHM

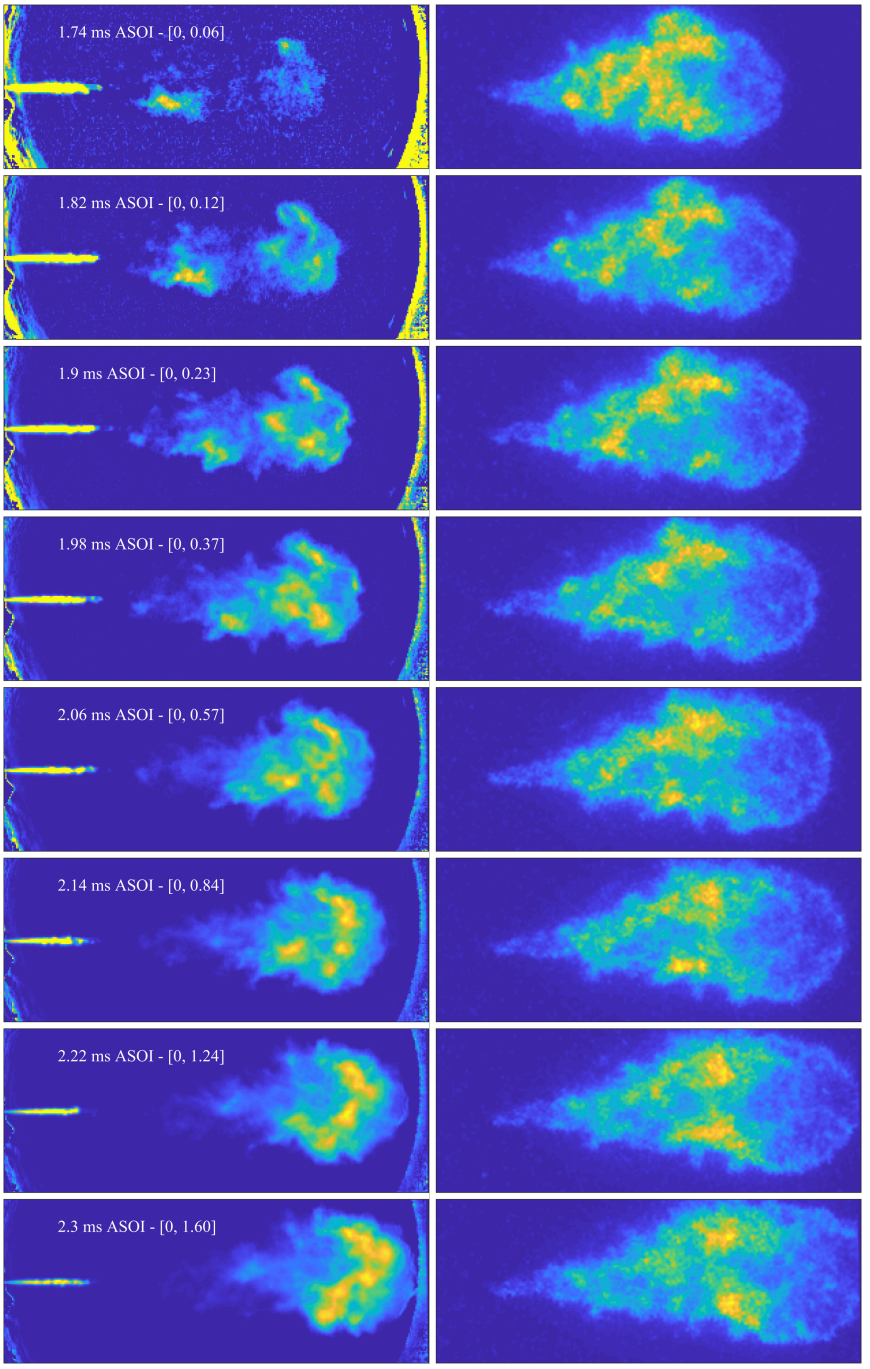

Figure 4.7: Measurement of KL (left) and OH* chemiluminescence (right), showing soot production during the premixed phase for *n*-heptane for 990 K, 16.6 kg/m^3 and 46.7 bar in air.

5. Summary of Results

This chapter presents a summary of the findings in the selected articles, which form the basis of the doctoral work.

5.1 Article I - Diffuse Back-Illuminated Extinction Imaging of Soot: Effects of Beam Steering and Flame Luminosity

This study presents important diagnostic aspects of the technique DBIEI, including a methodology for effectively eliminating flame luminosity effects on DBIEI of soot in high pressure spray flames, and assessing the influence of beam steering effects on the measurement of soot optical density (KL). The study has been performed in the OACIC, where diesel fuel has been used as a benchmark case for two ambient gas conditions, i.e. constant density with a high and low gas temperature, creating high and low sooting cases, respectively.

Both flame luminosity effects and beam steering effects become very influential for high sooting flames in DBIEI, where the level of light originating from the back-illumination reaches the noise level of the camera, making it very sensitive to errors. The light received by the camera is the sum of the LED light and the flame luminosity, where the flame luminosity part is unwanted. In order to only obtain the soot sensitive part, i.e. LED light intensity in the measured signal, the flame luminosity needs to be eliminated. In this study, two existing techniques are compared to a newly developed technique for flame luminosity correction.

For measuring the optical density of soot in the CI spray flame, high speed cameras are used. A pulsed high power LED generates the backlight needed for measuring KL. The LED is pulsed for every second camera frame, resulting in measuring the flame luminosity before and after every light extinction frame. The existing techniques utilize these flame images to estimate the flame luminosity distribution

during the extinction measurement. The first method calculates the mean flame luminosity image of these, while the second method uses optical flow algorithm to predict the location of the flame luminosity distribution during the extinction measurement.

Unlike the previous techniques, the two-camera method measures the flame luminosity distribution using a separate high speed camera. The second camera is synchronized with the main camera, and is imaging the same field of view via a beamsplitter. By adding a small time delay to the main camera compared to the second camera exposure, and triggering the LED pulse such that only the main camera is exposed to light, the second camera measures the flame luminosity distribution close to the extinction measurement. Since the time delay is small, the flame luminosity measurement is similar to that influencing the extinction measurement and can therefore be used for correction.

Since the two measurements are slightly misaligned and are of two different image sensors, post-processing including alignment and brightness correction is needed. This is achieved by transforming the second camera's flame luminosity image before the extinction image such that it fits the main camera's flame luminosity image before extinction, and then applying the same changes to the second camera's flame luminosity image during extinction measurement. The transformed flame distribution obtained by the second camera is then used for correcting the extinction image measured by the main camera.

In order to assess the performance of the three techniques, measurements with no backlight were conducted. In this way, the actual flame luminosity distribution during extinction could be measured, and a direct comparison with the estimated flame luminosity could be performed. This resulted in the mean image being the least accurate prediction of the flame, followed by optical flow, which yielded 18% lower errors than the mean image, and the two-camera method yielding 50% lower errors than optical flow. This was independent of the flame luminosity level, i.e. the sooting level of the flame. By increasing the frame rate, the errors related to optical flow decreased. The two-camera method recreates the flame structure accurately, but is not able to resolve the small scale variations, which were a result of a smoothing effect caused by the transformation algorithm. KL and the associated uncertainties based on the flame luminosity influences are calculated. The uncertainty on KL for high sooting regions of the flame was approximately 100% higher when applying optical flow compared to the two-camera method, where the two-camera method yielded a bounded KL value up to 3.8, versus 2.7 for optical flow.

The beam steering effects due to nonuniformities in the light distribution from the

engineered diffuser were investigated. In order assess the effects of beam steering on the measurement, a model for calculating the intensity variation was developed and validated. The model uses measurement of the light distribution from the diffuser surface as input. The total radiation read by a pixel on the image sensor is calculated based on the light collected from an area on the diffuser, which is limited by the aperture of the objective lens, focal distance and the relative diffuser location. As beam steering is induced, the collection area on the diffuser is shifted according to the extent of beam steering. This follows a two-dimensional Gaussian probability density function (PDF), where the beam steering angle is defined as the angle determined from the standard deviation of the PDF and the diffuser/focal plane distance. By performing multiple calculations for varying beam steering angles and apertures, the intensity variation magnitude is found.

For the optimal aperture of f/1.2 and the expected level of beam steering in a CI spray, the intensity variation due to beam steering was 0.5% of the dynamic range, which can be reduced by improving the large scale nonuniformities in the diffuser light distribution. The model also emphasizes the importance of optimizing the optical setup with help from light characterization, where small and large scale nonuniformities in the diffuser light output are very important for reducing the intensity variation caused by beam steering, especially for high sooting flames.

5.2 Article II - Optical Measurements of In-Flame Soot in Compression-Ignited Methyl Ester Flames

The investigation of combustion and soot characteristics of surrogate fuels for biodiesel are presented in this study. The aim of the study is to produce highly accurate quantitative data of in-flame soot, which can be used for validation of models for spray flames or engine simulations. The study uses the DBIEI setup described in **Article I**, combined with simultaneous temporal OH^* chemiluminescence measurement for FLOL determination and light-based IDT. A literature review on the state-of-the-art of surrogate fuels representing biodiesel in kinetic studies is presented. The resulting selection of surrogate fuels was methyl oleate (MO), methyl decanoate (MD), *n*-heptane and a 50/50% molar blend of *n*-heptane and methyl decanoate (HP-MD), and comparing them to a rapeseed methyl ester (RME) fuel.

The measurement campaign was conducted in the OACIC, for four thermodynamic conditions, where the ambient gas temperature was varied while keeping the ambient gas density constant. A total of 30 combustion cycles were performed for each fuel. The analysis applied to the KL measurement includes the temporal development of total mass of soot during the premixed combustion phase and the spatial

gradient of soot mass (soot gradient) during the mixing-controlled quasi-steady period. The soot gradient indicates the average cross-axial development of soot along the central axis, providing a measure of soot mass production in the quasi-steady spray flame. Since all of these fuels, except *n*-heptane, are oxygenated, the equivalence ratio at FLOL ($\overline{\phi}(H)$) provides the amount of air mixed in prior to FLOL, where the fuel-bound oxygen is included. By comparing $\overline{\phi}(H)$ with the soot gradient, the sooting tendencies of the fuels based on the available oxygen are found.

IDTs were observed to follow the derived cetane number. During the premixed combustion phase, the IDT correlated well with the AHRR in this period, where a longer IDT resulted in a higher AHRR. The AHRR during the mixing-controlled period was similar for all fuels, which is due to the similar heating values of the fuels. The fuels can be divided into two groups; short and long carbon chain fuels. The long chain fuels, including RME and MO, had shorter IDTs compared to *n*-heptane, MD and HP-MD. When comparing the FLOLs to the IDTs, a correlation was found, where longer IDT generally resulted in a longer FLOL, which is consistent with existing literature.

For a constant $\overline{\phi}(H)$, the order of sooting tendency was RME>MO>HP>HP-MD>MD. RME was found to produce more soot than MO, which is likely due to the higher degree of unsaturation of RME. The very low sooting tendency of MD compared to *n*-heptane is likely due to the high fuel oxygen ratio, i.e. 6.6%, compared to 0%, where MD actually has more carbon-carbons bonds than *n*-heptane (9 versus 6, respectively), which promotes soot production, indicating that the higher fuel oxygen ratio of MD is causing the soot reduction between them.

The FLOL was found to vary during the mixing-controlled period, consequently affecting the in-flame soot production. In order to eliminate the transient effects, and to confirm the sooting trend presented above, which was based on mean values, the instantaneous FLOL and soot gradient were calculated for each injection. Generally, the transient soot gradient correlated well with the FLOL during a single injection, where a longer FLOL resulted in a lower soot gradient, and vice versa. This made it possible to observe the behavior of the soot gradient over a range of FLOLs combusting under the same thermodynamic condition. Comparing all fuels for the same ambient gas temperature yielded the same trend as mentioned above. This also showed that for $\overline{\phi}(H) < 2$, no fuel produced soot during the mixing-controlled period. From the instantaneous plots of $\overline{\phi}(H)$ and the soot gradient, a clear ambient gas temperature dependency was observed, where a higher temperature led to a higher soot gradient for the same equivalence ratio. This means that an increased temperature results in a higher increase of soot formation rate compared to soot oxidation rate. This was apparent for all fuels tested.

During the premixed combustion period, the maximum soot production rate was calculated, showing that higher ambient gas temperatures yielded higher maximum soot production rates. This was likely due to the shorter IDTs, resulting in richer premixed mixtures. The order of sooting tendencies based on the maximum soot production rate was similar to the trends found during the mixing-controlled period. However, these results were affected by the equivalence ratio in the mixture, which was not estimated in this study. Since the IDTs of RME and MO were comparable, similar equivalence ratio distributions can be expected during the premixed period. A 33% higher maximum soot production rate for RME therefore supports the previous finding that RME has a higher soot tendency than MO.

MO is found to be a good representative of RME, where the sooting tendency and combustion characteristics are closely recreated. However, MO is a large molecule, making it computationally expensive to be used in for instance CFD simulations. MD has an ester moiety, making the chemical pathways similar to RME. However, large difference in IDT, FLOL and sooting tendency were found. Blending MD with *n*-heptane makes it more suitable as a surrogate fuel, as it increases the sooting tendency and improves low temperature reactivity.

5.3 Article III - Combustion and Soot Characteristics of Hydrotreated Vegetable Oil Compression-Ignited Spray Flames

Combustion and in-flame soot characteristics of HVO were measured and compared to diesel fuel and RME. The optical techniques used are similar to those used in **Article I** and **Article II**. HVO has shown to be a promising future fuel, where low pollutant emissions compared to diesel fuel have been reported with regards to PM, NO_x and CO. This study is focused on reporting detailed information about in-flame soot production of HVO, and provide data for validation of future kinetic studies. The comparison of HVO with RME and diesel is made since a blend of these three fuels will likely be used in future CI engines.

HVO is a paraffinic fuel consisting of straight and branched alkanes of average carbon-chain length 15-18, giving the fuel a very high cetane number, typically 80-90. The fuel density of HVO is 8% lower than that of diesel fuel, and the kinematic viscosity is also lower, i.e. 2.92 mm^2/s versus 3.21 mm^2/s. Comparing the volatility of HVO to diesel fuel and RME, HVO is found to be the most volatile.

The measurements were conducted for four operating conditions where the ambient gas temperatures ranged from 819 K to 966 K with a constant ambient gas density of 16.7 kg/m^3. All other parameters connected to injection and operating

conditions were held constant.

The IDTs based on OH* chemiluminescence were consistent with the cetane number ratings of the fuels, ordered as HVO, RME and diesel, where HVO had the shortest IDT. The measured temporal development of the FLOL showed that diesel fuel needed more time to stabilize for the lowest ambient gas temperature condition, i.e. approximately 3 ms, while HVO and RME stabilized shortly after start of ignition. The FLOL of RME was found to be the shortest for all conditions, while HVO and diesel fuel had similar ones, which do not match the cetane number ratings. A possible explanation for this could be the cooling effect from the latent heat of evaporation, where RME was observed to have less evaporated fuel upstream of FLOL compared to HVO and diesel. This results in less evaporative cooling and could consequently make the FLOL of RME shorter.

The sooting characteristics of HVO were investigated by calculating the soot mass produced during the premixed and mixing-controlled phase. The soot inception time is defined as the time between ignition and when the soot mass production rate exceeded 30 μg/ms. The soot inception times were found to be in the order of diesel (0.23 ms), HVO (0.27 ms) and RME (0.35 ms), where a shorter time indicates an increased tendency to produce soot. The soot inception time was also observed to be insensitive to ambient gas temperature changes. A change in ambient gas temperature resulted in a change in IDT, which in turn changes the equivalence ratio in the premixed plume prior to ignition, where a shorter IDT yields a richer mixture. A richer mixture would be expected to form soot earlier, which was not observed. This could be explained by the fact that the air-fuel mixture is partially premixed, always having the equivalence ratio which results in the shortest possible soot inception time.

The soot production during the premixed phase was measured by total soot mass and the soot mass production rate 0.36 ms after ignition. This provided a comparison between the fuels at equal times after ignition. Based on this, diesel fuel was observed to have 3-6 times higher total soot mass and soot production rate compared to RME and HVO, while RME and HVO were found to produce similar levels of soot.

For the soot production during the mixing-controlled phase, the soot mass gradient (μg/cm) measured 20.2 mm downstream of FLOL during the quasi-steady period was used as metric. The soot production trend of the fuels was similar to that found during the premixed phase, where diesel fuel was the most sooting, while RME and HVO had similar levels.

The high soot production for diesel fuel is attributed to content of aromatics, which

is known to promote production of soot. Comparing the soot production in RME and HVO flames, they are comparable due to their similar average carbon chain lengths, i.e. 17 and 15-18, respectively. Since RME has an ester moiety, including two oxygen atoms per molecule (resulting in 3.61% fuel oxygen ratio), a slightly lower soot production is observed compared to HVO, which does not contain any oxygen.

5.4 Article IV - Detailed Examination of the Combustion of Diesel/Glycerol Emulsions in a Compression Ignition Engine

An increased production of biodiesel has been observed over the past decade as a result of allowing it to be blended with diesel fuel up to 7% by volume (EN 590). As a result, there is a large supply of the byproduct glycerol to the market, which exceeds the demand. The utilization of glycerol in diesel fuel as a soot reducing oxygenate additive is therefore studied in this work. Glycerol is characterized as having a low reactivity, high viscosity and being immiscible with diesel. Because of its immiscibility, the fuel is mixed in as an emulsion, requiring added surfactant and treatment.

In order to investigate a potential PM emission reduction after the addition of glycerol to diesel fuel, a reference diesel containing no biodiesel was compared to reference diesel containing 15% by mass glycerol. The experimental part consisted of measuring emissions and engine performance in a six cylinder CI engine. In addition, detailed in-flame soot and combustion characteristics were optically measured in the OACIC for three ambient gas temperatures. In order to fundamentally understand the soot reducing processes, a kinetic study was performed using a homogeneous constant pressure reactor simulation, where *n*-heptane containing 15% by mass glycerol was used as the surrogate fuel.

For the instrumented engine test, the two fuels were tested for six loads at a fixed engine speed, measuring the particle number and size distribution, and gas concentrations in the exhaust. There was found to be no significant difference in engine performance after adding glycerol to the fuel. Since the addition of glycerol to diesel prolongs the IDT, the injection timing was changed so as to maintain a 50% cumulative heat release at 1 CAD after TDC. For the exhaust gas emissions, the NO_x concentrations measured for the two fuels were similar, where the main differences were observed for CO, THC and PM. The addition of glycerol to diesel increased the CO and THC emissions, especially for lower loads. For higher loads, there were no differences observed. The increase in CO emissions is associated with incomplete combustion, which is attributed to the low reactivity of

glycerol. For the PM measurement, a reduction in particle number for particle diameters above 25 nm was observed. For particles smaller than 25 nm in diameter, large particle numbers were observed for the glycerol blend. These were hypothesized to partially or completely consist of condensed volatile organic compounds (VOCs) and not solid soot particles.

The optical results showed that the IDTs became longer after the addition of glycerol. The addition of glycerol also caused a longer FLOL, especially for the lowest ambient gas temperature condition. The soot mass gradient measured 19 mm downstream of the FLOL was slightly reduced after adding glycerol. The observed reduction in soot is likely due to the oxygen content in glycerol, which fits to the observation of a lower PM in the exhaust of the engine experiments.

The reactor simulation was performed at the thermodynamic conditions expected in the rich partially premixed region of the flame, i.e. close to FLOL. Ignition occurred at similar times for both fuels and attained the same flame temperatures at the last simulation time step. The concentrations of soot precursors such as ethene, ethyne (acetylene), propene and propyne at the last time step in the reactor were used as proxies for sooting tendency, where higher concentrations indicate a higher propensity to form soot particles. The addition of glycerol to *n*-heptane resulted in an increase of CO and a reduction of soot precursor concentration, which match the experimental results. The reduction of soot precursors occurs due to the presence of carbon-oxygen bonds in the glycerol molecule, which do not take part in soot chemistry. In addition, adding oxygen atoms increases the oxidation of the species pool including soot precursors.

6. Conclusion and Further Work

6.1 Conclusion

During the current doctoral work, the most important contribution has been the development of an experimental test rig for conducting measurements of combustion and emission characteristics in CI engines. The experimental rig allows for detailed optical measurements of CI combustion, enabling the ability to perform state-of-the-art research on high pressure spray flames. Operational procedures and technical descriptions of the rig have been described, allowing for further research on alternative fuels used in CI engines. The test rig is adapted to perform fuel studies, where experiments can be executed in relatively short time, enabling the generation of large sample sizes for statistically significant results. In addition, since the test rig is versatile, other engine combustion modes such as spark ignition, homogeneous charge compression ignition and reaction controlled compression ignition combustion can be studied.

The presented work also includes improvements to the measuring technique DBIEI of soot, where a method for reducing the influence of flame luminosity on the measured optical density in turbulent spray flames has been developed, improving the measurement of high sooting flames in particular. The optical setup needed for conducting in-flame soot measurements with high reliability has been described, where effects like beam steering and non-ideal camera characteristics have been assessed in detail.

Research on combustion and sooting characteristics of biofuels has been conducted. Firstly, an experimental comparison of a biodiesel against potential surrogate fuels was performed. The work resulted in detailed information on in-flame soot production of biodiesel surrogate fuels, which can be used in future numerical simulations. The inclusion of a real biodiesel also enables an experimental comparison between a real fuel and its corresponding surrogate fuels, allowing

to assess the degree of replication when replacing a real biodiesel with simplified surrogates. Methyl oleate was found to be a good surrogate fuel for RME, yielding similar combustion characteristics and sooting tendency. Methyl decanoate had poor low temperature combustion properties and a low sooting tendency compared to RME. However, methyl oleate requires a complex reaction mechanism because of its large size, making it unfit for comprehensive numerical simulations. Methyl decanoate based surrogates have similar combustion chemistry to that of RME because of their ester moiety, and are less computationally expensive than methyl oleate. Secondly, since HVO is a promising future energy resource for CI engines, a detailed investigation of combustion and in-flame soot production of HVO spray flames was performed. A comparison between HVO, RME and diesel fuel was conducted in order to elucidate the phenomena contributing to the reduction in PM emissions observed in engine tests fueled with HVO, while generating detailed information on in-flame soot. Diesel fuel was found to produce the most in-flame soot due to its aromatic content, while HVO and RME produced similar levels of in-flame soot. RME showed a slightly lower soot production than HVO, which is likely attributed to its fuel-bound oxygen content, since the number of carbon-carbon bonds are similar. Lastly, a study on the effect of adding glycerol to diesel fuel as an emulsion was conducted. The addition of glycerol reduces PM emissions in engine tests, which was can be explained by a lower in-flame soot production due to the fuel-bound oxygen in glycerol. This was supported by optical measurements and numerical simulations. However, disadvantages of adding glycerol was also realized since it has a low reactivity, high viscosity and is immiscible with diesel fuel.

6.2 Further work

Further work is needed in order to reduce PM emissions from CI engines. Research on biofuels is important since it will likely be part of the solution for reducing CO_2 emissions to the atmosphere.

The OACIC offers a great opportunity to further extend existing knowledge on potential biofuels for future CI engines. New types of biofuels such as upgraded pyrolysis oil and hydrothermal liquefaction fuels should be studied in detail in order to map their combustion and emission characteristics. Although these fuels are still limited in quantity, since the production processes still are at a research stage, the potential variation in molecular composition can be mapped, where surrogate fuels can be designed and tested in a research device such as the OACIC. By collaborating with researchers developing the production processes, the fuel can be altered according to the results achieved from combustion experiments, potentially simplifying the production process. The fuel properties of the novel biofuel might

not comply to existing standards on its own, but could achieve this from blending it with a conventional fuel such as biodiesel or diesel fuel. This could potentially make the upgrading process less complex and consequently more economically viable. A systematic screening study where the fuel properties of blends of possible novel biofuels and conventional fuels should be conducted. By selecting blends that comply to existing standards and designing surrogate fuels that fit the novel biofuel's properties, measurements of the surrogate fuel blend can be conducted in the OACIC and in a real engine, providing confidence that the novel biofuel can be implemented to existing vehicles.

Soot can be investigated more in detail. Linking optical in-flame soot measurements with PM is interesting, since it provides information about soot oxidation processes occurring in the exhaust stream. This can be achieved in the OACIC by measuring particle numbers and size distributions of PM in the exhaust. The soot oxidation occurring in the exhaust is dependent on the oxidative properties of the particles, which can vary based on the fuel and combustion process. The OACIC offers the possibility to sample soot particles in the flame and exhaust, and thereby analyzing the nanosized soot structure in a transmission electron microscope. Sampling soot in the exhaust stream has already been tested, however, techniques for sampling in-flame soot particles require further development. In addition, procedures for measuring PM in the exhaust need to be further developed, where problems related to skip-firing and contamination must be solved.

A CFD model of the motored cycle in the OACIC should be developed in order to perform simulations of the flow field and heat transfer in the combustion chamber. A working CFD model of the internal flow can also be used to design new throat designs, where a flow field with little gas motion or high swirl can be achieved. In addition, this also provides input to the thermodynamic model of the OACIC, which can improve estimation of the compressed air temperature and density.

If further research on CI spray combustion is pursued, involvement in the Engine Combustion Network (ECN) should be strived for. In order to contribute to the ECN research, the standard nozzles must fit the OACIC, where for instance spray A has an axially drilled nozzle hole, requiring a different installation of the injector onto the OACIC. A possible solution could be to fit the injector from the top of the engine head, enabling a centered spray, injecting vertically into the combustion chamber. This would require a modified design of the engine head.

For investigating biofuels and soot production more in detail, a combination of experiments and kinetic simulations should be performed. A preliminary kinetic study on the fuels tested in **Article II**, using the detailed hydrocarbon mechanism of CRECK [147] was performed. The approach was similar to the kinetic study

performed in **Article IV**. A correlation between the experimental results and the numerical simulation results was achieved, and further work on developing this model is encouraged, providing insight to the chemical mechanisms behind soot production for complex fuels. These simulations are not computationally costly, which enable the use of detailed mechanisms, where pathways for soot formation and oxidation can be identified for both the real fuel and the surrogate fuel. This methodology could result in a tool for constructing surrogate fuels, where the change of kinetic pathways to soot formation after simplification of the fuel composition can be identified.

Bibliography

[1] H. Aatola, M. Larmi, T. Sarjovaara, and S. Mikkonen. Hydrotreated Vegetable Oil (HVO) as a Renewable Diesel Fuel: Trade-off between NOx, Particulate Emission, and Fuel Consumption of a Heavy Duty Engine. *SAE International Journal of Engines*, 1(1):1251–1262, Oct. 2008.

[2] E. Çabukoglu, G. Georges, L. Küng, G. Pareschi, and K. Boulouchos. Battery electric propulsion: An option for heavy-duty vehicles? Results from a Swiss case-study. *Transportation Research Part C: Emerging Technologies*, 88:107–123, Mar. 2018.

[3] J. Akhtar and N. A. S. Amin. A review on process conditions for optimum bio-oil yield in hydrothermal liquefaction of biomass. *Renewable and Sustainable Energy Reviews*, 15(3): 1615–1624, Apr. 2011.

[4] T. L. Alleman and R. L. McCormick. Fischer-Tropsch Diesel Fuels – Properties and Exhaust Emissions: A Literature Review. In *SAE Technical Paper Series*, 2003. doi: 10.4271/2003-01-0763.

[5] A. Arneth, H. Barbosa, T. Benton, and Coauthors. Climate Change and Land. Special Report on climate change, desertification, and degradation, sustainable land management, food security, and greenhouse gas fluxes in terrestrial ecosystems. Technical report, IPCC, 2019. URL https://www.ipcc.ch/srccl/.

[6] R. S. G. Baert, P. J. M. Frijters, B. Somers, C. C. M. Luijten, and W. de Boer. Design and Operation of a High Pressure, High Temperature Cell for HD Diesel Spray Diagnostics: Guidelines and Results. In *SAE Technical Paper Series*, Apr. 2009. doi: 10.4271/2009-01-0649.

[7] S. Bai, J. Tang, G. Wang, and G. Li. Soot loading estimation model and passive regeneration characteristics of DPF system for heavy-duty engine. *Applied Thermal Engineering*, 100: 1292–1298, May 2016.

[8] M. Bardi, R. Payri, L. M. Malbec, G. Bruneaux, L. M. Pickett, J. Manin, T. Bazyn, and C. Genzale. Engine combustion network: Comparison of spray development, vaporization, and combustion in different combustion vessels. *Atomization and Sprays*, 22(10):807–842, 2012.

[9] C. C. Barrios, C. Martín, A. Domínguez-Sáez, P. Álvarez, M. Pujadas, and J. Casanova. Effects of the addition of oxygenated fuels as additives on combustion characteristics and particle number and size distribution emissions of a TDI diesel engine. *Fuel*, 132:93–100, Sept. 2014.

[10] P. Basu. *Biomass gasification, pyrolysis and torrefaction: practical design and theory*. Academic press, 3rd edition, 2018. ISBN 978-0-12-812992-0.

[11] P. Benjumea, J. R. Agudelo, and A. F. Agudelo. Effect of the Degree of Unsaturation of Biodiesel Fuels on Engine Performance, Combustion Characteristics, and Emissions. *Energy & Fuels*, 25(1):77–85, Jan. 2011.

[12] J. M. Bergthorson and M. J. Thomson. A review of the combustion and emissions properties of advanced transportation biofuels and their impact on existing and future engines. *Renewable and Sustainable Energy Reviews*, 42:1393–1417, Feb. 2015.

[13] V. Bermúdez, J. M. García, E. Juliá, and S. Martínez. Engine with Optically Accessible Cylinder Head: A Research Tool for Injection and Combustion Processes. In *SAE Technical Paper Series*, Mar. 2003. doi: 10.4271/2003-01-1110.

[14] C. F. Bohren and D. R. Huffman. *Absorption and scattering of light by small particles*. John Wiley & Sons, 2008. ISBN 978-3-527-61816-3.

[15] T. C. Bond, S. J. Doherty, D. W. Fahey, P. M. Forster, T. Berntsen, B. J. DeAngelo, M. G. Flanner, S. Ghan, B. Kärcher, D. Koch, S. Kinne, Y. Kondo, P. K. Quinn, M. C. Sarofim, M. G. Schultz, M. Schulz, C. Venkataraman, H. Zhang, S. Zhang, N. Bellouin, S. K. Guttikunda, P. K. Hopke, M. Z. Jacobson, J. W. Kaiser, Z. Klimont, U. Lohmann, J. P. Schwarz, D. Shindell, T. Storelvmo, S. G. Warren, and C. S. Zender. Bounding the role of black carbon in the climate system: A scientific assessment. *Journal of Geophysical Research: Atmospheres*, 118(11):5380–5552, June 2013.

[16] F. V. Bracco. Modeling of Engine Sprays. In *SAE Technical Paper Series*. SAE International, Feb. 1985. doi: 10.4271/850394.

[17] H. F. Calcote. Mechanisms of soot nucleation in flames—A critical review. *Combustion and Flame*, 42:215–242, Jan. 1981.

[18] J. C. Caroca, F. Millo, D. Vezza, T. Vlachos, A. De Filippo, S. Bensaid, N. Russo, and D. Fino. Detailed Investigation on Soot Particle Size Distribution during DPF Regeneration, using Standard and Bio-Diesel Fuels. *Industrial & Engineering Chemistry Research*, 50(5): 2650–2658, Mar. 2011.

[19] W.-T. Chen, Y. Zhang, T. H. Lee, Z. Wu, B. Si, C.-F. F. Lee, A. Lin, and B. K. Sharma. Renewable diesel blendstocks produced by hydrothermal liquefaction of wet biowaste. *Nature Sustainability*, 1(11):702–710, Nov. 2018.

[20] Chevron Corporation. Diesel Fuels Technical Review. Technical report, Chevron Corporation, 2007. URL https://www.chevron.com/-/media/chevron/operations/documents/diesel-fuel-tech-review.pdf.

[21] D. Chiaramonti, M. Prussi, M. Buffi, A. M. Rizzo, and L. Pari. Review and experimental study on pyrolysis and hydrothermal liquefaction of microalgae for biofuel production. *Applied Energy*, 185:963–972, Jan. 2017.

[22] H. J. Curran, P. Gaffuri, W. J. Pitz, and C. K. Westbrook. A Comprehensive Modeling Study of n-Heptane Oxidation. *Combustion and Flame*, 114(1):149–177, July 1998.

[23] D. D. Das, C. S. McEnally, and L. D. Pfefferle. Sooting Tendencies of Unsaturated Esters in Nonpremixed Flames. *Combustion and Flame*, 162(4):1489–1497, Apr. 2015.

[24] C. J. Dasch. One-dimensional tomography: a comparison of Abel, onion-peeling, and filtered backprojection methods. *Applied Optics*, 31(8):1146–1152, Mar. 1992.

[25] J. E. Dec. A Conceptual Model of DI Diesel Combustion Based on Laser-Sheet Imaging. In *SAE Technical Paper Series*. SAE International, Feb. 1997. doi: 10.4271/970873.

[26] J. E. Dec. Advanced compression-ignition engines—understanding the in-cylinder processes. *Proceedings of the Combustion Institute*, 32(2):2727–2742, 2009.

[27] J. E. Dec, A. O. zur Loye, and D. L. Siebers. Soot Distribution in a D.I. Diesel Engine Using 2-D Laser-Induced Incandescence Imaging. In *SAE Technical Paper Series*, Feb. 1991. doi: 10.4271/910224.

[28] R. Diesel. The Diesel Oil-Engine, and Its Industrial Importance, Particularly for Great Britain. *Proceedings of the Institution of Mechanical Engineers*, 82(1):179–280, June 1912.

[29] A. Dimitriadis and S. Bezergianni. Hydrothermal liquefaction of various biomass and waste feedstocks for biocrude production: A state of the art review. *Renewable and Sustainable Energy Reviews*, 68:113–125, Feb. 2017.

[30] O. Doğan. The influence of n-butanol/diesel fuel blends utilization on a small diesel engine performance and emissions. *Fuel*, 90(7):2467–2472, July 2011.

[31] A. Donkerbroek, M. Boot, C. Luijten, N. Dam, and J. ter Meulen. Flame lift-off length and soot production of oxygenated fuels in relation with ignition delay in a DI heavy-duty diesel engine. *Combustion and Flame*, 158(3):525–538, Mar. 2011.

[32] D. X. Du, R. L. Axelbaum, and C. K. Law. The influence of carbon dioxide and oxygen as additives on soot formation in diffusion flames. *Symposium (International) on Combustion*, 23(1):1501–1507, Jan. 1991.

[33] A. Engman, T. Hartikka, M. Honkanen, and U. Kiiski. Neste Renewable Diesel Handbook. Technical report, Neste Oyj, 2016. URL https://www.neste.com/.

[34] European Environment Agency. Air pollutant emissions data viewer (Gothenburg Protocol, LRTAP Convention) 1990-2017, July 2019. URL https://www.eea.europa.eu/data-and-maps/dashboards/air-pollutant-emissions-data-viewer-2.

[35] European Union. Regulation (EC) No 715/2007 of the European Parliament and of the Council of 20 June 2007 on type approval of motor vehicles with respect to emissions from light passenger and commercial vehicles (Euro 5 and Euro 6) and on access to vehicle repair and maintenance information, June 2007. URL http://data.europa.eu/eli/reg/2007/715/oj.

[36] M. A. Fahim, T. A. Alsahhaf, and A. S. Elkilani. *Fundamentals of petroleum refining*. Elsevier, Amsterdam, 2010. ISBN 978-0-444-52785-1.

[37] M. Frenklach and H. Wang. Detailed mechanism and modeling of soot particle formation. In *Soot formation in combustion*, pages 165–192. Springer, Berlin, Heidelberg, 1994. ISBN 978-3-642-85169-8.

[38] A. G. Gaydon. *The Spectroscopy of Flames*. Springer Verlag, Dordrecht, 2nd edition, 1974. ISBN 978-94-009-5722-0.

[39] J. B. Ghandhi and D. M. Heim. An optimized optical system for backlit imaging. *Review of Scientific Instruments*, 80(5):056105, May 2009.

[40] S. S. Gill, A. Tsolakis, K. D. Dearn, and J. Rodríguez-Fernández. Combustion characteristics and emissions of Fischer–Tropsch diesel fuels in IC engines. *Progress in Energy and Combustion Science*, 37(4):503–523, Aug. 2011.

[41] I. Glassman. Soot formation in combustion processes. *Symposium (International) on Combustion*, 22(1):295–311, Jan. 1989.

[42] I. Glassman, R. A. Yetter, and N. G. Glumac. *Combustion*. Academic press, 5th edition, 2014. ISBN 978-0-12-407913-7.

[43] E. Gnansounou, A. Dauriat, J. Villegas, and L. Panichelli. Life cycle assessment of biofuels: Energy and greenhouse gas balances. *Bioresource Technology*, 100(21):4919–4930, Nov. 2009.

[44] A. R. K. Gollakota, N. Kishore, and S. Gu. A review on hydrothermal liquefaction of biomass. *Renewable and Sustainable Energy Reviews*, 81:1378–1392, Jan. 2018.

[45] M. A. González, W. Piel, T. Asmus, W. Clark, J. Garbak, E. Liney, M. Natarajan, D. W. Naegeli, D. Yost, E. A. Frame, and J. P. Wallace. Oxygenates screening for AdvancedPetroleum-Based Diesel Fuels: Part 2. The Effect of Oxygenate Blending Compounds on Exhaust Emissions. In *SAE Technical Paper Series*, Sept. 2001. doi: 10.4271/2001-01-3632.

[46] P. S. Greenberg and J. C. Ku. Soot volume fraction imaging. *Applied Optics*, 36(22):5514, Aug. 1997.

[47] B. Guan, R. Zhan, H. Lin, and Z. Huang. Review of the state-of-the-art of exhaust particulate filter technology in internal combustion engines. *Journal of Environmental Management*, 154:225–258, May 2015.

[48] A. J. Haagen-Smit. Chemistry and Physiology of Los Angeles Smog. *Industrial & Engineering Chemistry*, 44(6):1342–1346, June 1952.

[49] H. Halleux, S. Lassaux, R. Renzoni, and A. Germain. Comparative life cycle assessment of two biofuels ethanol from sugar beet and rapeseed methyl ester: With a preface by Jörg Schweinle. *The International Journal of Life Cycle Assessment*, 13(3):184–190, May 2008.

[50] B. S. Haynes and H. G. Wagner. Soot formation. *Progress in Energy and Combustion Science*, 7(4):229–273, Jan. 1981.

[51] J. B. Heywood. *Internal Combustion Engine Fundamentals*. McGraw-Hill, 1988. ISBN 0-07-100499-8.

[52] B. Higgins and D. Siebers. Measurement of the Flame Lift-Off Location on Dl Diesel Sprays Using OH Chemiluminescence. In *SAE Technical Paper Series*, 2001. doi: 10.4271/2001-01-0918.

[53] B. Higgins, D. L. Siebers, and A. Aradi. Diesel-Spray Ignition and Premixed-Burn Behavior. In *SAE Technical Paper Series*, Mar. 2000. doi: 10.4271/2000-01-0940.

[54] S. K. Hoekman and C. Robbins. Review of the effects of biodiesel on NOx emissions. *Fuel Processing Technology*, 96:237–249, Apr. 2012.

[55] F. M. Hossain, M. N. Nabi, T. J. Rainey, T. Bodisco, M. M. Rahman, K. Suara, S. M. A. Rahman, T. C. Van, Z. Ristovski, and R. J. Brown. Investigation of microalgae HTL fuel effects on diesel engine performance and exhaust emissions using surrogate fuels. *Energy Conversion and Management*, 152:186–200, Nov. 2017.

[56] H. C. Hottel and F. P. Broughton. Determination of True Temperature and Total Radiation from Luminous Gas Flames. *Industrial & Engineering Chemistry Analytical Edition*, 4(2): 166–175, Apr. 1932.

[57] M. Härtl, P. Seidenspinner, E. Jacob, and G. Wachtmeister. Oxygenate screening on a heavy-duty diesel engine and emission characteristics of highly oxygenated oxymethylene ether fuel OME1. *Fuel*, 153:328–335, Aug. 2015.

[58] G. W. Huber, P. O'Connor, and A. Corma. Processing biomass in conventional oil refineries: Production of high quality diesel by hydrotreating vegetable oils in heavy vacuum oil mixtures. *Applied Catalysis A: General*, 329:120–129, Oct. 2007.

[59] C. A. Idicheria and L. M. Pickett. Effect of EGR on diesel premixed-burn equivalence ratio. *Proceedings of the Combustion Institute*, 31(2):2931–2938, Jan. 2007.

[60] B. Ihracska, R. J. Crookes, D. Montalvão, M. R. Herfatmanesh, Z. Peng, S. Imran, and T. Korakianitis. Opto-mechanical design for sight windows under high loads. *Materials & Design*, 117:430–444, Mar. 2017.

[61] F. Inal and S. M. Senkan. Effects of oxygenate concentration on species mole fractions in premixed n-heptane flames. *Fuel*, 84(5):495–503, Mar. 2005.

[62] International Energy Agency. Renewables 2018. Technical report, 2018. URL https://www.iea.org/renewables2018/.

[63] International Energy Agency. *Global EV Outlook 2019: Scaling-up the transition to electric mobility*. OECD, June 2019. ISBN 978-92-64-47013-2.

[64] International Energy Agency. Transport, May 2019. URL https://www.iea.org/tcep/transport/.

[65] U. Irfan. The law that's helping fuel Delhi's deadly air pollution. *Vox Media*, Nov. 2019.

[66] K. O. Johansson, M. P. Head-Gordon, P. E. Schrader, K. R. Wilson, and H. A. Michelsen. Resonance-stabilized hydrocarbon-radical chain reactions may explain soot inception and growth. *Science*, 361(6406):997–1000, Sept. 2018.

[67] T. N. Kalnes, K. P. Koers, T. Marker, and D. R. Shonnard. A technoeconomic and environmental life cycle comparison of green diesel to biodiesel and syndiesel. *Environmental Progress & Sustainable Energy*, 28(1):111–120, 2009.

[68] T. Kamimoto and S. Matsuoka. Prediction of spray evaporation in reciprocating engines. In *SAE Transactions*, volume 86, pages 1792–1802, 1977.

[69] T. Kan, V. Strezov, and T. J. Evans. Lignocellulosic biomass pyrolysis: A review of product properties and effects of pyrolysis parameters. *Renewable and Sustainable Energy Reviews*, 57:1126–1140, May 2016.

[70] D. Kennaird, C. Crua, M. Heikal, R. Morgan, F. Bar, and S. Sapsford. A new high-pressure diesel spray research facility. In *IMechE international conference on computational and experimental methods in reciprocating engines*, volume 8, pages 179–188, UK, 2000.

[71] M. R. Kholghy, J. Weingarten, A. D. Sediako, J. Barba, M. Lapuerta, and M. J. Thomson. Structural Effects of Biodiesel on Soot Formation in a Laminar Coflow Diffusion Flame. *Proceedings of the Combustion Institute*, 36(1):1321–1328, 2017.

[72] T. Kitamura, T. Ito, J. Senda, and H. Fujimoto. Extraction of the suppression effects of oxygenated fuels on soot formation using a detailed chemical kinetic model. *JSAE Review*, 22(2):139–145, Apr. 2001.

[73] G. Knothe. Historical perspectives on vegetable oil-based fuels. *INFORM - International News on Fats, Oils and Related Materials*, 12(11):1103, 2001.

[74] G. Knothe. Dependence of Biodiesel Fuel Properties on the Structure of Fatty Acid Alkyl Esters. *Fuel Processing Technology*, 86(10):1059–1070, June 2005.

[75] G. Knothe. "Designer" Biodiesel: Optimizing Fatty Ester Composition to Improve Fuel Properties. *Energy & Fuels*, 22(2):1358–1364, Mar. 2008.

[76] G. Knothe and L. F. Razon. Biodiesel fuels. *Progress in Energy and Combustion Science*, 58:36–59, Jan. 2017.

[77] G. Knothe, C. A. Sharp, and T. W. Ryan. Exhaust Emissions of Biodiesel, Petrodiesel, Neat Methyl Esters, and Alkanes in a New Technology Engine. *Energy & Fuels*, 20(1):403–408, Jan. 2006.

[78] M. Koebel, M. Elsener, and M. Kleemann. Urea-SCR: a promising technique to reduce NOx emissions from automotive diesel engines. *Catalysis Today*, 59(3):335–345, June 2000.

[79] S. Kook and L. M. Pickett. Effect of Fuel Volatility and Ignition Quality on Combustion and Soot Formation at Fixed Premixing Conditions. *SAE International Journal of Engines*, 2(2): 11–23, Nov. 2009.

[80] H. Kosaka, T. Aizawa, and T. Kamimoto. Two-dimensional imaging of ignition and soot formation processes in a diesel flame. *International Journal of Engine Research*, 6(1):21–42, Feb. 2005.

[81] V. Krivopolianskii. *Experimental Investigation of Injection and Combustion Processes in Marine Gas Engines Using Constant Volume Rig*. PhD thesis, Norwegian University of Science and Technology, Trondheim, Norway, 2019.

[82] V. Krivopolianskii, K. O. P. Bjørgen, D. Emberson, S. Ushakov, V. Æsøy, and T. Løvås. Experimental Study of Ignition Delay, Combustion, and NO Emission Characteristics of Hydrogenated Vegetable Oil. *SAE International Journal of Fuels and Lubricants*, 12(1):29–42, Feb. 2019.

[83] K. K. Kuo and R. Acharya. *Fundamentals of Turbulent and Multiphase Combustion*. John Wiley & Sons, Inc., Hoboken, NJ, USA, Mar. 2012. ISBN 978-1-118-10768-3.

[84] N. Ladommatos, M. Parsi, and A. Knowles. The effect of fuel cetane improver on diesel pollutant emissions. *Fuel*, 75(1):8–14, Jan. 1996.

[85] M. Lapuerta, O. Armas, and J. Rodriguez-Fernandez. Effect of biodiesel fuels on diesel engine emissions. *Progress in Energy and Combustion Science*, 34(2):198–223, Apr. 2008.

[86] M. Lapuerta, M. Villajos, J. R. Agudelo, and A. L. Boehman. Key properties and blending strategies of hydrotreated vegetable oil as biofuel for diesel engines. *Fuel Processing Technology*, 92(12):2406–2411, Dec. 2011.

[87] M. K. Le, R. Zhang, L. Rao, S. Kook, and E. R. Hawkes. The Development of Hydroxyl and Soot in a Methyl Decanoate-Fuelled Automotive-Size Optical Diesel Engine. *Fuel*, 166: 320–332, Feb. 2016.

[88] D. Leckel. Diesel Production from Fischer-Tropsch: The Past, the Present, and New Concepts. *Energy & Fuels*, 23(5):2342–2358, May 2009.

[89] S. Lee, T. Kim, and K. Kang. Performance and emission characteristics of a diesel engine operated with wood pyrolysis oil. *Proceedings of the Institution of Mechanical Engineers, Part D: Journal of Automobile Engineering*, 228(2):180–189, Feb. 2014.

[90] R. Lemaire, A. Faccinetto, E. Therssen, M. Ziskind, C. Focsa, and P. Desgroux. Experimental comparison of soot formation in turbulent flames of Diesel and surrogate Diesel fuels. *Proceedings of the Combustion Institute*, 32(1):737–744, 2009.

[91] T. Li. *Gasification of Biomass for Second Generation Biofuel Production*. PhD thesis, Norwegian University of Science and Technology, Trondheim, Norway, 2015.

[92] P. M. Lillo, L. M. Pickett, H. Persson, O. Andersson, and S. Kook. Diesel Spray Ignition Detection and Spatial/Temporal Correction. *SAE International Journal of Engines*, 5(3): 1330–1346, Apr. 2012.

[93] LOGE AB. LOGEresearch Manual - Engine Models, 2017. URL https://logesoft.com/.

[94] A. Maiboom, X. Tauzia, and J.-F. Hétet. Experimental study of various effects of exhaust gas recirculation (EGR) on combustion and emissions of an automotive direct injection diesel engine. *Energy*, 33(1):22–34, Jan. 2008.

[95] J. Manin, M. Bardi, and L. M. Pickett. Evaluation of the liquid length via diffused back-illumination imaging in vaporizing diesel sprays. In *The Proceedings of the International symposium on diagnostics and modeling of combustion in internal combustion engines 2012.8*, pages 665–673. The Japan Society of Mechanical Engineers, 2012.

[96] J. Manin, L. M. Pickett, and S. A. Skeen. Two-Color Diffused Back-Illumination Imaging as a Diagnostic for Time-Resolved Soot Measurements in Reacting Sprays. *SAE International Journal of Engines*, 6(4):1908–1921, Oct. 2013.

[97] J. Manin, S. Skeen, L. Pickett, E. Kurtz, and J. E. Anderson. Effects of Oxygenated Fuels on Combustion and Soot Formation/Oxidation Processes. *SAE International Journal of Fuels and Lubricants*, 7(3):704–717, Oct. 2014.

[98] B. Mohan, W. Yang, and S. k. Chou. Fuel injection strategies for performance improvement and emissions reduction in compression ignition engines—A review. *Renewable and Sustainable Energy Reviews*, 28:664–676, Dec. 2013.

[99] C. J. Mueller and G. C. Martin. Effects of Oxygenated Compounds on Combustion and Soot Evolution in a DI Diesel Engine: Broadband Natural Luminosity Imaging. In *SAE Technical Paper Series*, 2002. doi: 10.4271/2002-01-1631.

[100] C. J. Mueller, W. J. Pitz, L. M. Pickett, G. C. Martin, D. L. Siebers, and C. K. Westbrook. Effects of Oxygenates on Soot Processes in DI Diesel Engines: Experiments and Numerical Simulations. In *SAE Technical Paper Series*, May 2003. doi: 10.4271/2003-01-1791.

[101] M. Musculus and L. Pickett. Diagnostic Considerations for Optical Laser-Extinction Measurements of Soot in High-Pressure Transient Combustion Environments. *Combustion and Flame*, 141(4):371–391, June 2005.

[102] M. P. Musculus, J. E. Dec, and D. R. Tree. Effects of Fuel Parameters and Diffusion Flame Lift-Off on Soot Formation in a Heavy-Duty DI Diesel Engine. In *SAE Technical Paper Series*, Mar. 2002. doi: 10.4271/2002-01-0889.

[103] M. P. Musculus, P. C. Miles, and L. M. Pickett. Conceptual Models for Partially Premixed Low-Temperature Diesel Combustion. *Progress in Energy and Combustion Science*, 39(2-3): 246–283, Apr. 2013.

[104] J. Naber and D. L. Siebers. Effects of Gas Density and Vaporization on Penetration and Dispersion of Diesel Sprays. In *SAE Technical Paper Series*, 1996. doi: 10.4271/960034.

[105] M. N. Nabi, M. M. Rahman, M. A. Islam, F. M. Hossain, P. Brooks, W. N. Rowlands, J. Tulloch, Z. D. Ristovski, and R. J. Brown. Fuel characterisation, engine performance, combustion and exhaust emissions with a new renewable Licella biofuel. *Energy Conversion and Management*, 96:588–598, May 2015.

[106] J. T. Nakos. Uncertainty analysis of thermocouple measurements used in normal and abnormal thermal environment experiments at Sandia's Radiant Heat Facility and Lurance Canyon Burn Site. Technical Report SAND2004-1023, 918777, Sandia National Laboratories, Apr. 2004. URL http://www.osti.gov/servlets/purl/918777-6up8yW/.

[107] M. Natarajan, E. A. Frame, D. W. Naegeli, T. Asmus, W. Clark, J. Garbak, A. Manuel, D. González, E. Liney, W. Piel, and J. P. Wallace. Oxygenates for Advanced Petroleum-Based Diesel Fuels: Part 1. Screening and Selection Methodology for the Oxygenates. In *SAE Technical Paper Series*, 2001. doi: 10.4271/2001-01-3631.

[108] Y. İçıngür and D. Altiparmak. Effect of fuel cetane number and injection pressure on a DI Diesel engine performance and emissions. *Energy Conversion and Management*, 44(3):389–397, Feb. 2003.

[109] G. Nichols, S. Byard, M. J. Bloxham, J. Botterill, N. J. Dawson, A. Dennis, V. Diart, N. C. North, and J. D. Sherwood. A review of the terms agglomerate and aggregate with a recommendation for nomenclature used in powder and particle characterization. *Journal of Pharmaceutical Sciences*, 91(10):2103–2109, 2002.

[110] O. Nilaphai, C. Hespel, S. Chanchaona, and C. Mounaïm-Rousselle. Spray and combustion characterizations of ABE/Dodecane blend in comparison to alcohol/Dodecane blends at high-pressure and high-temperature conditions. *Fuel*, 225:542–553, Aug. 2018.

[111] I. Nyström, P. Bokinge, and P.-k. Franck. Production of liquid advanced biofuels - global status. Technical report, CIT Industriell Energi AB, 2019.

[112] J. Otera. Transesterification. *Chemical Reviews*, 93(4):1449–1470, June 1993.

[113] S. S. Pandurangi, M. Bolla, Y. M. Wright, K. Boulouchos, S. A. Skeen, J. Manin, and L. M. Pickett. Onset and Progression of Soot in High-Pressure N-Dodecane Sprays Under Diesel Engine Conditions. *International Journal of Engine Research*, 18(5-6):436–452, Aug. 2017.

[114] J. Pastor, J. García-Oliver, J.-G. Nerva, and B. Giménez. Fuel effect on the liquid-phase penetration of an evaporating spray under transient diesel-like conditions. *Fuel*, 90(11):3369–3381, Nov. 2011.

[115] J. V. Pastor, J. M. Garcia-Oliver, R. Novella, and T. Xuan. Soot Quantification of Single-Hole Diesel Sprays by Means of Extinction Imaging. *SAE International Journal of Engines*, 8(5): 2068–2077, Sept. 2015.

[116] F. Payri, J. V. Pastor, J. M. García, and J. M. Pastor. Contribution to the application of two-colour imaging to diesel combustion. *Measurement Science and Technology*, 18(8):2579–2598, Aug. 2007.

[117] R. Payri, J. Gimeno, M. Bardi, and A. H. Plazas. Study liquid length penetration results obtained with a direct acting piezo electric injector. *Applied Energy*, 106:152–162, June 2013.

[118] N. Peters. *Turbulent Combustion*. Cambridge University Press, Cambridge, 2000. ISBN 978-0-511-61270-1.

[119] L. M. Pickett and D. L. Siebers. An investigation of diesel soot formation processes using micro-orifices. *Proceedings of the Combustion Institute*, 29(1):655–662, Jan. 2002.

[120] L. M. Pickett and D. L. Siebers. Non-Sooting, Low Flame Temperature Mixing-Controlled DI Diesel Combustion. In *SAE Technical Paper Series*, 2004. doi: 10.4271/2004-01-1399.

[121] L. M. Pickett and D. L. Siebers. Soot Formation in Diesel Fuel Jets Near the Lift-Off Length. *International Journal of Engine Research*, 7(2):103–130, Apr. 2006.

[122] L. M. Pickett, D. L. Siebers, and C. A. Idicheria. Relationship Between Ignition Processes and the Lift-Off Length of Diesel Fuel Jets. In *SAE Technical Paper Series*, Oct. 2005. doi: 10.4271/2005-01-3843.

[123] L. M. Pickett, S. Kook, and T. C. Williams. Visualization of Diesel Spray Penetration, Cool-Flame, Ignition, High-Temperature Combustion, and Soot Formation Using High-Speed Imaging. *SAE International Journal of Engines*, 2(1):439–459, Apr. 2009.

[124] L. M. Pickett, C. L. Genzale, G. Bruneaux, L.-M. Malbec, L. Hermant, C. Christiansen, and J. Schramm. Comparison of Diesel Spray Combustion in Different High-Temperature, High-Pressure Facilities. *SAE International Journal of Engines*, 3(2):156–181, Oct. 2010.

[125] L. M. Pickett, C. L. Genzale, J. Manin, C.-M. Térmicos, L.-M. Malbec, and L. Hermant. Measurement Uncertainty of Liquid Penetration in Evaporating Diesel Sprays. In *ILASS Americas, 23rd Annual Conference on Liquid Atomization and Spray Systems*, Ventura, CA, May 2011.

[126] W. J. Pitz and C. J. Mueller. Recent progress in the development of diesel surrogate fuels. *Progress in Energy and Combustion Science*, 37(3):330–350, June 2011.

[127] S. Puhan, N. Saravanan, G. Nagarajan, and N. Vedaraman. Effect of biodiesel unsaturated fatty acid on combustion characteristics of a DI compression ignition engine. *Biomass and Bioenergy*, 34(8):1079–1088, Aug. 2010.

[128] R. D. Reitz, H. Ogawa, R. Payri, T. Fansler, S. Kokjohn, Y. Moriyoshi, A. Agarwal, D. Arcoumanis, D. Assanis, C. Bae, K. Boulouchos, M. Canakci, S. Curran, I. Denbratt, M. Gavaises, M. Guenthner, C. Hasse, Z. Huang, T. Ishiyama, B. Johansson, T. Johnson, G. Kalghatgi, M. Koike, S. Kong, A. Leipertz, P. Miles, R. Novella, A. Onorati, M. Richter, S. Shuai, D. Siebers, W. Su, M. Trujillo, N. Uchida, B. M. Vaglieco, R. Wagner, and H. Zhao. IJER editorial: The future of the internal combustion engine. *International Journal of Engine Research*, In press, 2019.

[129] H. Richter and J. B. Howard. Formation of polycyclic aromatic hydrocarbons and their growth to soot—a review of chemical reaction pathways. *Progress in Energy and Combustion Science*, 26(4):565–608, Aug. 2000.

[130] S. Riess, L. Weiss, A. Peter, J. Rezaei, and M. Wensing. Air entrainment and mixture distribution in Diesel sprays investigated by optical measurement techniques. *International Journal of Engine Research*, 19(1):120–133, Jan. 2018.

[131] J. Sandquist. Biofuels from waste – What is hydrothermal liquefaction and why is it interesting?, June 2019. URL https://blog.sintef.com/sintefenergy/what-is-hydrothermal-liquefaction-and-why-is-it-interesting/.

[132] S. Schlatter, B. Schneider, Y. M. Wright, and K. Boulouchos. N-heptane micro pilot assisted methane combustion in a Rapid Compression Expansion Machine. *Fuel*, 179:339–352, Sept. 2016.

[133] C. Schulz, B. Kock, M. Hofmann, H. Michelsen, S. Will, B. Bougie, R. Suntz, and G. Smallwood. Laser-induced incandescence: recent trends and current questions. *Applied Physics B*, 83(3):333–354, June 2006.

[134] D. L. Siebers and B. Higgins. Flame Lift-Off on Direct-Injection Diesel Sprays Under Quiescent Conditions. In *SAE Technical Paper Series*, Mar. 2001. doi: 10.4271/2001-01-0530.

[135] D. L. Siebers, B. Higgins, and L. Pickett. Flame Lift-Off on Direct-Injection Diesel Fuel Jets: Oxygen Concentration Effects. In *SAE Technical Paper Series*, Mar. 2002. doi: 10.4271/2002-01-0890.

[136] J. Sjöholm, R. Wellander, H. Bladh, M. Richter, P.-E. Bengtsson, M. Alden, U. Aronsson, C. Chartier, O. Andersson, and B. Johansson. Challenges for In-Cylinder High-Speed Two-Dimensional Laser-Induced Incandescence Measurements of Soot. *SAE International Journal of Engines*, 4(1):1607–1622, Apr. 2011.

[137] S. Skeen, K. Yasutomi, E. Cenker, B. Adamson, N. Hansen, and L. Pickett. Standardized Optical Constants for Soot Quantification in High-Pressure Sprays. *SAE International Journal of Engines*, 11(6):805–816, Apr. 2018.

[138] S. A. Skeen and K. Yasutomi. Measuring the Soot Onset Temperature in High-Pressure N-Dodecane Spray Pyrolysis. *Combustion and Flame*, 188:483–487, Feb. 2018.

[139] S. A. Skeen, J. Manin, K. Dalen, and L. M. Pickett. Extinction-based Imaging of Soot Processes over a Range of Diesel Operating Conditions. In *8th U. S. National Combustion Meeting*, May 2013.

[140] S. A. Skeen, J. Manin, L. M. Pickett, E. Cenker, G. Bruneaux, K. Kondo, T. Aizawa, F. Westlye, K. Dalen, A. Ivarsson, T. Xuan, J. M. Garcia-Oliver, Y. Pei, S. Som, W. Hu, R. D. Reitz, T. Lucchini, G. D'Errico, D. Farrace, S. S. Pandurangi, Y. M. Wright, M. A. Chishty, M. Bolla, and E. Hawkes. A Progress Review on Soot Experiments and Modeling in the Engine Combustion Network (ECN). *SAE International Journal of Engines*, 9(2):883–898, Apr. 2016.

[141] D. R. Snelling, K. A. Thomson, G. J. Smallwood, and m. L. Gülder. Two-dimensional imaging of soot volume fraction in laminar diffusion flames. *Applied Optics*, 38(12):2478, Apr. 1999.

[142] P. L. Spath and D. C. Dayton. Preliminary Screening – Technical and Economic Assessment of Synthesis Gas to Fuels and Chemicals with Emphasis on the Potential for Biomass-Derived Syngas. Technical Report NREL/TP-510-34929, National Renewable Energy Lab., Golden, CO. (US), Dec. 2003. URL https://www.osti.gov/biblio/15006100.

[143] A. Srna, G. Bruneaux, B. von Rotz, R. Bombach, K. Herrmann, and K. Boulouchos. Optical Investigation of Sooting Propensity of *n*- Dodecane Pilot/Lean-Premixed Methane Dual-Fuel Combustion in a Rapid Compression-Expansion Machine. *SAE International Journal of Engines*, 11(6):1049–1068, Apr. 2018.

[144] S. Steiner, C. Bisig, A. Petri-Fink, and B. Rothen-Rutishauser. Diesel exhaust: current knowledge of adverse effects and underlying cellular mechanisms. *Archives of Toxicology*, 90: 1541–1553, 2016.

[145] K. Sunde, A. Brekke, and B. Solberg. Environmental Impacts and Costs of Hydrotreated Vegetable Oils, Transesterified Lipids and Woody BTL—A Review. *Energies*, 4:845–877, 2011.

[146] C.-J. Sung and H. J. Curran. Using rapid compression machines for chemical kinetics studies. *Progress in Energy and Combustion Science*, 44:1–18, Oct. 2014.

[147] The CRECK Modeling Group. Complete mechanism (Version 1412, December 2014), 2014. URL http://creckmodeling.chem.polimi.it/menu-kinetics/menu-kinetics-detailed-mechanisms/menu-kinetics-complete-mechanism.

[148] D. R. Tree and K. I. Svensson. Soot Processes in Compression Ignition Engines. *Progress in Energy and Combustion Science*, 33(3):272–309, June 2007.

[149] S. R. Turns. *An Introduction to Combustion: Concepts and Applications*. McGraw-Hill, New York, 3rd edition, 2012. ISBN 978-0-07-338019-3.

[150] B. Van de Beld, E. Holle, and J. Florijn. The use of pyrolysis oil and pyrolysis oil derived fuels in diesel engines for CHP applications. *Applied Energy*, 102:190–197, Feb. 2013.

[151] K. Verbiezen, A. Donkerbroek, R. Klein-Douwel, A. van Vliet, P. Frijters, X. Seykens, R. Baert, W. Meerts, N. Dam, and J. ter Meulen. Diesel combustion: In-cylinder NO concentrations in relation to injection timing. *Combustion and Flame*, 151(1-2):333–346, Oct. 2007.

[152] X. Wang, Z. Huang, W. Zhang, O. A. Kuti, and K. Nishida. Effects of ultra-high injection pressure and micro-hole nozzle on flame structure and soot formation of impinging diesel spray. *Applied Energy*, 88(5):1620–1628, May 2011.

[153] Y. Wang, H. Liu, and C.-F. F. Lee. Particulate matter emission characteristics of diesel engines with biodiesel or biodiesel blending: A review. *Renewable and Sustainable Energy Reviews*, 64:569–581, Oct. 2016.

[154] C. K. Westbrook, H. J. Curran, W. J. Pitz, J. F. Griffiths, C. Mohamed, and S. K. Wo. The effects of pressure, temperature, and concentration on the reactivity of alkanes: Experiments and modeling in a rapid compression machine. *Symposium (International) on Combustion*, 27(1):371–378, Jan. 1998.

[155] C. K. Westbrook, W. J. Pitz, and H. J. Curran. Chemical Kinetic Modeling Study of the Effects of Oxygenated Hydrocarbons on Soot Emissions from Diesel Engines. *The Journal of Physical Chemistry A*, 110(21):6912–6922, June 2006.

[156] C. K. Westbrook, W. J. Pitz, O. Herbinet, H. J. Curran, and E. J. Silke. A comprehensive detailed chemical kinetic reaction mechanism for combustion of n-alkane hydrocarbons from n-octane to n-hexadecane. *Combustion and Flame*, 156(1):181–199, Jan. 2009.

[157] F. R. Westlye, M. Battistoni, S. A. Skeen, J. Manin, L. M. Pickett, and A. Ivarsson. Penetration and combustion characterization of cavitating and non-cavitating fuel injectors under diesel engine conditions. In *SAE Technical Paper Series*, 2016. doi: 10.4271/2016-01-0860.

[158] F. R. Westlye, K. Penney, A. Ivarsson, L. M. Pickett, J. Manin, and S. A. Skeen. Diffuse Back-Illumination Setup for High Temporally Resolved Extinction Imaging. *Applied Optics*, 56(17):5028, June 2017.

[159] C. Willert, B. Stasicki, J. Klinner, and S. Moessner. Pulsed operation of high-power light emitting diodes for imaging flow velocimetry. *Measurement Science and Technology*, 21(7): 075402, 2010.

[160] C. E. Willert, D. M. Mitchell, and J. Soria. An assessment of high-power light-emitting diodes for high frame rate schlieren imaging. *Experiments in Fluids*, 53(2):413–421, Aug. 2012.

[161] Z. Xiao, N. Ladommatos, and H. Zhao. The effect of aromatic hydrocarbons and oxygenates on diesel engine emissions. *Proceedings of the Institution of Mechanical Engineers, Part D: Journal of Automobile Engineering*, 214(3):307–332, Mar. 2000.

[162] Y. Xu and C.-f. F. Lee. Forward-illumination light-extinction technique for soot measurement. *Applied Optics*, 45(9):2046, Mar. 2006.

[163] T. Xuan, J. M. Desantes, J. V. Pastor, and J. M. Garcia-Oliver. Soot temperature characterization of spray a flames by combined extinction and radiation methodology. *Combustion and Flame*, 204:290–303, June 2019.

[164] T. Xuan, J. V. Pastor, J. M. García-Oliver, A. García, Z. He, Q. Wang, and M. Reyes. In-flame soot quantification of diesel sprays under sooting/non-sooting critical conditions in an optical engine. *Applied Thermal Engineering*, 149:1–10, Feb. 2019.

[165] J. Yanowitz, M. A. Ratcliff, R. L. McCormick, J. D. Taylor, and M. J. Murphy. Compendium of Experimental Cetane Numbers. Technical Report NREL/TP-5400-67585, National Renewable Energy Laboratory, 2017.

[166] Zeldovich. The Oxidation of Nitrogen in Combustion and Explosions. *Acta Physicochimica*, 21:577–628, 1946.

[167] H. Zhao and N. Ladommatos. Optical Diagnostics for Soot and Temperature Measurement in Diesel Engines. *Progress in Energy and Combustion Science*, 24(3):221–255, 1998.

A. Appendix

A.1 Non-ideal camera characteristics

See Appendix in **Article III** for details on the framework for dealing with non-ideal camera characteristics. The following section explains how to apply the framework to the flame luminosity correction techniques explained in **Article I**.

For the calculation of KL, the transmittance I_t/I_0 needs to be calculated from

$$\frac{I_t}{I_0} = \frac{I'_{tf,n} - I'_{tf,n-1}}{I'_{0,n} - I'_{0,n-1}}. \tag{A.1}$$

In order to generalize Equation A.1, $I'_{tf,n-1}$ is replaced with I'_f, which is the estimated/measured distribution of $I'_{f,n}$. I'_f can be estimated directly from $I'_{tf,n-1}$ and $I'_{tf,n+1}$ by calculating the mean image (see **Article I**)

$$I'_{f,n} = \frac{1}{2}\left(I'_{tf,n-1} + I'_{tf,n+1}\right). \tag{A.2}$$

However, when applying the optical flow algorithm, care should be taken since the measured raw quantities $I'_{tf,n-1}$ and $I'_{tf,n+1}$ contain the background noise distribution of the camera. If the optical flow is applied directly to the raw images both the flame luminosity distribution and the background noise distribution are transformed, making the estimated flame luminosity erroneous. Therefore, the raw flame luminosity images must be corrected such that no background noise distribution is present, i.e. first finding $I_{f,n-1}$ and $I_{f,n+1}$, by accounting for image lag[1]. The flame luminosity images can be calculated from

[1] In the following calculation, the assumption that $\beta = \alpha$ is made.

$$I_{f,n+1} = I'_{tf,n+1} - (BGs - \alpha I_{t,n}), \tag{A.3}$$

where

$$I_{t,n} = \frac{I'_{tf,n} - I'_{tf,n+1}}{1 + 2\alpha}. \tag{A.4}$$

By doing the same for $I_{f,n-1}$, optical flow can be applied in order to obtain the estimate flame luminosity during frame n.

$$I_{f,n} = optical flow(I_{f,n-1},\ I_{f,n+1}) \tag{A.5}$$

In order to apply $I_{f,n}$, it must be converted back to raw format:

$$I'_{f,n} = I_{f,n} + (BGs - \alpha I_{t,n}) \tag{A.6}$$

For the two camera technique, the same must be performed, where all flame images measured by the camera exposed to the backlight must be corrected before applying the transformation algorithm. As seen from the equations, the value of α is needed in order to apply the optical flow algorithm or the two-camera setup.

A.2 LED driver

The LED driver uses two capacitors of 2200 μF each and a MOSFET for switching the signal going to the LED. The driver is powered by a 10-36 V (supply voltage), which powers the capacitors, and 5-8 V (gate voltage) to power the MOSFET. The 10-36 V supply determines the power going to the LED. The trigger voltage is a 5 V signal, which switches the MOSFET on/off, consequently determining the duty cycle of the LED. During DBIEI measurements, this signal was 1-2 μs long and was synchronized with half the frame speed of the high speed camera (50 kfps). The LED driver was powered by 36 V for the supply voltage and 8 V for the gate voltage.

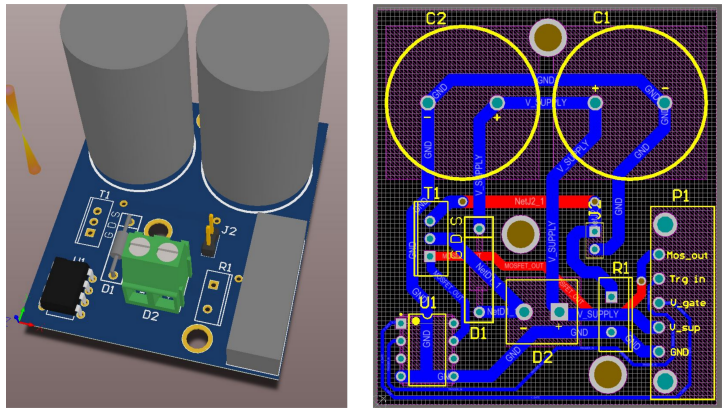

Figure A.1: LED driver circuit board.

Table A.1: Components used in the LED driver circuit.

Label	Component	Part name
C1/C2	Capacitor	EPCOS Capacitor 2200 μF
T1	MOSFET	Infineon IRFB3206PBF N-channel MOSFET
U1	MOSFET driver	Texas Instr. UCC37322P, MOSFET Power Driver
R1	Resistor	Vishay LTO50 10mΩ
D1	Diode	Fairchild UF4004 Diode
D2	LED	Luminus Devices SST-90-R-F11-HH100

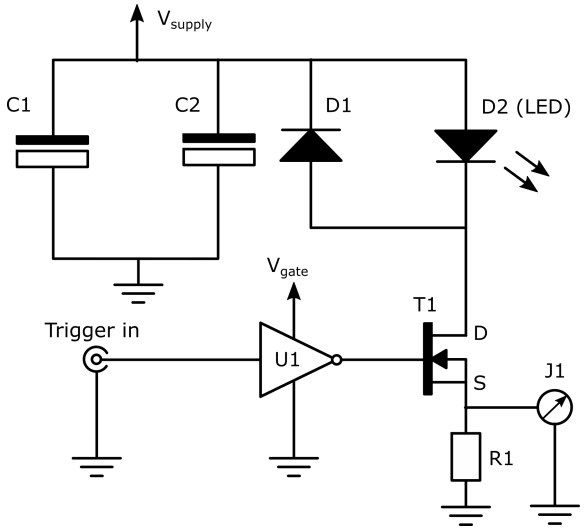

Figure A.2: LED driver circuit diagram. C1 and C2 are the capacitors, D1 is the diode, D2 is the LED, U1 is the MOSFET driver, T1 is the MOSFET, J1 is a voltmeter.

A.3 OACIC

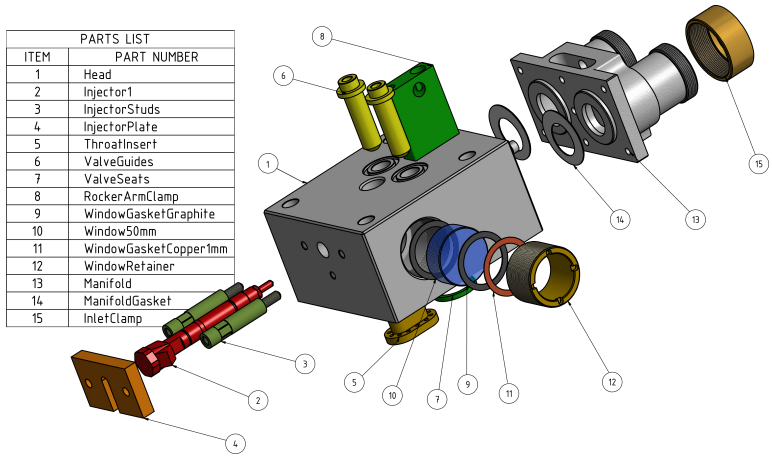

PARTS LIST	
ITEM	PART NUMBER
1	Head
2	Injector1
3	InjectorStuds
4	InjectorPlate
5	ThroatInsert
6	ValveGuides
7	ValveSeats
8	RockerArmClamp
9	WindowGasketGraphite
10	Window50mm
11	WindowGasketCopper1mm
12	WindowRetainer
13	Manifold
14	ManifoldGasket
15	InletClamp

Figure A.3: Assembly drawing of the OACIC.

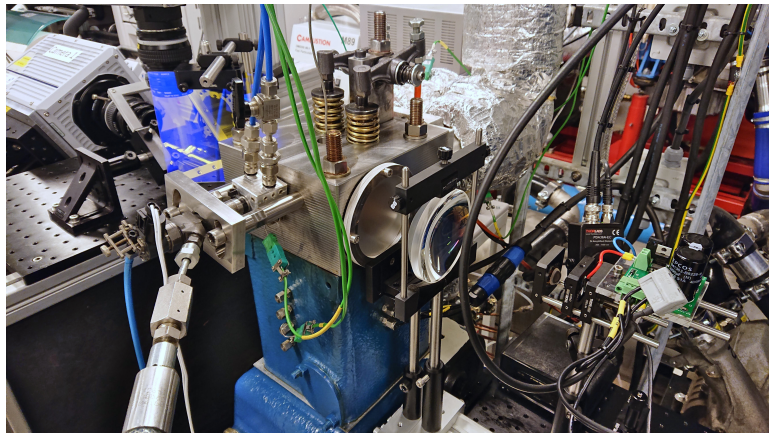

Figure A.4: The OACIC with the optical setup.

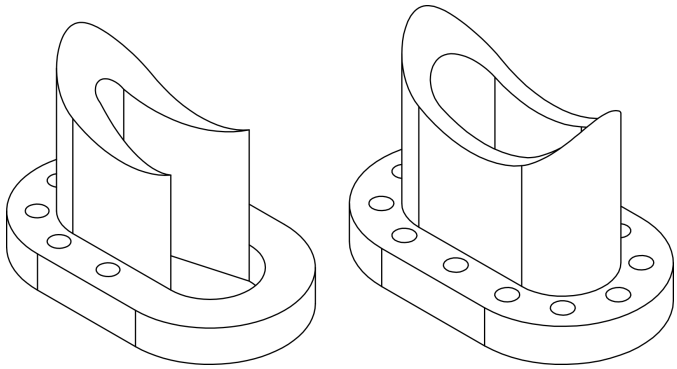

Figure A.5: The throat insert used in the OACIC was improved in order to minimize spray-wall interaction. The CR changed from 16.36 to 15.93 when using the improved design. Left: improved design, right: old design.

Article I

Karl Oskar Pires Bjørgen, David Robert Emberson and Terese Løvås

Diffuse Back-Illuminated Extinction Imaging of Soot: Effects of Beam Steering and Flame Luminosity

Published in SAE International 15.01.2019
DOI: 10.4271/2019-01-0011

Article II

Karl Oskar Pires Bjørgen, David Robert Emberson and Terese Løvås

Optical Measurements of In-Flame Soot in Compression-Ignited Methyl Ester Flames

Published in Energy and Fuels 04.07.19
DOI: 10.1021/acs.energyfuels.9b01467

energy&fuels

Article

Cite This: Energy Fuels 2019, 33, 7886−7900

pubs.acs.org/EF

Optical Measurements of In-Flame Soot in Compression-Ignited Methyl Ester Flames

Karl Oskar Pires Bjørgen,* David Robert Emberson, and Terese Løvås

Department of Energy and Process Engineering, Norwegian University of Science and Technology, 7491 Trondheim, Norway

ABSTRACT: This study investigates in-flame sooting characteristics of biodiesel surrogates in compression-ignited spray flames. The aim of the study is to produce reliable experimental data on in-flame soot for validation of kinetic mechanisms and soot models. A rapeseed oil biodiesel [rapeseed oil methyl ester (RME)] was compared to neat methyl oleate (MO) and methyl decanoate (MD). In addition, neat *n*-heptane was chosen as a baseline fuel and the effect of blending *n*-heptane and MD on soot production was investigated. The study was performed in a single-cylinder research engine with optical access to a single spray for varying ambient gas temperatures (825−990 K). The in-flame soot was measured by a high-speed diffuse back-illuminated extinction imaging system, and the flame lift-off length (FLOL) and the corresponding estimated equivalence ratio at FLOL was measured from high-speed OH* chemiluminescence imaging. Results show that RME has the highest tendency to soot, closely followed by MO, independent of the FLOL equivalence ratio. Having almost identical fuel properties, this is likely due to the higher degree of unsaturation in RME compared to MO. When comparing MD to *n*-heptane, a much lower in-flame soot production rate is observed despite the fact that MD has a higher number of carbon−carbon bonds, concluding that the high fuel oxygen ratio in MD is effectively reducing in-flame soot production. Generally, for FLOL equivalence ratio leaner than ∼2, no in-flame soot was produced for all ambient gas temperatures. The in-flame soot production rate also showed a clear ambient gas temperature dependence for constant FLOL equivalence ratios, where the soot production rate increased with increased gas temperatures.

1. INTRODUCTION

The compression ignition (CI) engine is highly relevant for research because of the higher fuel efficiency compared to the spark ignition engine. In the coming years, a low emission engine will be required to meet stringent regulations set by authorities. This requires a full understanding of the phenomena occurring in the combustion chamber. In particular, the production of soot in combusting fuel sprays is not fully understood.[1] An increased understanding of the in-flame soot phenomena will help engine and fuel designers predict emissions of particulate matter (PM) and heat transfer due to radiation from in-flame heated soot particles.

Oxygenated fuels such as biodiesel are important to study due to the increased use of diesel fuel at present. The European fuel standard EN590 allows diesel fuel to contain up to 7 wt % of biodiesel in commercial diesel, and countries like China, India, and Brazil intend to accelerate investments in biofuel production in the coming decade.[2] The addition of an oxygenated fuel has a large impact on the combustion process, affecting the production of soot in the flame and the resulting tail pipe PM substantially. Since soot production is largely a function of chemistry, a detailed mechanism of the gas-phase fuel oxidation, a numerical representation of the physical processes and a soot model are needed. Soot predictions in compression-ignited sprays based on computational fluid dynamics (CFD) simulations are currently showing discrepancies and are not well understood.[3] The development of existing soot models is still highly dependent on experiments, emphasizing the need for reliable in-flame soot measurements.

Biodiesel does not have a clearly defined molecular composition, varying based on the feedstock. Feedstock include oils from rapeseed, soybean, palm, and sunflower. Through transesterification of the oil and an alcohol, a mixture of various alkyl esters is produced, which constitutes the biodiesel fuel. The most common biodiesel consists of methyl esters produced from methanol and vegetable oils. Besides a maximum allowed content of linolenic methyl esters (12 wt %) and polyunsaturated methyl esters (1 wt %), the current regulation only limits the resulting physical and chemical parameters such as cetane number, boiling point, viscosity, etc., allowing the composition to vary greatly (European standard EN14214).

This variation imposes challenges to the definition of biodiesel and the fuel surrogates used in modeling. To reduce the calculation time of simulations, a fuel surrogate which satisfies target properties of the real fuel is chosen. The target properties of the surrogates can be C/H/O ratio, heating value, sooting tendencies, cetane number, etc. This has previously been achieved by using a single- or multicomponent surrogate that meets the target properties.

Existing surrogate fuel components for biodiesel consist of methyl esters of different carbon chain lengths and with varying saturation, and normal alkanes. Fisher et al. developed a detailed mechanism for methyl butanoate and methyl formate.[4] Although having a methyl ester group, methyl butanoate has a short carbon chain length of four, which was shown not to reproduce the kinetic features of the long-chain methyl esters found in biodiesel (16−18 carbon atoms).[5] To improve the combustion characteristics, a mechanism for

Received: May 9, 2019
Revised: June 30, 2019
Published: July 5, 2019

DOI: 10.1021/acs.energyfuels.9b01467
Energy Fuels 2019, 33, 7886−7900

methyl decanoate (MD) was developed.[6] Computed results using the MD mechanism were validated with MD in a research engine, and rapeseed oil methyl esters (RMEs) in a jet-stirred reactor (JSR). Unlike methyl butanoate, MD was able to capture the early formation of carbon dioxide, which differentiates biodiesel fuels from diesel fuels. Further work included adding unsaturated molecules to the surrogate fuel blend.[7] Since most of the methyl esters in biodiesel are unsaturated, adding unsaturated compounds to the MD mechanism, i.e., methyl-5-decenoate (MD5) and methyl-9-decenoate (MD9), could improve the combustion and sooting characteristics. MD9 was chosen because the double bond is located in the same position as the one in methyl oleate (MO) and as the first double bond in methyl linoleate and methyl linolenate. MD5 was chosen to highlight the effect of position of the double bond in the carbon chain. Simulations of the oxidation of the ternary surrogate blend of *n*-heptane (HP), MD, and MD9 were compared to experiments of RME under diesel-like conditions in a jet-stirred reactor (JSR)[8] and showed good global agreement. In 2011, Westbrook et al. presented a detailed mechanism for longer methyl esters.[9] The mechanism includes the five major components of biodiesel: methyl stearate, methyl oleate, methyl linoleate, methyl linolenate, and methyl palmitate, being able to mimic a real biodiesel with different compositions.

MD has previously been studied optically in optical engines and combustion vessels at numerous occasions.[10−14] This is mainly because it has proven to be a fitting surrogate fuel for biodiesel, as well as because it produces small amounts of in-flame soot due to a high oxygen content, making it suitable for certain measurement techniques that require low in-flame soot. The interest in oxygenated fuels is mainly driven by the reduced in-flame soot and possibly reduced PM. Using oxygenated fuels has been shown to facilitate the concept of leaner lifted-flame combustion,[12,15] where the aim is to produce nonsooting, mixing-controlled flames in CI engines to eliminate PM engine-out emissions.

An investigation of MD and diesel fuel combustion in an optical direct injection (DI) engine was conducted by Cheng et al.[11] MD was shown to produce very small amounts of in-flame soot compared to diesel fuel, although having similar flame lift-off lengths (FLOLs) during mixing-controlled combustion. The calculated equivalence ratio at flame lift-off location was significantly lower for MD compared to diesel, which likely explains the low level of in-flame soot.

Several oxygenated fuels and blends were tested in a constant-volume vessel by Manin et al.,[10] where the FLOL and in-flame soot were measured. They concluded that the total in-flame soot mass produced is inversely proportional to the oxygen content of the fuel. In addition, the comparison between a tripropylene glycol monomethyl ether (TPGME)−alkane blend and neat ND, both having similar oxygen contents (measured by fuel oxygen ratio), showed that the location of the oxygen atoms in the molecule is important for the in-flame soot, where the TPGME−alkane blend yielded the lowest in-flame soot level. Also, for a given ignition delay time (IDT), FLOL tended to increase with addition of oxygen to the fuel, which also supports the statement of IDT and FLOL not being one-to-one correlated.[16]

To investigate the effect of molecular structure on soot processes in spray combustion, numerical simulations for several oxygenated fuels and blends (including MD) were performed by Park et al.[17] Soot precursors (acetylene) in the spray combustion were shown to decrease with increased fuel oxygen ratio and decreased number of carbon−carbon bonds in the molecule. The soot formation for fuel blends with similar fuel oxygen ratio and number of C−C bonds was mainly governed by the IDT and the FLOL. This study also highlighted that in-flame soot production is highly dependent on the molecular structure, as well as the fuel−air mixing.

A comparison between a long and a short carbon chain biodiesel was conducted in a small bore engine by Zhang et al.[18] They concluded that an increase in carbon chain length leads to reduced IDTs for the long-chain biodiesel, increasing the mixing-controlled burn phase duration. The long-chain biodiesel produces more soot due to less premixing and a lower fuel oxygen content.

The authors did not find any previous studies conducting optical measurement of in-flame soot for longer-chain neat methyl esters such as MO. In this study, the combustion of a commercial RME, neat MO, neat MD, neat *n*-heptane, and a 50% molar blend of MD and *n*-heptane has been investigated for varying ambient gas temperature conditions. MO is chosen because of the large content of it in RME, making the data valuable for future validation of CFD and kinetic simulations of RME. Also, by comparing MO to RME, the observed difference will be attributed to the remaining components in RME. MD (neat or blended with an alkane) is chosen because it is a widely used surrogate fuel for biodiesel. The aim is to compare combustion and in-flame soot characteristics of a real biodiesel to possible surrogate fuels under enginelike conditions and to examine the effect of fuel-bound oxygen and degree of unsaturation on these characteristics.

2. METHODS

2.1. Optical Accessible Compression Ignited Chamber (OACIC). The experiments were performed in the Optical Accessible Compression Ignited Chamber (OACIC) at the Department of Energy and Process Engineering at the Norwegian University of Science and Technology (NTNU). The OACIC is a modified four-stroke engine (Lister 12 CS) where the head has been redesigned for optical access. The combustion chamber located in the head is connected to the engine's swept volume via an interchangeable throat (Figure 1). A second-generation Bosch solenoid common rail injector is installed in the chamber, fitted with a single-hole nozzle having an

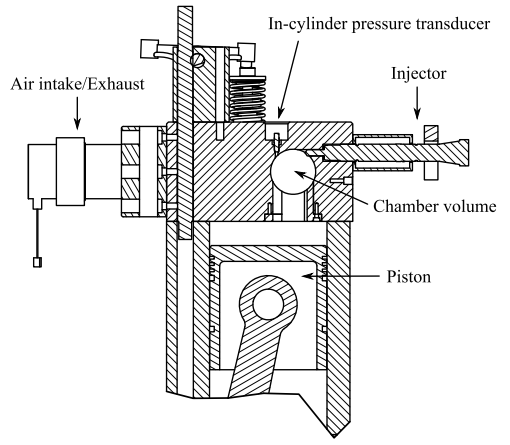

Figure 1. Cross section of the OACIC.

DOI: 10.1021/acs.energyfuels.9b01467
Energy Fuels 2019, 33, 7886−7900

angle of 62° with respect to the nozzle axis. The intake and exhaust valves are taken from the original engine and are installed in the head. The OACIC is only lubricated with light lubricants, to avoid any PM emissions associated with engine oil. A summary of engine dimensions and details are given in Table 1.

Table 1. Engine Specifications of the OACIC

engine type	four-stroke, single-cylinder, indirect DI engine
bore/stroke	130 mm/140 mm
displaced volume	1.85 L
compression ratio (CR)	15.9
injector	Bosch CR second generation
injector nozzle	single hole, DSLA124P1659 62° w.r.t. central axis
hole diameter	0.12 mm
injection pressure	1000 bar
injection duration	4.48 ms
injection timing	2.7° before top dead center (TDC)

The combustion chamber is cylindrical in shape with a diameter of 50 mm and a height of 40 mm, sealed with two fused-silica windows (63 mm in diameter and 25 mm thick) and copper gaskets. The windows allow a line-of-sight view of the chamber and are retained by two threaded rings.

The piston and crank are driven by an alternating current motor operated at 500 rpm. The position of the crank shaft is measured by a magnetic shaft encoder, with 3200 readings per revolution, resulting in 0.1125 crank angle degrees cycle resolution (37.5 μs time resolution for 500 rpm). A dynamic pressure sensor (Kistler 6052C) synchronized with the shaft encoder records motored and combustion pressures in the chamber.

2.1.1. Fuel System. The injection pressure is driven by an air-driven pump. The injections are controlled by an injection driver (National Instruments Drivven) through LabVIEW and only triggered when the injection pressure is within ±10 bar during a cycle, resulting in a standard deviation of 2% of the target pressure. The total volume of the fuel system is kept to a minimum to minimize waste of fuel. A minimum volume of ∼200 mL fuel for a complete fuel measurement was required. The injector is water-cooled by a cooling jacket fitted around the injector body.

2.1.2. Intake Air and Exhaust System. The intake air system consists of a large air box with an orifice plate for measuring the volume flow rate of the intake air. The intake air is then compressed by a roots compressor coupled to a settling tank to dampen pressure oscillations before the OACIC. A 2 kW electric flow heater is installed near the intake manifold, heating the air up to a maximum of ∼150 °C. The inlet air temperature is measured by a K-type thermocouple, and the inlet air pressure is measured by a high-speed absolute pressure sensor (Kistler 6011) located close to the inlet manifold. The temperatures of the exhaust gases are also measured by a K-type thermocouple.

2.1.3. Thermal Conditions. The thermal conditions of the OACIC have been assessed by measuring the temperature during motoring under several conditions. The cylinder is constantly kept at 90 °C by heaters, while the head is neither externally cooled nor heated. A K-type thermocouple is installed in the head located 21 mm from the combustion chamber wall, giving an indication of the head temperature. Additionally, a measurement performed using a stripped injector installed with a thermocouple in the center axis allowed for measurement of the nozzle tip temperature during motoring. The injector tip temperature reached ∼160 °C during stable operation of the OACIC. During ordinary operation of the OACIC for optical measurements, skip-fire mode was enabled with a minimum of 10 motored cycles before each combustion cycle, ensuring that the thermal conditions are more stable during the operating period. This also ensures that no postcombustion gases from the previous combustion cycles are present in the chamber during measurement.

2.1.4. Thermodynamic Analysis. The in-cylinder gas pressure is a common measurement in engine research and is considered a highly reliable measurement. However, the in-cylinder gas temperature is a much harder quantity to measure. In this study, an estimation of the in-cylinder ambient gas temperature was made, involving a combination of in-cylinder pressure measurements and a thermodynamic model available in the commercial software LOGEresearch by LOGE AB.

A zero-dimensional analysis of the thermodynamic conditions in the chamber has been made using a first-law approach. The inputs to the calculation were absolute inlet air pressure, inlet air temperature, engine dimensions, wall temperature, and in-cylinder gas pressure. The in-cylinder gas temperature is iteratively calculated based on the energy conservation equation and ideal gas law, and the heat transfer is modeled by the Woschni correlation.[19] The model also takes into account the temperature dependence of the gas properties.

Several motored pressures with varying inlet conditions were acquired and compared to the modeled pressure. Since the modeled pressure did not include blowby, the modeled pressure yielded a higher in-cylinder pressure. Mass loss due to blowby was accounted for by decreasing the compression ratio in the model such that the measurements matched the modeled pressure. This obviously did not give the correct total mass in the chamber but yielded a good estimation of the in-cylinder temperature and density. Consistency of the blowby for the entire range of conditions in the OACIC was checked by repeating this for all measured conditions in the OACIC, resulting the same reduced compression ratio for all conditions. The reduced compression ratio was found to be 12.6 (geometrical CR = 15.9).

Four thermodynamic conditions were chosen in this study. The ambient gas density was kept constant at ∼16.6 kg/m^3 for all conditions, while the ambient gas temperature was varied. The conditions are given in Table 2.

Table 2. Calculated Average Thermodynamic Conditions of the Ambient Gas in the OACIC[a]

condition	1	2	3	4
ρ_{TDC} (kg/m^3)	16.7	16.7	16.6	16.6
P_{TDC} (bar)	39.7	42.1	44.4	46.7
T_{TDC} (K)	825	877	928	978
T_{max} (K)	837	890	941	990
T_{span} (K)	12	13	13	12

[a] ρ_{TDC}, P_{TDC}, and T_{TDC} are density, pressure, and temperature of the ambient gas, respectively, at top dead center (TDC) during motoring of the OACIC. T_{max} and T_{span} are the maximum ambient gas temperature and the temperature span during the fuel injection period (with combustion), respectively. Temperature span is defined as the difference between the maximum and minimum ambient gas temperature during the injection period. The table is based on combustion of all fuels.

The temperature distribution near TDC in the chamber is heterogeneous, mainly due to cooling of the gas near the chamber walls. Since the fuel spray is directed toward the center of the chamber, the center gas temperature, which is less affected by the wall cooling, is a more relevant measure to consider as the entrained gas temperature between start of injection (SOI) and start of combustion.

During combustion in the chamber, the pressure increases above the motored pressure due to local heat release in the spray combustion, expanding the combusting gases. The expansion causes the air in the chamber to compress, increasing the ambient gas temperature. The increase in temperature due the combustion was estimated from the in-cylinder combustion pressure. Adiabatic compression of the nonreacting air was assumed and the temperature increase was calculated based on the numerical integration of

DOI: 10.1021/acs.energyfuels.9b01467
Energy Fuels 2019, 33, 7886−7900

$$\frac{dT}{dt} = \frac{R \cdot T}{c_p(T) \cdot P} \frac{dP}{dt} \quad (1)$$

with air being the compressed medium, R the specific gas constant, and c_p the temperature-dependent specific heat capacity for constant pressure. The initial temperature used in the calculation is taken from the motored ambient gas temperature mentioned above at the start of combustion. Results of the average ambient gas temperature during combustion for all conditions and fuels are shown in Figure 2. The ambient gas temperature variation over the period of injection is relatively stable, varying by ∼12 K for all conditions.

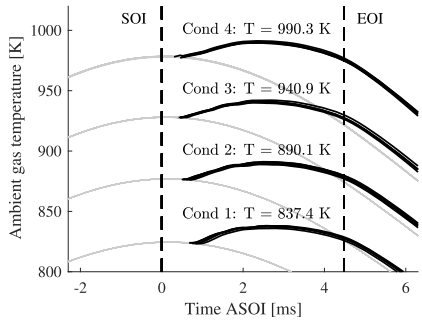

Figure 2. Estimated average ambient gas temperature in the chamber during motored and combustion cycles for all fuels and conditions. Maximum temperatures (T_{max}) during the injection period, start of injection (SOI), and end of injection (EOI) are indicated.

2.2. Fuels. The dominating component in the current RME fuel is the unsaturated ester MO (see Table 3) with 61.8 wt %, followed by methyl linoleate with 18.4 wt %. Important physical and chemical properties are listed in Table 4 for all fuels. MD had a purity of ≥99% and the MO 96%.

Table 3. Molecular Composition of the Rapeseed Oil Methyl Ester (RME)

component	wt %
methyl oleate (C18:1)	61.8
methyl linoleate (C18:2)	18.4
methyl linolenate (C18:3)	7.3
methyl palmitate (C16:0)	4.4
methyl stearate (C18:0)	1.6
other	6.5

As RME contains a large portion of MO, their properties should be similar, which is confirmed in Table 4. The second and third largest components in RME are methyl linoleate and methyl linolenate, where the degree of unsaturation of these molecules are 3 and 4, respectively. This is the reason for RME having a 10% higher degree of unsaturation compared to MO. An increase in level of unsaturation of neat methyl esters is known to decrease the cetane number, the kinematic viscosity, heat of combustion, and melting point.[20] In addition, the C/H/O ratios of RME and MO are very similar, resulting in a similar fuel oxygen ratio (Ω_f). The calculated fuel oxygen ratio Ω_f is defined as the ratio between the oxygen present in the fuel and the amount of oxygen needed to convert all carbon and hydrogen in the fuel molecule into carbon dioxide and water[21]

$$\Omega_f = \frac{n_O}{2n_C + 0.5n_H} \quad (2)$$

where n_O, n_C, and n_H are the number of oxygen, carbon, and hydrogen atoms in the fuel molecule, respectively. MD is a shorter-chain methyl ester compared to RME and MO, resulting in some properties being completely different. The main difference is the much higher fuel oxygen ratio of 6.06, compared to ∼3.60 of the long-chain methyl esters. Moreover, the combined effect of a lower degree of unsaturation, oxygen content, and number of C−C bonds results in MD having a much lower expected tendency to produce soot compared to the longer-chain methyl esters.[17,22] The main similarities between MD and RME/MO are the density and the lower heating value, resulting in similar total energy injected when using the same injection strategy.

The choice of including neat *n*-heptane to this study is mainly motivated by having a baseline fuel, which is thoroughly investigated previously and which is commonly used as a component in biodiesel surrogates. The 50% molar blend of *n*-heptane and methyl decanoate (HP−MD) will highlight the effects on soot production when changing some key properties such as fuel oxygen ratio, number of C−C bonds, and degree of unsaturation.

2.3. Diffuse Back-Illuminated Extinction Imaging (DBIEI) of Soot. For measuring in-flame soot, diffuse back-illuminated extinction imaging (DBIEI) was used. DBIEI is a nonintrusive two-dimensional line-of-sight measurement, where the principle of light extinction is applied, which occurs when light is either absorbed or scattered by soot particles present in the light path. The optical depth of the soot particle cloud can be calculated from the Beer−Lambert law,[33] where the transmittance τ, being the ratio between the incident light intensity I_t and the transmitted light intensity I_0, can be related to the optical depth KL as

Table 4. Physical and Chemical Properties of Rapeseed Oil Methyl Ester (RME), Methyl Decanoate (MD), Methyl Oleate (MO), *n*-Heptane, and a 50% Molar Blend of *n*-Heptane and Methyl Decanoate (HP−MD)

	unit	RME	MD	MO	*n*-heptane	HP−MD
lower heating value	MJ/kg	37.82[a]	36.7	40.1[f]	44.6[g]	
carbon	wt %	77.1	70.9	77.0	83.9	75.5
hydrogen	wt %	12.1	11.9	12.2	16.1	13.4
oxygen	wt %	10.9	17.2	10.8	0.0	11.2
fuel oxygen ratio Ω_f[j]	mol %	3.62	6.06	3.57	0.00	3.01
density at 15 °C	g/mL	0.8833[a]	0.8728	0.8704	0.6880[g]	
viscosity at 40 °C	mm^2/s	4.434[a]	1.72[e]	4.51[e]	0.34[i]	
cetane number		57.1[a]	47.9[c]	57[b]	56[d]	
derived cetane number (DCN)			51.6[f]	59.3[k]	53[l]	
normal boiling point	°C	350.2[a]	225[b]	350[b]	98.52[h]	
degree of unsaturation	mol^{-1}	2.21	1	2	0	0.5
number of C−C bonds	#/mol	16.9	9	17	6	7.5

[a]Measured. [b]Ref 23. [c]Ref 24. [d]Ref 25. [e]Ref 26. [f]Ref 27. [g]Ref 28. [h]Ref 29. [i]Ref 30. [j]Ref 21. [k]Ref 31. [l]Ref 32.

DOI: 10.1021/acs.energyfuels.9b01467
Energy Fuels 2019, 33, 7886−7900

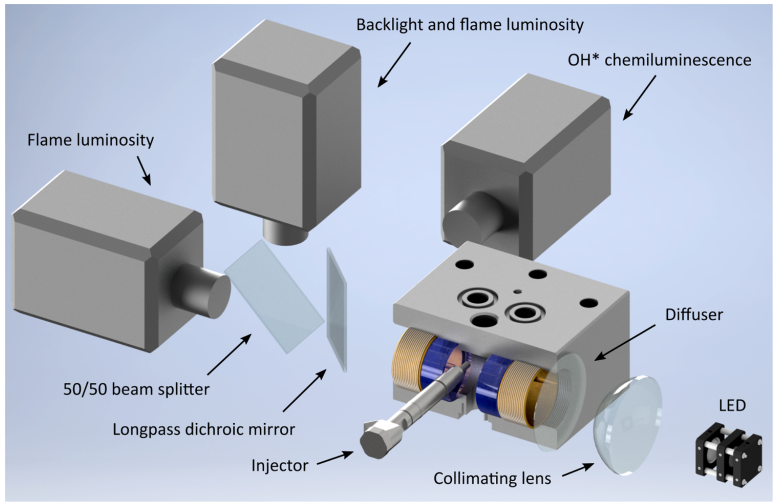

Figure 3. Optical setup. Components from right to left: 628 nm LED with focusing lenses, collimating lens (focal length 100 mm, diameter 100 mm), engineered diffuser (divergence angle 15°, diameter 100 mm); long-pass dichroic mirror (cuton wavelength, 480 nm) and 50/50 visible light beam splitter.

$$\tau = \frac{I_t}{I_0} = \exp\left(-\int_L k(x)\,\mathrm{d}x\right) = \mathrm{e}^{-KL} \tag{3}$$

where $k(x)$ is the local dimensional extinction coefficient, x is the spatial position along the light path, K is the path-averaged dimensional extinction coefficient, L is the path length through the soot particle cloud, and the product KL is the observed optical depth of the soot particle cloud in a line-of-sight light extinction measurement.

The measured optical depth KL can be related to the soot volume fraction[34] f_v by

$$f_v = \frac{\lambda K}{k_e} \tag{4}$$

where k_e is the nondimensional extinction coefficient and can be described as $k_e = 6\pi E(m)(1 + \alpha_{sa})$. $E(m)$ is the imaginary part of the refractive index function (m being the complex refractive index of the soot particles), while α_{sa} is the scattering-to-absorption ratio in the measurement (calculated from Rayleigh−Debye−Gans for fractal aggregate theory). α_{sa} is known to be nonconstant mainly dependent on the size of the particles, but often assumed as close to zero for spray combustion. Values of $E(m)$ and α_{sa} recommended by engine combustion network (ECN)[35] for the incident light source wavelength of 628 nm are chosen for the quasi-steady period of the high-pressure spray combustion for all fuels tested, $k_e = 7.2$. The assigned uncertainty of k_e is ±20%. The quasi-steady period for the current study will be defined later.

2.4. Optical Setup. A detailed description of the DBIEI setup used in the current study is thoroughly described by Bjørgen et al.,[36] and is similar to setups used by Pastor et al.[37] and Skeen and Yasutomi.[38]

As shown in Figure 3, a high-power light-emitting diode (LED) with wavelength of 628 nm [full width at half-maximum (FWHM) = 15 nm] was used as the back-illumination light source for the DBIEI. The light from the LED is directed on to an engineered diffuser (spreading angle of 15°) and further directed through the chamber volume. The angular distribution from the diffuser is measured to have a uniform intensity distribution across over the specified 15°. The setup is designed according to the recommended criteria described by Westlye et al.[39] for complete abatement of beam steering effects, due to large density gradients normally present in high-pressure spray combustion.

The LED is pulsed by an in-house built driver, enabling short and high-power light pulses. The light pulses are synchronized with every second exposure of the main high-speed camera, enabling an alternating measurement of the transmitted intensity distribution I_{tf} (LED light and flame luminosity superimposed) and the flame luminosity intensity distribution I_f (flame luminosity only). A second high-speed camera with equal optics, measuring the same field of view as the main camera through a 50/50 visible light beam splitter, is synchronized with the main camera. However, the second camera is given a small time shift such that it does not overlap with the light pulses. This ensures that the second camera is measuring I_f shortly before the I_{tf} measurement. The information obtained from the second camera is then used to correct for the flame luminosity effects on the main camera, giving the true transmitted intensity distribution $I_t = I_{tf} - I_f$.

Both high-speed cameras used were Photron FASTCAM SA5, fitted with Nikkor 50 mm f/1.2 objective lenses and 500D close-up lenses. The spectral filters used were centered at 634 nm (FWHM 70 nm), and neutral density filters were used for adjusting the light intensity such that the measurement was close to the saturation limit of the cameras, maximizing the dynamic range of the measurement. All measurements were recorded at 100 kfps, with 1 μs exposure time and a resolution of 320 × 192, where the pixel scale was 0.16 mm/pixel.

2.5. OH* Chemiluminescence Imaging. In addition to measuring in-flame soot distribution, instantaneous natural luminosity of the flame in the UV wavelength range was measured simultaneously. This spectral interval is known to be dominated by chemiluminescence from short-lived exited-state OH (OH*), indicative of high temperature and stoichiometric combustion conditions in the flame.[40] A high-speed measurement of the OH* distribution gives a measure of when and where high-temperature combustion starts, and the instantaneous FLOL. The latter is as previously mentioned closely related to in-flame soot formation.[41]

The OH* distribution was measured using a Lambert Instruments gated intensifier (II25) fitted on to a Photron FASTCAM SA-X2. A UV 100 mm f/2.8 CERCO 2178 lens from Sodern fitted with a spectral filter centered at 307 nm (FWHM 10 nm) was used. The measurement was synchronized to half the speed of the DBIEI

DOI: 10.1021/acs.energyfuels.9b01467
Energy Fuels 2019, 33, 7886−7900

cameras, i.e., 50 kfps, to match the light extinction measurement frame rate. The gating time of the intensifier was set to 5 μs and centered to the DBIEI main camera exposure position. The resolution of the camera was 256 × 256, with a pixel scale of 0.215 mm/px. The same field of view as the DBIEI setup was captured by using a dichroic mirror, reflecting light with shorter wavelength than 480 nm and transmitting longer wavelengths to the DBIEI measurement setup.

2.6. Analysis of OH* Chemiluminescence. The FLOL was defined as the distance along the central axis between the nozzle orifice and the location, where the OH* chemiluminescence reached 50% of a predefined threshold value. The characteristic OH* intensity value was defined as where the OH* signal leveled off after the initial steep increase, denoted as the OH* signal shoulder value in Figure 4.

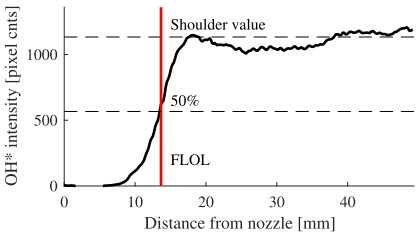

Figure 4. OH* intensity plotted along the central axis together with the definition of FLOL.

The pixel intensities during the quasi-steady period did not saturate. Since the OH* signal slope at the location of the FLOL is relatively large, the determination of the shoulder value did not affect the FLOL greatly.

2.6.1. Steady FLOL. Having measured the instantaneous OH* distribution for 10 injections over three runs, an average of 30 injections could be used to determine the FLOL for all conditions and fuels. Also, by identifying the period where the flame is fully developed, also known as the quasi-steady period, i.e., during the mixing-controlled combustion phase, after the premixed combustion phase, and before end of injection, a total of 2730 images per fuel and condition were used for the ensemble-averaged OH* image.

2.6.2. Equivalence Ratio at Flame Lift-Off Location. The FLOL indicates the amount air that has been entrained in the fuel spray prior to combustion. A shorter FLOL indicates less entrained air and vice versa. To assess the sooting characteristics between the fuels and conditions, the equivalence ratio at the flame lift-off location is needed. A model for a nonreacting spray was used for assessment of the equivalence ratio at flame lift-off location.[42,43] The model is assumed to be valid for the current measurements since no combustion occurs upstream of the flame lift-off location. The cross-sectional average equivalence ratio at flame lift-off location is given by

$$\bar{\phi}(H) = \frac{2(A/F)_{st}}{\sqrt{1 + 16(H/x^+)^2} - 1} \tag{5}$$

where H is the FLOL, $(A/F)_{st}$ is the stoichiometric air−fuel ratio by mass, and x^+ is the characteristic length scale

$$x^+ = \sqrt{\frac{\rho_f}{\rho_a}} \frac{\sqrt{C_a}\cdot d}{\tan(\theta/2)\cdot a} \tag{6}$$

where ρ_f is the density of the fuel, ρ_a is the ambient gas density, C_a is the area contraction coefficient, d is the nozzle diameter, a is a constant equal to 0.75,[44] and $\theta/2$ is the half-spreading angle of the spray. A value of 0.85 was chosen as the C_a based on measurements of various nozzles in ref 43. The nozzle diameter was d = 0.12 mm. The primary effect on the spreading angle is shown to be the ambient gas/fuel density ratio[43] (ρ_a/ρ_f). The calculation of $\bar{\phi}(H)$ was not performed with intention of evaluating the absolute value, but rather to investigate trends.

As the ambient gas density in this study is kept constant at 16.6 kg/m^3, only the fuel density is changing between the tests. Since the fuel densities for RME, MD, and MO are relatively similar, the spreading angles for the sprays under all conditions tested are expected to be similar. This means that $\bar{\phi}(H)$ is mainly sensitive to changes in $(A/F)_{st}$ and H. The spreading angle is therefore calculated using an empirical relation only considering ambient gas/fuel density ratio from ref 43. Note that heptane and the MD−heptane blend have much lower fuel density than the neat methyl esters, making the comparison between these more uncertain.

2.7. Analysis of In-Flame Soot. *2.7.1. Total Soot Mass.* The in-flame soot measured by the DBIEI can be evaluated in several ways. The line-of-sight measurement of KL provides a measure of the total soot mass within the collection cone of a pixel on the camera sensor. Based on eq 4 and assuming that the angle of the collection cone in the DBIEI setup is small, the total mass of soot present in the collection cone of the objective lens is given by

$$m_{soot} = \rho_{soot} \frac{\lambda \cdot KL}{k_e} \cdot \Delta A_{px} \tag{7}$$

where ρ_{soot} is the density of soot and ΔA_{px} is the projected pixel area in the focal plane. In this calculation, the uncertainty from k_e (as discussed earlier) and ρ_{soot} must be combined. Values for ρ_{soot} found in the literature range from 1.12 to 1.8 g/cm^3.[45,46] The chosen value of soot density in this study was 1.8 g/cm^3 since this is most commonly reported for in-flame diesel combustion. Due to restriction from the combustion chamber geometry, the entire flame is not measured by the DBIEI during the quasi-steady period. Hence, the total soot mass is only captured during the premixed combustion stage, where the entire flame is measured. By applying this method to the premixed burn phase, the temporal development of the soot mass can be evaluated. The soot mass production rate is calculated as the temporal differential of the total soot mass development during the premixed burn phase.

2.7.2. Soot Gradient. The soot gradient is defined as the soot mass per unit length along the spray axis, as illustrated in Figure 5. This is calculated from the cross-sectionally integrated KL distribution.

As seen in Figure 5, the liquid core overlaps with the soot-producing region of the spray, making this region ambiguous. To eliminate the liquid core from the integrated KL, the liquid core is estimated by fitting a Gaussian profile to the upstream part of the spray, where no soot is expected to form. The downstream part of the liquid core is then estimated based on the upstream line fit. This

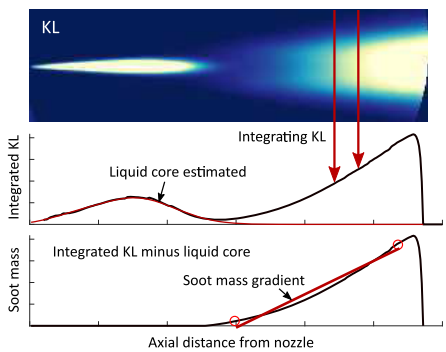

Figure 5. Illustration of how the soot gradient is calculated. Top: KL distribution; middle: cross-sectionally integrated KL values along the spray axis, estimated liquid core contribution is displayed in red; bottom: the resulting soot mass distribution after subtracting the liquid core from the integrated KL.

DOI: 10.1021/acs.energyfuels.9b01467
Energy Fuels 2019, 33, 7886−7900

procedure was verified by applying the same algorithm to a liquid core prior to the formation of soot, resulting in a good prediction of the downstream part of the liquid core. The *KL* distribution from the liquid core was then subtracted from the integrated *KL*, resulting in the integrated *KL* caused only by the presence of soot. By applying eq 7 to the integrated *KL*, the soot mass distribution along the spray axis was calculated. The soot gradient was calculated as the slope of a linear fit to the soot mass distribution along the spray axis in μg/cm.

The soot gradient gives a direct measure of the soot production tendency in the quasi-steady spray flame. Most of the soot is produced in the central core of the flame where there is a constant competition between soot formation and soot oxidation processes. After the flame lift-off location, soot formation processes dominate over soot oxidation, resulting in an increase of the soot concentration when moving downstream. At a certain point, soot oxidation overtakes soot formation, and the peak soot level is reached. Further downstream, oxidation is dominant and the soot level decays. The soot gradient observed between soot lift-off length position and peak soot position gives a measure of the imbalance between soot oxidation and soot formation.

2.8. Temporal Analysis of Soot and FLOL. To investigate the instantaneous effect of FLOL on in-flame soot, the FLOL was also determined temporally. This was achieved by plotting the OH* chemiluminescence along the central spray axis temporally (see Figure 6). The *x* axis is time after start of injection (ASOI), while *y* axis is the distance from the nozzle hole along the central spray axis, giving a temporal overview of the FLOL behavior. This type of plot is also known as an *I*−*x*−*t* plot, displaying an intensity distribution in the axial position/time plane. An interesting feature that can be observed in the plots is the tilted streaks, which displays the convection of turbulent structures along the central axis. Assuming that the turbulent structures follow the spray bulk motion, this provides an estimation of the spray velocity. This information will be used in the interpretation of the interaction between soot production and equivalence ratio at flame lift-off location.

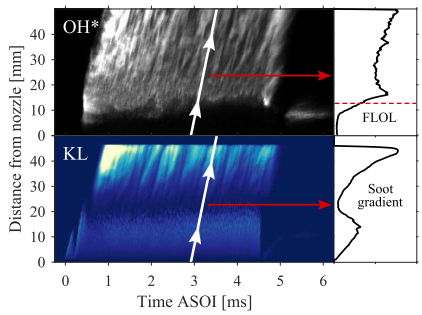

Figure 6. Temporal representation of cross-sectionally integrated *KL* and OH* along the spray axis. The line plots on the right-hand side represent the values along the "tilted" white lines. Values along the white line represent the trajectory of a gas parcel traveling in the spray. Lighter color means higher values of OH* and integrated *KL*.

Similar to the temporal development of the OH*, a temporal representation of soot is given. However, instead of taking the values along the spray central axis, the cross-sectionally integrated *KL* values are calculated. In this way, the total soot mass in each pixel-wide slice volume of the spray is plotted along the *y* axis of Figure 6, resulting in the temporal development of the axial distribution of soot mass in the reacting spray.

Due to the highly transient behavior of the FLOL, the amount of air mixed in with the spray prior to FLOL varies accordingly. This transient behavior translates into a fluctuating in-flame soot production, where a gas parcel traveling from the flame lift-off location with a certain equivalence ratio will have a soot production accordingly as it moves downstream. To relate the instantaneous equivalence ratio at FLOL to the corresponding soot production, values along a tilted line in Figure 6 are extracted. The line is tilted according to the estimated spray velocity, as mentioned previously. This results in extracting information from a gas parcel traveling along the spray axis. The calculated soot gradient and the FLOL are based on the average of 10 consecutive trajectories (tilted lines). This method was found to give more correlating results with regard to the relation between $\overline{\phi}(H)$ and the soot production. By comparing the temporal soot gradient to the corresponding equivalence ratio at the FLOL, the interaction between air entrainment and soot production for all of the fuels and conditions can be assessed, eliminating the uncertainty resulting from having an unsteady FLOL.

3. RESULTS AND DISCUSSION

3.1. Combustion Characteristics. In this section, combustion characteristics are presented. This includes the calculated apparent heat release rate (aHRR) and IDTs.

The aHRR was calculated from the in-cylinder combustion pressure based on a first-law approach described by Heywood,[47] and is shown in Figure 7 (top row). The bottom row of Figure 7 shows the sum of all pixel values captured by the OH* chemiluminescence high-speed measurement, where the OH*-based IDT is defined as the time between start of injection and the first observed OH* signal.

The aHRR curves of all fuels have similar characteristics. When considering each condition separately, ignition starts at similar timings and a premixed burn phase is evident for all fuels. The magnitude of the premixed burn phase is correlated with the IDTs; for a longer IDT, a larger heat release rate is observed. This is due to having a longer period for fuel and air to mix prior to ignition, leading to a larger portion of the injected fuel to burn as a premixed flame. After the premixed burn phase, the mixing-controlled burn phase occurs. This phase is unaffected by the IDT and seen to be very similar in magnitude and shape for all fuels and conditions. This phase will from here on be referred to as the quasi-steady period.

The IDTs are expected to follow the cetane number rating of the fuels. In general, longer chain lengths and a lower degree of unsaturation result in higher cetane numbers.[26] As seen in Table 4, two cetane numbers are given: cetane number and derived cetane number (DCN). The trends of the two are slightly different. When considering the cetane number, RME, MO, and heptane have similar values of ∼57, while MD has the lowest value of ∼48. This suggests that RME, MO, and heptane should have the shortest IDTs. As seen in Figure 8, this is not the case in the current study, where RME and MO have similar IDTs, and MD and heptane have longer IDTs.

When considering the DCNs of the fuels, the results are more correlated, MD and heptane have DCNs of 51.6 and 53, respectively, while RME and MO have ∼59. The reason for the DCNs being more correlated to the current results is likely due to the different operating conditions used when determining the DCN with the IQT and the cetane number with the CFR engine. With the device IQT, a single ambient gas condition is chosen, while the CFR engine uses a range. Because of the poorer low-temperature ignition properties of MD,[10] a lower cetane number is measured compared to heptane. The DCN is therefore more representative of the conditions used in the current study.

3.2. Flame Lift-Off Length. The FLOLs for all fuels and conditions were determined from the OH* chemiluminescence images. A sample size of 30 combustion cycles was used to get a representative mean. Figure 9 shows the mean

DOI: 10.1021/acs.energyfuels.9b01467
Energy Fuels 2019, 33, 7886−7900

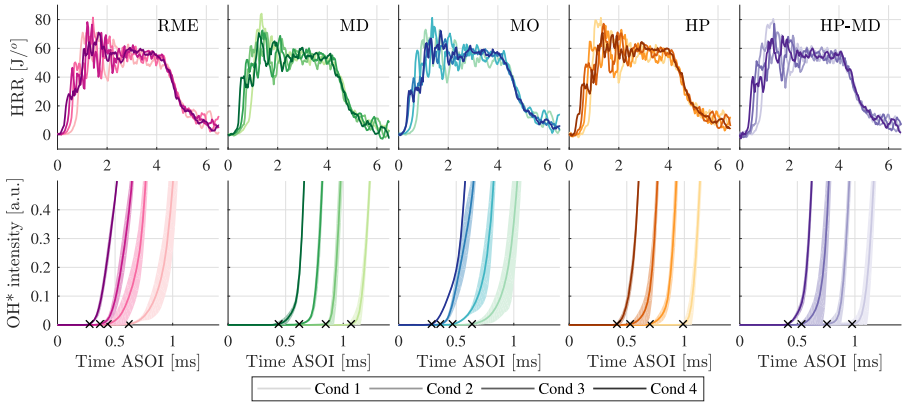

Figure 7. Apparent heat release rate (top row) and the total OH* chemiluminescence intensity for all fuels and conditions tested (bottom row). The occurrence of first OH* chemiluminescence signal is indicated by a cross. The HRR and OH* intensities shown are ensemble-averaged, and the bands indicate the ±1 standard deviation.

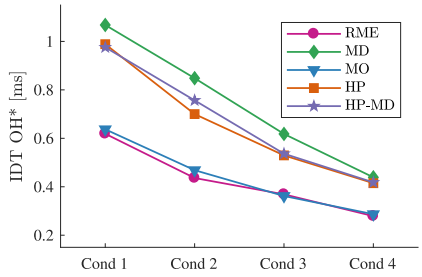

Figure 8. OH*-based IDTs determined from the first occurrence of the ensemble-averaged OH* signal.

temporal behavior of the FLOL plotted together with a ±1 standard deviation band to indicate the uncertainty. The FLOL has a tendency of starting with larger values, especially for the lower ambient temperature conditions, and stabilizing at a shorter distance later in the cycle. A possible contributor to this could be colder ambient gas temperatures before combustion. As combustion occurs, the ambient gases are further compressed by the combustion pressure rise, increasing the temperature. This is also likely to be the cause of the unstable lift-off length seen in the chamber since the combustion process is a highly stochastic event. This effect is much stronger in a small-volume combustion chamber such as the current one while less evident in a typical constant-volume combustion chamber, where the chamber volume is much larger. The FLOL stabilizes between 3 and 4 ms ASOI, which is also used as the quasi-steady period of the combustion period. Toward the end of the period, the FLOL was observed to increase slightly. This might be due to the ambient gas temperature decrease in the expansion stroke (see Figure 2). For MD during the coldest condition, the FLOL did not stabilize before ∼1.5 ms ASOI.

The average values of the FLOL during the quasi-steady period for all conditions and fuels are shown in Figure 10. All fuels show a monotonically decreasing trend with increasing ambient gas temperatures. RME has the shortest FLOL for all conditions, followed by MO. The short-chain molecule group of HP, MD, and HP−MD has quite similar FLOLs for all conditions, except the coldest one, where MD has a longer average FLOL. The FLOL has in some cases been shown to correlate closely with the cetane number,[48] although this is not always true, especially for oxygenated fuels,[10] where the fuel-

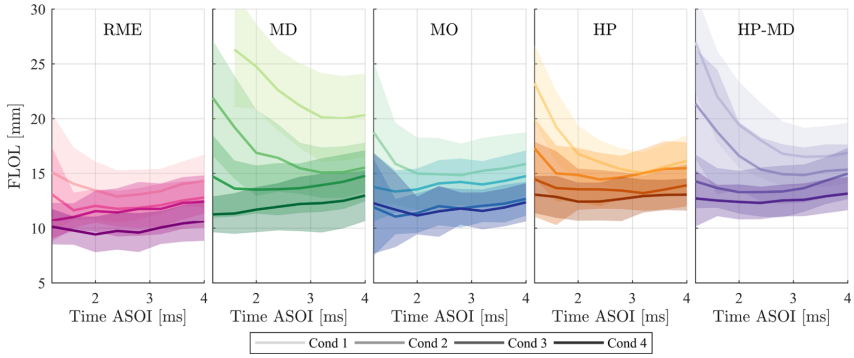

Figure 9. Ensemble-averaged temporal development of the flame lift-off length, including the ±1 standard deviation.

DOI: 10.1021/acs.energyfuels.9b01467
Energy Fuels 2019, 33, 7886−7900

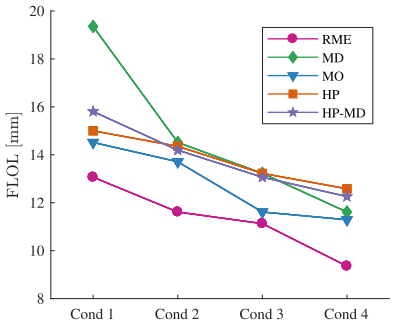

Figure 10. Average FLOLs during the quasi-steady period.

bound oxygen can affect the laminar flame speed and the location of the stoichiometric mixture fraction contour. When comparing the FLOL with the measured OH*-based IDTs, a clear correlation can be made (see Figure 11). For shorter

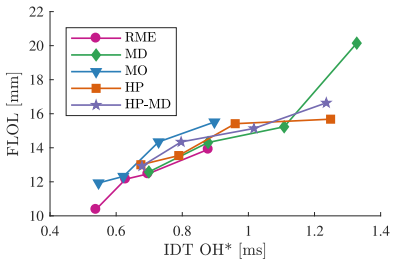

Figure 11. Comparison between OH*-based IDT and FLOL.

IDTs, shorter FLOLs are observed and vice versa. However, MD can be seen to deviate from the correlation for the coldest condition, where the FLOL is longer than what the trend would suggest.

3.3. Sooting Characteristics. *3.3.1. Ensemble-Averaged KL.* Ensemble-averaged *KL* images for all fuels and conditions tested are shown in Figure 12. The individual steady images are constructed from a total of 2730 images taken during the quasi-steady period.

As seen in Figure 12, all turbulent structures in the spray are averaged out, displaying only the mean behavior. The liquid core of the spray can be seen, where the trend of the liquid length closely follows the inverse of the volatility of the fuels, i.e., RME > MO > MD > HP−MD > HP. Downstream of the liquid core, soot is observed. The amount of soot produced in the spray increases when moving downstream. As mentioned previously, the peak soot level is located outside the measurement domain and therefore not captured in these measurements.

Looking at each fuel individually, the liquid length can be seen to decrease as ambient gas temperature increases. This is due to the hotter ambient gas vaporizing the liquid droplets faster. It is also clear that soot production in the spray flame increases as the ambient gas temperature increases. This is a consequence of the equivalence ratio at flame lift-off location, which was presented in the previous section. A higher ambient gas temperature results in a shorter FLOL, and consequently less air is entrained into the spray upstream of the FLOL. As the fuel-rich mixture has enough residence time, ignition starts and products are formed. A richer mixture prior to ignition leads to production of more soot precursors downstream of FLOL, such as polycyclic aromatic hydrocarbons, benzene, and acetylene.[49] From the gaseous soot precursors, soot nuclei are formed and surface growth and agglomeration occur, resulting in a large enough concentration of soot particles to be captured by the measurement technique.

Soot production in a turbulent nonpremixed flame is mainly governed by air entrainment upstream of FLOL and fuel effects. To investigate the fuel effects on soot production, Figure 13 shows the soot gradient from the steady *KL* measurement plotted against the equivalence ratio at FLOL ($\bar{\phi}(H)$). In this plot, one can compare the soot production in the flame for constant equivalence ratios at FLOL, and fuel effects can be singled out. The results show that MD has the lowest soot production, while the longer-chain esters have the highest. Heptane has a slightly lower soot production than the long-chain esters. For all equivalence ratios estimated, the

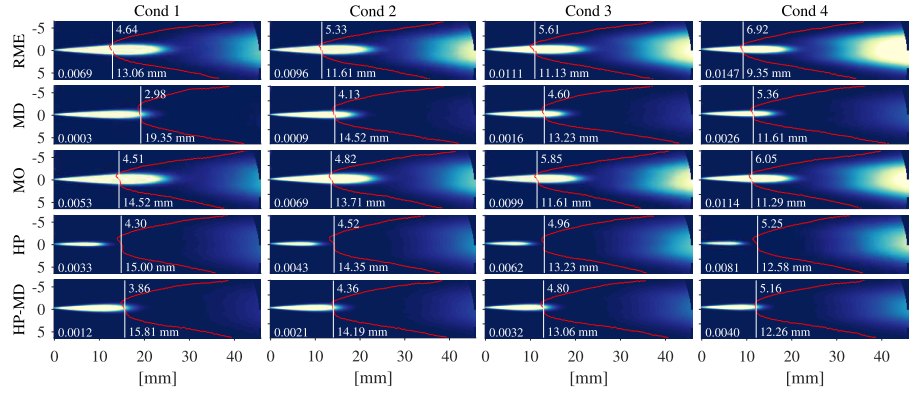

Figure 12. Ensemble-averaged *KL* plots, where the *KL* scale ranges from 0 to 1.4. The white line indicates the FLOL. The red contour indicates the location of the 50% OH* shoulder value. The soot gradient in μg/cm is indicated in the bottom left corner, the equivalence ratio at FLOL is indicated in the top middle, and the FLOL in mm is indicated in the bottom middle.

DOI: 10.1021/acs.energyfuels.9b01467
Energy Fuels 2019, 33, 7886−7900

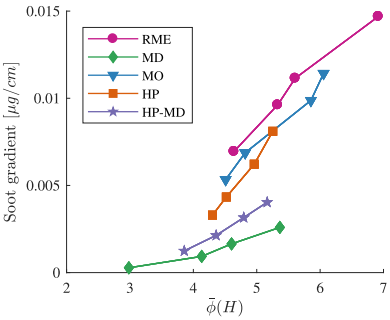

Figure 13. Equivalence ratio at FLOL plotted against soot gradient from the ensemble-averaged data.

ordering of soot production is RME > MO > HP > HP−MD > MD. Fuel effects on soot production will be discussed later in this section.

3.3.2. Temporal Distribution of OH Chemiluminescence and KL.* The temporal development of the OH* chemiluminescence and *KL* during the premixed burn phase for the hottest condition are discussed. Figure 14 shows the temporally ensemble-averaged measurement for the time interval 0.08−0.48 ms after start of OH* ignition. Each image is an average of 30 measurements.

In Figure 14, ignition starts for all fuels close to the nozzle tip. For RME and MO, the ignition starts closer to the nozzle than for the other fuels, which is likely due to the later ignition of the short-chain fuels, resulting in the igniting part of the fuel−air mixture to move further downstream for the short-chain fuels compared to the long-chain fuels. The initial ignition kernel close to the nozzle tip observed here is different from that observed in constant-volume vessels,[48] where ignition starts at or downstream of the stabilized flame lift-off location. The observed upstream ignition kernel is likely caused by injector specifics. The spray penetration velocity is observed to be slower in the beginning and increasing later on. This results in some fuel being present closer to the nozzle, igniting upstream of the stabilized FLOL. This will of course affect the premixed phase and must be taken into account when compared to simulations. For the long-chain fuels, the initial flame propagates from the near-nozzle ignition kernel to the tip of the spray, while for the short-chain fuels, a new ignition kernel is formed in the downstream part of the spray around 0.6−0.7 ms ASOI, where fuel and air have had time to form a premixed mixture. The two ignition kernels are later joined together, resulting in having similar characteristics to the long-chain fuels. This is also observed in the aHRR in Figure 7, where the short-chain fuels have higher heat release rate during the premixed burn phase than the long-chain fuels.

RME and MO have very similar temporal OH* characteristics, which is expected since RME consists of 61.8 wt % MO. MD and heptane also have relatively similar temporal OH* characteristics, which is more surprising, given that the molecular structures of the two fuels are very different.

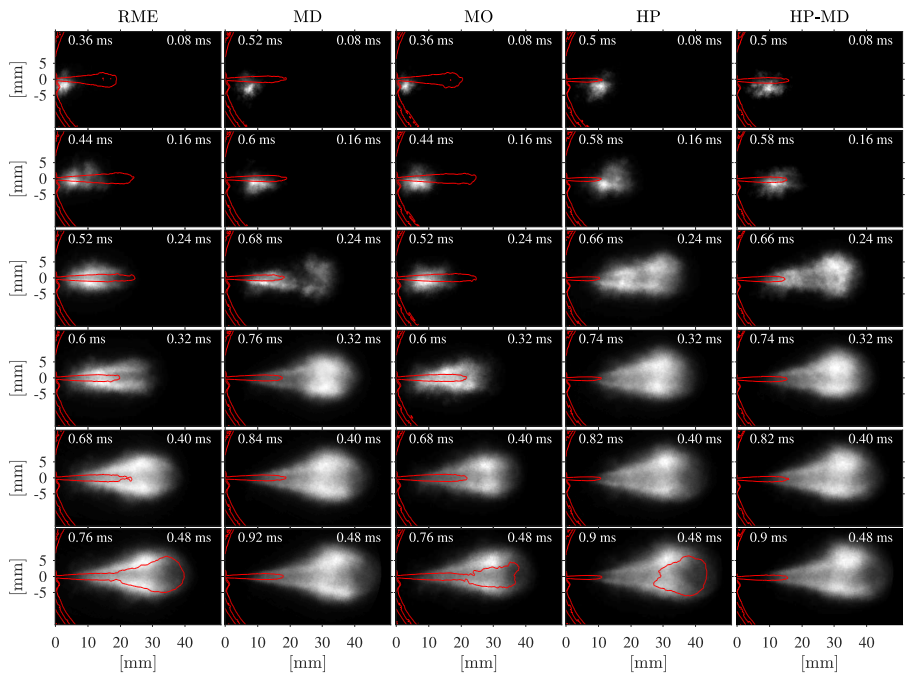

Figure 14. Ensemble-averaged plots showing the temporal development of OH* chemiluminescence during the premixed burn phase for the highest ambient gas temperature condition. The red line indicates the contour of the *KL* measurement. The indicated time on the left is time ASOI and the time on the right is time after start of ignition by OH*.

DOI: 10.1021/acs.energyfuels.9b01467
Energy Fuels 2019, 33, 7886−7900

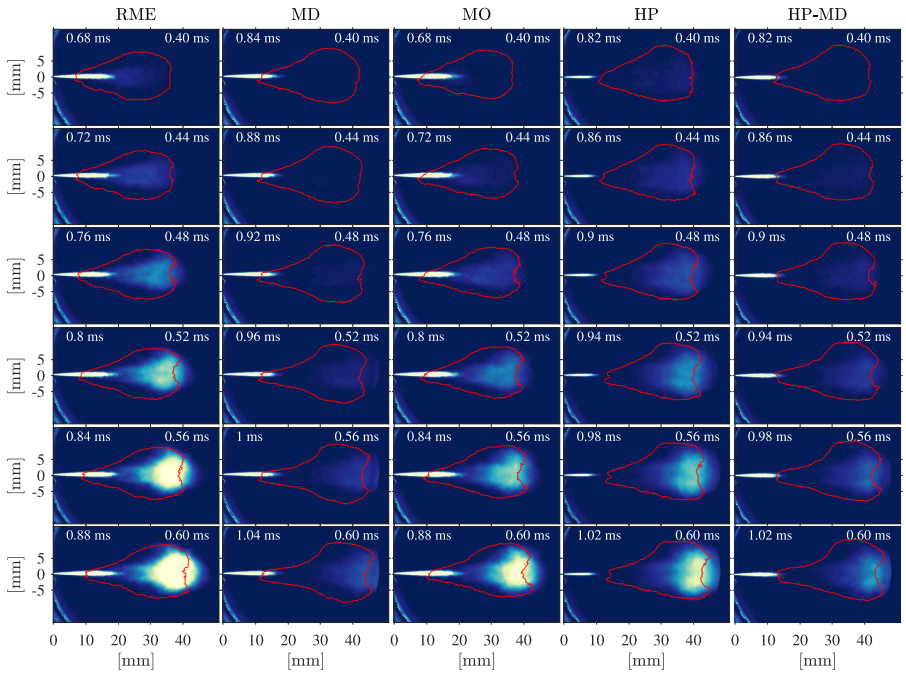

Figure 15. Ensemble-averaged plots showing the temporal development of *KL* during the premixed burn phase for the highest ambient gas temperature condition. The red line indicates the contour of the OH* chemiluminescence measurement. The indicated time on the left is time ASOI, and the time on the right is time after start of ignition by OH*.

However, the DCN of the two are similar, suggesting that the ignition properties should be similar.

Figure 15 shows the temporal development of *KL* for the time interval 0.4−0.6 ms after start of OH* ignition. Figure 16 shows the time after OH* ignition at which maximum soot production rate occurs together with the time of inception of soot. As seen in Figure 16, soot starts to form around 0.3 and 0.4 ms after start of OH* ignition for the hottest condition, meaning that Figure 15 shows the approximate start of soot production in the first row and the time of maximum soot mass rate in the last row. A general characteristic of the temporal development of soot production in the flame is that the highest soot production rate is found in the head of the spray. For the long-chain fuels, soot is first formed close to the end of the liquid core. For the short-chain fuels, soot is first formed further downstream. This due to the longer IDT of the short-chain fuel, where the spray flame has had time to develop before soot starts to form. Fuel volatility also has an impact on the initial premixing and the IDT, where the short-chain fuels, having higher volatility, evaporate faster, resulting in shortening of the IDT.

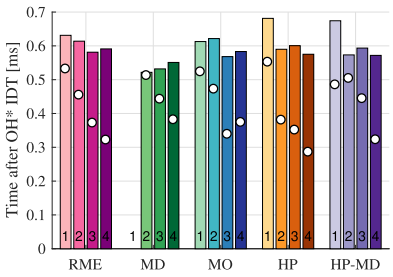

Figure 16. Time between OH*-based ignition and maximum production rate of soot. The time of inception of soot is indicated as white circles, and the numbers at the bottom indicate the condition. No soot was detected for MD at condition 1.

For increasing ambient gas temperatures in Figure 16, the time of soot inception is advanced, while the time of maximum soot production is held relatively stable, especially for the three hottest conditions. This indicates that an increase in ambient gas temperature decreases the time for the first detectable soot particles to form. The time between OH* ignition and maximum soot rate occurrence is relatively unaffected by the temperature increase. The maximum soot production rate for all fuels and conditions are shown in Figure 17. The data for conditions 3 and 4 are most representative of the total soot produced because of the early ignition resulting in the initial soot being produced within the measurement domain. The maximum soot production rate increases for higher ambient gas temperatures and has the same ordering as the soot gradient during quasi-steady period, i.e., RME > MO > HP > HP−MD > MD.

3.3.3. Instantaneous Soot Production and Local Equivalence Ratio. An analysis of the instantaneous $\overline{\phi}(H)$ and the instantaneous soot gradient was performed based on their temporal development and is shown in Figure 18. In these plots, the instantaneous equivalence ratio at FLOL and the

DOI: 10.1021/acs.energyfuels.9b01467
Energy Fuels 2019, 33, 7886−7900

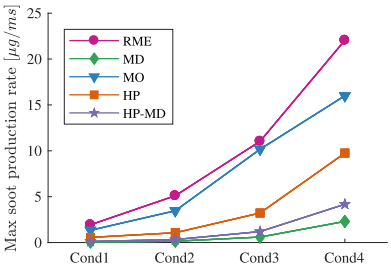

Figure 17. Maximum soot production rate.

corresponding soot gradient are plotted temporally over the combustion period. This approach minimizes the effects of an unstable FLOL on the soot production since temporal effects are captured. Each point in Figure 18 represents an instantaneous measurement during an injection event, not considering the early and late phases of the combustion period, approximately between 1 and 4 ms ASOI. The plots on top and to the right of each figure indicate the number density of the points along their respective axes, showing each condition separately. From this, the spread in the results of measured $\overline{\phi}(H)$ and soot gradient is observed. The $\overline{\phi}(H)$ and the soot gradient have a relatively large spread, indicating that the combustion is highly stochastic. However, the $\overline{\phi}(H)$ and the soot gradient correlate quite well, even within a single condition, where a low equivalence ratio at FLOL leads to a lower soot gradient and vice versa.

For equivalence ratio values below approximately 2, no soot is expected to be formed, as concluded by Pickett and Siebers,[15] which can be observed in the current measurements. All fuels start forming soot between approximately $\overline{\phi}(H) = 2$ and 2.5. As seen in eq 5, the fuel-bound oxygen is taken into account when calculating $\overline{\phi}(H)$, making Figure 18 mostly dependent on fuel molecular and ambient gas temperature differences.

An interesting observation can be seen when investigating the scatter plot for an individual fuel. If the soot gradient was independent of the ambient gas temperature increase between the conditions, the condition-wise trend lines of the points would be expected to overlap each other as the equivalence ratio increased. However, when calculating a least-squares linear fit for each condition, the lines for each condition do not line up. This means that for the same equivalence ratio, the soot gradient increases for increasing ambient gas temperatures, indicating that there is a clear effect of temperature on soot production for all fuels. This was also observed in refs 41 and 50.

3.3.4. Discussion on Fuel Effects on Soot Production. The difference in soot production between RME and MO is interesting since these two fuels are very similar in composition. In Table 4, the main difference between RME and MO is the degree of unsaturation. RME has a 10% higher degree of unsaturation compared to MO. The degree of unsaturation in esters has been shown in several studies to increase the sooting tendency of a nonpremixed flame.[22,51,52] The higher degree of unsaturation in the RME can then likely explain the higher soot production seen in these measurements.

When comparing the properties of MD and heptane, many differences can be pointed out. MD has a higher number of C−C bonds and a higher degree of unsaturation, which both promotes the production of soot precursors. In addition, MD has an ester moiety and a high content of oxygen in the molecule, which previously has shown to reduce soot production compared to similar-chain-length alkanes.[52] Since a lower soot production is observed in the measurements, it is evident that the presence of the ester functional group and the fuel-bound oxygen in MD are the dominating effects in the reduction of soot production.

The 50% molar blend of heptane and MD (HP−MD) resulted in a soot production that was in between heptane and MD. This is expected since the properties determining the soot

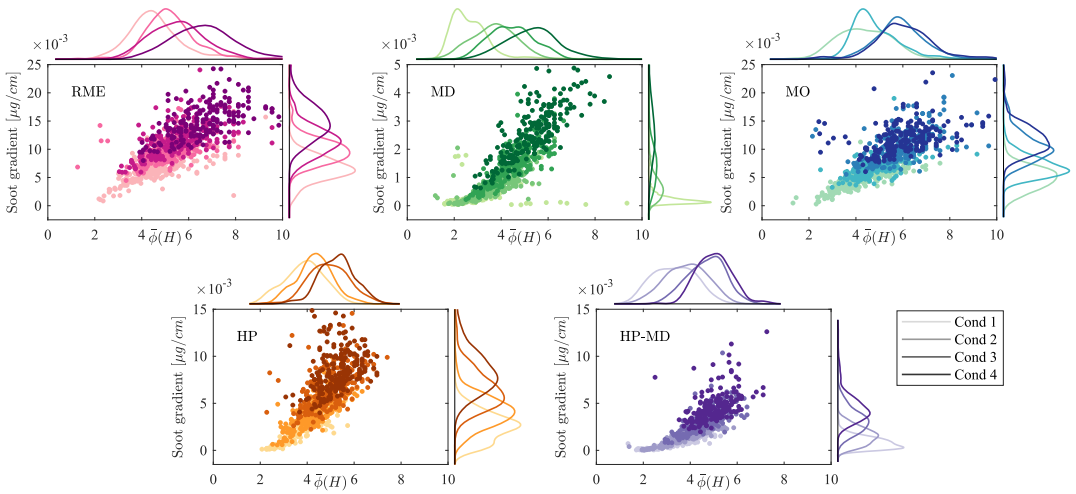

Figure 18. Instantaneous soot gradient versus equivalence ratio plots. The plots on top and to the right of each figure indicate the number density of the points along their respective axes, showing each condition separately.

DOI: 10.1021/acs.energyfuels.9b01467
Energy Fuels 2019, 33, 7886−7900

production are based on molecular properties; the 50% molar blend yields the mean of the important properties listed above.

Temperature effects on the soot gradient in Figure 13 must be taken into account when comparing the fuels. For instance, when considering soot gradients for all fuels at $\overline{\phi}(H) = 4.5$, the ambient gas temperatures for each fuel at this equivalence ratio are different since the points for each fuel in the plot represent different conditions. At $\overline{\phi}(H) = 4.5$, MD is close to condition 3, heptane is close to condition 2, and RME/MO are close to condition 1. This temperature effect can, however, be eliminated by plotting the individual conditions separately, shown in Figure 19 for condition 4. The variation of the

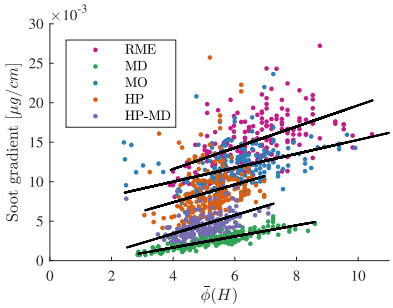

Figure 19. Instantaneous $\overline{\phi}(H)$ and the soot gradient for the hottest condition; the lines show the least-squares linear fit of the individual fuels.

equivalence ratio is here only due to the change in FLOL under the same ambient gas temperature, showing that the temperature effect on soot production does not change the soot gradient ordering for a given equivalence ratio.

4. CONCLUSIONS

Detailed measurements of in-flame soot and FLOL of compression-ignited flames of fuels relevant for biodiesel combustion have been conducted. The main conclusions are listed below.

- The fuels can be split into two groups: short- and long-carbon-chain fuels. The long-chain fuels, i.e., RME and neat MO, were observed to have shorter IDTs compared to the short-chain fuels (MD and heptane). Consequently, a higher heat release rate during the premixed combustion phase was observed for the short-chain fuels, due to more premixing prior to start of ignition.
- The FLOL correlated well with the ignition properties of all fuels, except for methyl decanoate, for the coldest condition, where the FLOL was found to deviate from the general trend.
- For a constant equivalence ratio at the flame lift-off location, the order of in-flame soot production was found to be RME > MO > HP > HP−MD > MD. The higher sooting tendency of RME compared to MO is likely due to the higher degree of unsaturation, while the lower sooting tendency of MD compared to heptane was mainly attributed to the high fuel oxygen ratio.
- Extrapolating the in-flame soot production for equivalence ratios at FLOL leaner than 2−2.5 yielded sootless combustion for all fuels tested.
- The instantaneous soot production in the spray and the corresponding equivalence ratio at FLOL correlated well within each individual combustion period, supporting the argument of air entrainment prior to FLOL being a very important factor for in-flame soot production.
- From analyzing the instantaneous soot production gradient versus instantaneous equivalence ratio at flame lift-off location over individual injection events, a clear temperature dependence on the balance between soot formation and oxidation was observed. Flames combusting with higher ambient gas temperatures with the same equivalence ratio at FLOL have higher soot production, meaning that the soot formation rate increases more than the soot oxidation rate for elevated temperatures within the tested temperature range.
- During the premixed combustion phase, soot mass production rate was measured, seeing that the soot mass rate increases substantially as ambient gas temperature is increased. This was likely attributed to the higher equivalence ratio in the fuel−air mixture for the hotter conditions because of shorter IDTs.
- The IDT between RME and MO was found to be very similar for all conditions, suggesting that the equivalence ratio in the fuel−air mixture prior to the premixed combustion phase was very similar. The ∼33% higher maximum soot production rate of RME compared to MO therefore supports the finding of the RME having a higher sooting tendency.
- The time between start of ignition and onset of soot was found to decrease as ambient gas temperature increased. For the three hottest conditions, the time between start of ignition and occurrence of maximum soot mass rate was almost constant for all fuels except for MD. This indicated that the time between onset of soot and occurrence of maximum soot mass rate increases as temperature increases.

AUTHOR INFORMATION

Corresponding Author

*E-mail: karl.o.bjorgen@ntnu.no. Phone: +47 90861780.

ORCID

Karl Oskar Pires Bjørgen: 0000-0003-2751-8670

David Robert Emberson: 0000-0002-0458-9356

Notes

The authors declare no competing financial interest.

ACKNOWLEDGMENTS

The experiments were conducted in the Motorlab at the Norwegian University of Science and Technology in Trondheim, Norway. The laboratory was supported by the research center Bio4fuels, which is part of Centers for Environment-friendly Energy Research (FME) funded by the Norwegian Research Council.

REFERENCES

(1) Skeen, S. A.; et al. A Progress Review on Soot Experiments and Modeling in the Engine Combustion Network (ECN). *SAE Int. J. Engines* **2016**, *9*, 883−898.

(2) International Energy Agency. *Renewables 2018*; IEA, 2018.

(3) Omidvarborna, H.; Kumar, A.; Kim, D.-S. Recent Studies on Soot Modeling for Diesel Combustion. *Renewable Sustainable Energy Rev.* **2015**, *48*, 635−647.

DOI: 10.1021/acs.energyfuels.9b01467
Energy Fuels 2019, 33, 7886−7900

(4) Fisher, E.; Pitz, W.; Curran, H.; Westbrook, C. Detailed Chemical Kinetic Mechanisms for Combustion of Oxygenated Fuels. *Proc. Combust. Inst.* **2000**, *28*, 1579−1586.
(5) Vaughn, T.; Hammill, M.; Harris, M.; Marchese, A. J. *Ignition Delay of Bio-Ester Fuel Droplets*; SAE Technical Paper Series; SAE International, 2006.
(6) Herbinet, O.; Pitz, W. J.; Westbrook, C. K. Detailed Chemical Kinetic Oxidation Mechanism for a Biodiesel Surrogate. *Combust. Flame* **2008**, *154*, 507−528.
(7) Herbinet, O.; Pitz, W. J.; Westbrook, C. K. Detailed Chemical Kinetic Mechanism for the Oxidation of Biodiesel Fuels Blend Surrogate. *Combust. Flame* **2010**, *157*, 893−908.
(8) Dagaut, P.; Gaïl, S.; Sahasrabudhe, M. Rapeseed Oil Methyl Ester Oxidation Over Extended Ranges of Pressure, Temperature, and Equivalence Ratio: Experimental and Modeling Kinetic Study. *Proc. Combust. Inst.* **2007**, *31*, 2955−2961.
(9) Westbrook, C.; Naik, C.; Herbinet, O.; Pitz, W.; Mehl, M.; Sarathy, S.; Curran, H. Detailed Chemical Kinetic Reaction Mechanisms for Soy and Rapeseed Biodiesel Fuels. *Combust. Flame* **2011**, *158*, 742−755.
(10) Manin, J.; Skeen, S.; Pickett, L.; Kurtz, E.; Anderson, J. E. Effects of Oxygenated Fuels on Combustion and Soot Formation/Oxidation Processes. *SAE Int. J. Fuels Lubr.* **2014**, *7*, 704−717.
(11) Cheng, A. S. E.; Dumitrescu, C. E.; Mueller, C. J. Investigation of Methyl Decanoate Combustion in an Optical Direct-Injection Diesel Engine. *Energy Fuels* **2014**, *28*, 7689−7700.
(12) Dumitrescu, C. E.; Cheng, A. S.; Kurtz, E.; Mueller, C. J. A Comparison of Methyl Decanoate and Tripropylene Glycol Monomethyl Ether for Soot-Free Combustion in an Optical Direct-Injection Diesel Engine. *J. Energy Resour. Technol.* **2017**, *139*, No. 042210.
(13) Le, M. K.; Zhang, R.; Rao, L.; Kook, S.; Hawkes, E. R. The Development of Hydroxyl and Soot in a Methyl Decanoate-Fuelled Automotive-Size Optical Diesel Engine. *Fuel* **2016**, *166*, 320−332.
(14) Su, H. C.; Kook, S.; Chan, Q. N.; Hawkes, E. R.; Le, M. K.; Ikeda, Y. A Comparison of High-Temperature Reaction and Soot Processes of Conventional Diesel and Methyl Decanoate. *Fuel* **2018**, *226*, 635−643.
(15) Pickett, L. M.; Siebers, D. L. *Non-Sooting, Low Flame Temperature Mixing-Controlled DI Diesel Combustion*; SAE Technical Paper Series; SAE International, 2004.
(16) Pickett, L. M.; Siebers, D. L. *Fuel Effects on Soot Processes of Fuel Jets at DI Diesel Conditions*; SAE Technical Paper Series; SAE International, 2003.
(17) Park, W.; Park, S.; Reitz, R. D.; Kurtz, E. The Effect of Oxygenated Fuel Properties on Diesel Spray Combustion and Soot Formation. *Combust. Flame* **2017**, *180*, 276−283.
(18) Zhang, R.; Pham, P. X.; Kook, S.; Masri, A. R. Influence of Biodiesel Carbon Chain Length on in-Cylinder Soot Processes in a Small Bore Optical Diesel Engine. *Fuel* **2019**, *235*, 1184−1194.
(19) Woschni, G. A. *A Universally Applicable Equation for the Instantaneous Heat Transfer Coefficient in the Internal Combustion Engine*; SAE Technical Paper Series; SAE International, 1967.
(20) Knothe, G. Dependence of Biodiesel Fuel Properties on the Structure of Fatty Acid Alkyl Esters. *Fuel Process. Technol.* **2005**, *86*, 1059−1070.
(21) Mueller, C. J.; Pitz, W. J.; Pickett, L. M.; Martin, G. C.; Siebers, D. L.; Westbrook, C. K. *Effects of Oxygenates on Soot Processes in DI Diesel Engines: Experiments and Numerical Simulations*; SAE Technical Paper Series; SAE International, 2003.
(22) Sarathy, S.; Gail, S.; Syed, S.; Thomson, M.; Dagaut, P. A Comparison of Saturated and Unsaturated C4 Fatty Acid Methyl Esters in an Opposed Flow Diffusion Flame and a Jet Stirred Reactor. *Proc. Combust. Inst.* **2007**, *31*, 1015−1022.
(23) Yuan, W.; Hansen, A.; Zhang, Q. Vapor Pressure and Normal Boiling Point Predictions for Pure Methyl Esters and Biodiesel Fuels. *Fuel* **2005**, *84*, 943−950.
(24) Knothe, G. A Comprehensive Evaluation of the Cetane Numbers of Fatty Acid Methyl Esters. *Fuel* **2014**, *119*, 6−13.
(25) Murphy, M. J.; Taylor, J. D.; McCormick, R. L. *Compendium of Experimental Cetane Number Data*; National Renewable Energy Laboratory, 2004.
(26) Knothe, G., Krahl, J., Van Gerpen, J. H., Eds. *The Biodiesel Handbook*, 2nd ed.; Elsevier: Urbana, IL, 2015.
(27) Knothe, G. "Designer" Biodiesel: Optimizing Fatty Ester Composition to Improve Fuel Properties. *Energy Fuels* **2008**, *22*, 1358−1364.
(28) Lemmon, E. W.; McLinden, M. O.; Friend, D. G. *NIST Chemistry WebBook*; NIST Standard Reference Database Number 69; NIST, 2018.
(29) Beattie, J. A.; Kay, W. C. The Normal Boiling Point and Critical Constants of Normal Heptane. *J. Am. Chem. Soc.* **1937**, *59*, 1586−1587.
(30) Yang, C.; Xu, W.; Ma, P. Thermodynamic Properties of Binary Mixtures of *p*-Xylene with Cyclohexane, Heptane, Octane, and *N*-Methyl-2-pyrrolidone at Several Temperatures. *J. Chem. Eng. Data* **2004**, *49*, 1794−1801.
(31) Knothe, G.; Matheaus, A. C.; Ryan, T. W., III Cetane Numbers of Branched and Straight-Chain Fatty Esters Determined in an Ignition Quality Tester Quality Tester. *Fuel* **2003**, 971−975.
(32) Lilik, G. K.; Boehman, A. L. Effects of Fuel Ignition Quality on Critical Equivalence Ratio for Autoignition. *Energy Fuels* **2013**, *27*, 1586−1600.
(33) Bohren, C. F.; Huffman, D. R. *Absorption and Scattering of Light by Small Particles*; John Wiley & Sons, 2008.
(34) Zhao, H.; Ladommatos, N. Optical Diagnostics for Soot and Temperature Measurement in Diesel Engines. *Prog. Energy Combust. Sci.* **1998**, *24*, 221−255.
(35) Skeen, S.; Yasutomi, K.; Cenker, E.; Adamson, B.; Hansen, N.; Pickett, L. Standardized Optical Constants for Soot Quantification in High-Pressure Sprays. *SAE Int. J. Engines* **2018**, *11*, 805−816.
(36) Bjørgen, K. O. P.; Emberson, D. R.; Lovas, T. *Diffuse Back-Illuminated Extinction Imaging of Soot: Effects of Beam Steering and Flame Luminosity*; SAE Technical Paper Series; SAE International, 2019.
(37) Pastor, J. V.; Garcia-Oliver, J. M.; Novella, R.; Xuan, T. Soot Quantification of Single-Hole Diesel Sprays by Means of Extinction Imaging. *SAE Int. J. Engines* **2015**, *8*, 2068−2077.
(38) Skeen, S. A.; Yasutomi, K. Measuring the Soot Onset Temperature in High-Pressure N-Dodecane Spray Pyrolysis. *Combust. Flame* **2018**, *188*, 483−487.
(39) Westlye, F. R.; Penney, K.; Ivarsson, A.; Pickett, L. M.; Manin, J.; Skeen, S. A. Diffuse Back-Illumination Setup for High Temporally Resolved Extinction Imaging. *Appl. Opt.* **2017**, *56*, 5028.
(40) Higgins, B.; Siebers, D. *Measurement of the Flame Lift-Off Location on Dl Diesel Sprays Using OH Chemiluminescence*; SAE Technical Paper Series; SAE International, 2001.
(41) Pickett, L. M.; Siebers, D. L. Soot in Diesel Fuel Jets: Effects of Ambient Temperature, Ambient Density, and Injection Pressure. *Combust. Flame* **2004**, 114.
(42) Naber, J.; Siebers, D. L. *Effects of Gas Density and Vaporization on Penetration and Dispersion of Diesel Sprays*; SAE Technical Paper Series; SAE International, 1996.
(43) Siebers, D. L. *Scaling Liquid-Phase Fuel Penetration in Diesel Sprays Based on Mixing-Limited Vaporization*; SAE Technical Paper Series; SAE International, 1999.
(44) Siebers, D. L.; Higgins, B.; Pickett, L. *Flame Lift-Off on Direct-Injection Diesel Fuel Jets: Oxygen Concentration Effects*; SAE Technical Paper Series; SAE International, 2002.
(45) Totton, T. S.; Chakrabarti, D.; Misquitta, A. J.; Sander, M.; Wales, D. J.; Kraft, M. Modelling the Internal Structure of Nascent Soot Particles. *Combust. Flame* **2010**, *157*, 909−914.
(46) Choi, M. Y.; Mulholland, G. W.; Hamins, A.; Kashiwagi, T. Comparisons of the Soot Volume Fraction Using Gravimetric and Light Extinction Techniques. *Combust. Flame* **1995**, *102*, 161−169.
(47) Heywood, J. B. *Internal Combustion Engine Fundamentals*; McGraw-Hill, 1988.

DOI: 10.1021/acs.energyfuels.9b01467
Energy Fuels 2019, 33, 7886−7900

(48) Pickett, L. M.; Siebers, D. L.; Idicheria, C. A. *Relationship Between Ignition Processes and the Lift-Off Length of Diesel Fuel Jets*; SAE Technical Paper Series; SAE International, 2005.
(49) Tree, D. R.; Svensson, K. I. Soot Processes in Compression Ignition Engines. *Prog. Energy Combust. Sci.* **2007**, *33*, 272−309.
(50) Kook, S.; Pickett, L. M. Effect of Fuel Volatility and Ignition Quality on Combustion and Soot Formation at Fixed Premixing Conditions. *SAE Int. J. Engines* **2009**, *2*, 11−23.
(51) Das, D. D.; McEnally, C. S.; Pfefferle, L. D. Sooting Tendencies of Unsaturated Esters in Nonpremixed Flames. *Combust. Flame* **2015**, *162*, 1489−1497.
(52) Kholghy, M. R.; Weingarten, J.; Sediako, A. D.; Barba, J.; Lapuerta, M.; Thomson, M. J. Structural Effects of Biodiesel on Soot Formation in a Laminar Coflow Diffusion Flame. *Proc. Combust. Inst.* **2017**, *36*, 1321−1328.

■ NOTE ADDED AFTER ASAP PUBLICATION

Due to a production error, this article published August 5, 2019 with errors in the values of Table 4. The corrected table published August 6, 2019.

DOI: 10.1021/acs.energyfuels.9b01467
Energy Fuels 2019, 33, 7886−7900

Article III

Karl Oskar Pires Bjørgen, David Robert Emberson and Terese Løvås

Combustion and Soot Characteristics of Hydrotreated Vegetable Oil Compression-Ignited Spray Flames

Submitted to Fuel 9.12.2019

The final article is published in Fuel 2020 ;Volum 266.
https://doi.org/10.1016/j.fuel.2019.116942

Combustion and Soot Characteristics of Hydrotreated Vegetable Oil Compression-Ignited Spray Flames

Karl Oskar Pires Bjørgen, David Robert Emberson, Terese Løvås

Department of Energy and Process Engineering,
Norwegian University of Science and Technology, Trondheim, Norway

Abstract

Quantitative measurements of combustion and in-flame soot in hydrotreated vegetable oil (HVO), biodiesel (rapeseed methyl ester [RME]) and diesel fuel spray flames are presented in this study. The measurements were performed in a compression ignition chamber with optical access having engine-like thermodynamic conditions. The simultaneously employed optical techniques were high-speed diffuse back-illuminated light extinction imaging for measuring the optical depth (KL) of in-flame soot, and OH^* chemiluminescence for imaging high temperature reaction zones. The results show that diesel produces a considerably higher amount of in-flame soot compared to RME and HVO, which is likely due to the aromatics present in diesel, while RME and HVO produce similar levels. RME was found to produce slightly less soot, which is likely due to the fuel-bound oxygen, since HVO and RME have a similar number of carbon-carbon bonds. The soot production during the premixed and mixing-controlled period were found to have similar trends. The time lag between start of ignition and soot formation was found to be constant for varying ambient temperatures for individual fuels, where soot was detected earliest after ignition for diesel, followed by HVO and RME, matching the measured sooting tendencies. The stabilised flame lift-off length of HVO was found to be shorter than that of diesel, while RME had the shortest of them all.

Keywords: soot; hydrotreated vegetable oil; spray combustion; compression-ignition; flame lift-off length

1. Introduction

Hydrotreated vegetable oil (HVO) has gained popularity over the past years because of its low carbon footprint while still having diesel-like fuel properties. The similarity in fuel properties makes HVO a so-called drop-in fuel, where no hardware modifications to a compression ignition (CI) engine are required. Since HVO is produced from renewable resources, it is often referred to as renewable diesel or green diesel. In contrast to its name, the feedstock HVO is produced from is not only limited to vegetable oil, but can also be made from other biomass sources such as fish and animal fats. Compared to diesel fuel, HVO is free from cycloalkanes and aromatics, yielding a lower sooting tendency. In addition, it consists of a mixture of normal and isoalkanes, resulting in a high cetane number, making it well suited for CI engines.

The production process of HVO starts with fatty oils (triglyceride). In the first step, the triglyceride is hydrotreated with hydrogen resulting in diglycerides, monoglycerides and acids [1]. The following step converts the intermediates into normal alkanes through decarboxylation, decarbonylation and hydrogenation. Some of the normal alkanes also under undergo isomerization and cracking, leading to isomerized and lighter alkanes in the product. This results in lowering the cetane number and the viscosity to more diesel-like properties.

HVO meets the European standard EN 15940 for paraffinic fuels, which also applies to synthetic fuels such as gas-to-liquid (GTL) and biomass-to-liquid (BTL) fuels (e.g. Fischer-Tropsch fuels). The EN 15940 standard is very similar to EN 590, which includes petroleum diesel and B7 (petroleum diesel containing maximum 7 vol-% fatty acid methyl ester [FAME]), however, EN 15940 has a minimum cetane number requirement of 70 versus 51 for EN 590, and a lower fuel density interval, 765-800 kg/m^3 versus 820-845 kg/m^3 for EN 590. Since HVO consists only of hydrocarbons, it is allowed to be blended in to an EN 590 fuel without labelling of any biocomponent at the retail point, as long as the regulations of EN 15940 are complied with. EN 590 does not have any requirements to the production process or the origin of the fuel, and can therefore contain HVO, in addition to the maximum allowed FAME content of 7 vol-%. The reason for regulating the FAME content, and not the HVO content, is due to the chemical composition of FAME (e.g. containing oxygen) [2].

HVO has shown to be a cleaner fuel when it comes to tail pipe emissions, reducing particulate matter (PM), NO_x, CO and total hydrocarbon emissions. Murtonen et al. [3] conducted an extensive study on emissions from five city buses and three engines running on diesel fuel (EN 590), FAME, GTL and HVO. The conclusion of this work was that PM was reduced by 30-51% when running on the paraffinic fuels (GTL and HVO) compared to diesel fuel. Similar reductions in PM emission when fuelling with HVO compared to diesel fuel has been observed in [4, 5, 6, 7].

Regarding macroscopic spray characteristics, those of HVO are found to be similar to diesel fuel since physical properties

like viscosity and distillation curve are similar. Bohl et al. [8] found that HVO has a slightly larger spray cone angle and a shorter spray penetration length than diesel fuel, which they explained was due to the lower density of HVO. The same conclusions were drawn by Cheng et al. [9], who also showed that the air-fuel mixing is similar for the two fuels.

For CI engines, the spray characteristics are of importance for understanding the tail-pipe emissions. In-flame soot measurements for HVO and diesel fuel were performed in a constant volume vessel by Zhang et al. [10]. The results showed that HVO and diesel fuel have very similar combustion characteristics, which include the flame lift-off length (FLOL), ignition delay time (IDT) and in-flame soot concentration. The previously mentioned engine experiments showed that HVO generally reduces the exhaust PM emissions compared to diesel fuel. However, the study by Zhang et al. did not show any reduction in in-flame soot. The in-flame soot is expected to be lower than that of diesel fuel, which was not shown in this study.

A detailed spray combustion study of a 50/50% blend by mass consisting of hydrogenated catalytic biodiesel (HCB)[1] and diesel fuel (not containing biodiesel) was performed by Xuan et al. [11]. The measurements were limited by the window size of the optical combustion chamber used, which resulted in not capturing the entire flame. The total soot mass was therefore affected by the FLOL, where the diesel/HCB blend had the shortest. This resulted in the measured soot area, i.e. the number of pixels containing soot in the measurement domain, being larger for diesel/HCB. Having measured that diesel/HCB had similar total soot mass levels compared to diesel, they concluded that HCB has a lower in-flame soot mass, since the soot area of diesel/HCB was larger.

Sooting tendencies calculated based on measured smoke point of diesel fuel, GTL, HVO and biodiesel were reported by Gómez et al. [12]. The study concluded that the order of sooting tendency was GTL<HVO<biodiesel<diesel, however, the difference between GTL, HVO and biodiesel was very small.

Finally it is worth noting that Lapuerta et al. [13] measured key properties relevant for CI combustion for blends of diesel and HVO. For an unmodified CI engine, they recommended not to blend HVO with diesel to above 50% by volume, as this would result in operational restrictions based on the low lubricity, the high cetane number and the poor cold flow properties of HVO. Also, sooting tendencies of HVO and diesel were measured, where the sooting tendency was dramatically reduced with an increased blending fraction of HVO.

As the future use of HVO in an engine will most likely be a blend of HVO, FAME and diesel, the three components are investigated in this study, where quantitative data on in-flame soot and spray combustion characteristics are measured and reported. Measurements of the three fuels in the same test rig, with the same measurement techniques, also enable a direct qualitative and quantitative comparison of the three fuels. The objective of this work is to generate detailed information about in-flame soot production of HVO, which will help researchers and industry understanding the underlying phenomena connected to soot characteristics of HVO, in comparison to diesel and FAME. To the authors' knowledge, this level of detail has not previously been reported in literature and is needed for validation of simulations.

[1] hydrogenated catalytic biodiesel is an alternative name of HVO.

2. Experimental Methods

2.1. Fuels

The fuels tested were HVO, diesel fuel (EN 590) and rapeseed methyl ester (RME) representing FAME. All tested fuels are commercially available in Norway. Important chemical and physical properties of all fuels are listed in Table 1. Since the molecular composition of HVO was not measured in this study, the composition measured by Zhong et al. [14] was used, as the fuel is similar to the one tested here. The tested diesel fuel is a Norwegian pump diesel, complying to EN 590.

There is a large difference between the cetane numbers of the fuels, where HVO has the highest of 93.2, while diesel has the lowest of 49.2. As mentioned, the density is the limiting property of HVO compared to diesel for satisfying the EN 590 standard, and in this case, HVO has a 8% lower density than diesel. The viscosity of HVO compared to diesel, although not conflicting with the EN 590 standard, is also much lower. When considering the sooting tendencies of the fuels, the aromatic content, the oxygen content, the number of carbon-carbon bonds and the degree of unsaturation are important. Note that HVO has a very low degree of unsaturation; 0.4 mol^{-1} compared to 1-2 mol^{-1} and 2.2 mol^{-1} for diesel and RME, respectively.

The distillation curve of all fuels were measured according to ASTM D86, which measures the boiling point of fuels at atmospheric pressure. The diesel fuel had a distillation curve linearly varying from $T_{b,10}$ = 480 K to $T_{b,90}$ = 615 K, having $T_{b,50}$ = 556 K. Both RME and HVO had relatively flat distillation curves where $T_{b,50}$ = 611 K for RME and $T_{b,50}$ = 552 K for HVO, respectively. According to Siebers [15], the lower volatility components of a fuel, i.e. the higher boiling point (e.g. $T_{b,90}$), control the liquid length, although Canaan et al. [16] found that the mid-boiling point correlated slightly better. This suggests that the $T_{b,90}$ and $T_{b,50}$ are indicators of the fuel's liquid penetration length and the evaporation tendencies in the spray. In addition to volatility, the fuel density also contributes to the evaporation characteristics of the liquid core, as a lighter fuel has more air entrainment into the spray [17]. Hence, more hot air is mixed into the liquid core, increasing the evaporation rate. From Table 1 it is clear that RME has the highest $T_{b,90}$, closely followed by diesel. HVO has the lowest $T_{b,90}$, suggesting that the HVO has the highest evaporation rate of the liquids. HVO also has the lowest fuel density, which additionally increases the evaporation rate.

2.2. The Optical Accessible Compression Ignition Chamber (OACIC)

The experiments were performed using the optically accessible compression ignition chamber (OACIC) at the Department

Table 1: Chemical and physical properties of all fuels.

	HVO	Diesel	RME
Cetane index[a] [-]	93.2	49.2	57.1
Lower heating value[b] [MJ/kg]	44.9	43.4	37.8
Density at 15°C[c] [kg/m^3]	779.5	848.7	883.3
Viscosity at 40°C[d] [mm^2/s]	2.918	3.209	4.434
$T_{b,90}$ [e] [K]	563.2	615.5	622.8
$T_{b,50}$ [e] [K]	551.6	556.2	611.0
Carbon [w%]	85.2	-	77.1[f]
Hydrogen [w%]	14.8	-	12.0[f]
Oxygen [w%]	0	-	10.9[f]
Fuel oxygen ratio Ω_f[g] [mol%]	0	-	3.61
Degree of unsaturation [mol^{-1}]	0.4	-	2.2

[a] ASTM D 4737-A [b] ASTM D240 [c] EN ISO 12185
[d] ASTM D445 [e] ASTM D 86 [f] EN 14103 [g] Ref. [18]

of Energy and Process Engineering, Norwegian University of Science and Technology (NTNU). The OACIC has also been used for experiments reported in [19] and [20], where details on the measurement techniques involved are given. Here, only a brief overview is provided. The OACIC is based on a single cylinder CI engine, where the engine head has been redesigned to allow for line-of-sight optical access, 50 mm in diameter, enabling optical measurements of fuel spray combustion. The installed injector has a single hole nozzle, eliminating the complexity of spray to spray interaction. This provides detailed measurements of in-flame soot production under real engine conditions. The OACIC is driven by an electrical motor running at a constant speed of 500 rpm, ensuring stable operation independent of the combustion. The intake air is compressed by a roots compressor and heated by an electrical heater. The intake pressure and temperature are controlled according to a predetermined set point. The most important information about the OACIC is listed in Table 2.

Table 2: Specifications of the OACIC.

Engine type	4-stroke, single-cylinder, direct injection engine
Bore/Stroke	130 mm/140 mm
Displaced volume	1.85 L
Compression ratio	15.9
Injector	Bosch CR second generation
Injector nozzle	Single hole, DSLA124P1659 62° wrt. central axis
Hole diameter	0.12 mm
Injection pressure	1000 bar
Injection duration	4.48 ms
Injection timing	2.7° before TDC

The thermodynamic conditions were chosen such that the ambient gas density was kept constant at top dead center (TDC), while the TDC temperature and pressure varied between the chosen conditions. This was achieved from only varying the intake pressure and temperature. The thermodynamic conditions were calculated based on a first law model together with the ideal gas law where heat transfer was estimated. The mass losses due to blow-by and other leakages were corrected for by reducing the compression ratio in the model such that the modelled pressure at TDC matched the measured pressure. This obviously did not yield the correct total air mass in the chamber, but gave a good estimation of the air pressure, temperature and density. Based on the model, the inlet temperatures and pressures required for a varying gas temperature at TDC, while maintaining a constant density of ~16.7 kg/m^3 were found. Table 3 shows the thermodynamic state of the four conditions used in this study. A more detailed description on the estimation of the ambient gas thermodynamic conditions is included in [20].

The flow field inside the chamber near TDC was assessed from schlieren-like measurements. The measurements showed that a rotational motion is present, rotating approximately 25°/ms.

2.3. Optical Diagnostics

2.3.1. Diffuse Back-Illuminated Extinction Imaging

For measuring in-flame soot, diffuse back-illuminated extinction imaging (DBIEI) was used. The technique is based on the principle of light extinction, where an incident light source is absorbed or scattered by particles in the optical path. The resulting transmitted light intensity is therefore lower than the incident light intensity, where transmittance is defined as the ratio between transmitted and incident light intensity. The optical depth KL can be calculated from the Beer-Lambert law [21],

$$\tau = \frac{I_t}{I_0} = exp\left(-\int_L k(x)dx\right) = exp\,(-KL) \tag{1}$$

where τ is the transmittance, I_t is the transmitted light intensity, I_0 is the incident light intensity, $k(x)$ is the local dimensional extinction coefficient, x is position along the light path, L is the total path length through the soot particle cloud and K is the path averaged dimensional extinction coefficient. In order to physically relate the measured extinction to the soot volume fraction, some optical and physical properties of soot are needed,

$$f_v = \frac{\lambda K}{k_e} \tag{2}$$

where f_v is the soot volume fraction, λ is the wavelength of the light and k_e is the dimensionless extinction coefficient. While K is calculated from the light extinction measurement (KL) and the path length L, the k_e is given as $k_e = 6\pi E(m)(1 + \alpha_{sa})$, where $E(m)$ is the imaginary part of $(m^2 - 1)/(m^2 + 1)$, m is the complex refractive index of soot and α_{sa} is the scattering-to-absorption ratio for the soot measured. For diesel combustion, α_{sa} is often assumed to be zero. The Engine Combustion Network (ECN) recommends $k_e = 7.2$ for light extinction measurements of soot in the wavelength of 628 nm [22]. The recommendation is valid for diesel-like spray combustion during the quasi-steady period. The estimated uncertainty of k_e is ±20%.

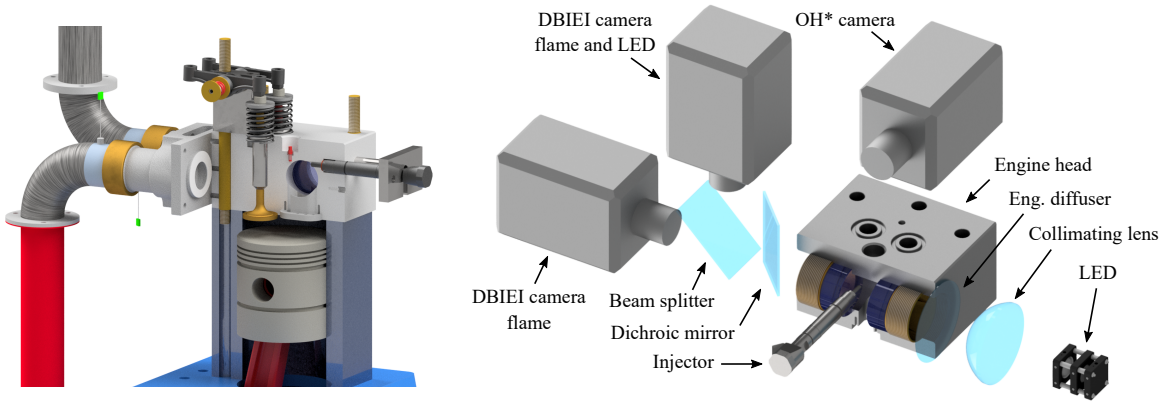

Figure 1: The OACIC and the optical setup.

Table 3: Thermodynamic conditions used in the OACIC at start of injection (SOI). The values in parentheses are the corresponding sample standard deviations.

	Condition 1	Condition 2	Condition 3	Condition 4
Inlet pressure [bar]	1.24	1.35	1.45	1.55
Inlet temperature [K]	327	354	381	408
Pressure at SOI [bar]	39.46 (0.11)	41.82 (0.11)	44.12 (0.16)	46.47 (0.16)
Temperature at SOI [K]*	819	868	916	966
Density at SOI [kg/m^3]*	16.7	16.7	16.7	16.7

* Calculated

Based on Equation 2, the volume of soot can be calculated by knowing the total measured volume. Since the measurement is performed using a CMOS sensor, KL is measured by a grid of pixels, each having a projected pixel area ΔA_{px}. The projected pixel area multiplied by the optical path length through the soot cloud results in the total volume, $L\Delta A_{px}$. Multiplying the total volume with the soot volume fraction, yields the soot volume, where the soot mass (m_{soot}) can be calculated from knowing the density of soot (ρ_{soot}).

$$m_{soot} = \rho_{soot} \frac{\lambda \cdot KL}{k_e} \Delta A_{px} \tag{3}$$

The density of soot varies within the flame, where nascent soot is lighter than mature soot. Totton et al. [23] recommended the density of nascent soot to be 1.12 g/cm^3, while Choi et al. [24] measured the density to be close to 1.8 g/cm^3. This illustrates the large uncertainty associated with soot mass density. The latter value is used in this study since this is most commonly reported for in-flame diesel combustion.

2.3.2. Optical Setup

The optical setup for DBIEI is shown in Figure 1, and is described in more detail in [25] and [20]. The light source was a light-emitting diode (LED) centred at 628 nm with a narrow wavelength distribution of 15 nm full width at half maximum (FWHM). The LED was pulsed with a duration of approximately 1.3 μs, allowing high power light intensity output. The light from the LED was collimated by a focusing lens and directed onto a large engineered diffuser (diameter of 100 mm) with a spreading angle of 15°. Beam steering effects related to the spatial and angular light intensity distribution from the engineered diffuser are addressed by Bjørgen et al. [25] for the current setup, following the guidelines of Westlye et al. [26].

In order to obtain the temporal development of the two-dimensional distribution of KL in the spray flame, the incident (I_0) and the transmitted light intensity distribution (I_t) was measured using high-speed cameras. I_0 was measured with no flame present, i.e. during a motored cycle prior to the combustion cycle. During a combustion cycle, the measurement of I_t is strongly influenced by the flame luminosity, I_f, as both are collected, hence resulting in the sum of the two, i.e. $I_{tf} = I_t + I_f$. Since it is I_t that is of interest, I_f must be subtracted from the recorded data. In this study, this was achieved by measuring I_f separately, using a second high-speed camera, measuring the same field of view via a beam splitter.

In order to only measure I_f, with no LED light pulse influence, a very small delay is added to the exposure of the camera measuring I_{tf}. In this way, I_f is measured almost simultaneously as I_{tf}, resulting in a good estimation of I_f. To account for any imperfect alignment of the two cameras, a transformation of I_f is applied. A detailed description of the technique can be found in [25].

The measurement of I_{tf} and I_f was performed using two high-speed cameras (Photron FASTCAM SA5). The optics for both cameras where identical, using a Nikkor 50 mm f/1.2

equipped with a 500D close-up lens, a narrow bandpass filter (centred at 630 nm with 10 nm FWHM) and neutral density filters in order to avoid saturation of the cameras. The cameras recorded at 100.000 frames per second, with an exposure duration of 1 μs.

2.3.3. Non-Ideal Camera Characteristics

For quantitative measurements using a high speed camera, special considerations should be taken regarding the background noise level of the camera. The background noise level has been shown to deviate from the static level when exposed to large changes in light intensities between two subsequent frames, as described by Manin et al. [27]. If the light intensity only changes by a small amount from frame to frame, this deviation is negligible. However, in the current study, a high power LED is alternating between on and off for every frame, i.e. alternating between a dark and bright frame, which almost extends over the entire dynamic range of the image sensor (12 bit, 0-4095 counts for the current camera), making this effect important to consider. A framework for dealing with local effects are provided in Appendix A.

2.3.4. OH Chemiluminescence Imaging*

In order to measure the high release rate zones in the flame, a narrow bandwidth in the ultraviolet (UV) spectrum of the flame was imaged (310 nm, FWHM 10 nm). The stoichiometric parts of the flame burns with a high temperature leading to the formation of electronically excited hydroxide (OH^*), primarily through the reaction $CH + O_2 \rightarrow CO + OH^*$. As OH^* returns to the ground state OH, an emission is released, which is known to be strong around 310 nm. [28, 29]. OH^* chemiluminescence was measured by a high speed camera (Photron FASTCAM SA-X2) connected to a gated intensifier (Lambert Instruments BV, II25) fitted with a UV 100 mm f/2.8 CERCO 2178 lens from Sodern. The camera was synchronized to half the speed of the DBIEI camera, i.e. 50.000 fps. The resolution was 256x256 with a physical pixel scale of 0.215 mm/pixel, and the gate time was set to 5 μs. The OH^* chemiluminescence camera was imaging the same field of view as the DBIEI system via a dichroic mirror, transmitting wavelengths longer than 480 nm to the DBIEI measurement and reflecting light with shorter wavelengths to the OH^* camera.

The high temperature IDT has been quantified according to the ECN standard [30]. The IDT was determined from the OH^* chemiluminescence measurements. The cool flame occurring prior to the high temperature heat release was not included in the IDT by setting a threshold between the maximum pixel count and the noise level of the camera. The maximum pixel count represents the high temperature flame and was found to be above 2000 counts on the camera. A cool flame was apparent when the pixel count exceeded ~200 counts on the camera. The threshold for high temperature IDT was set to 50% of the stabilised high temperature flame pixel count plateau, i.e. ~1000 counts.

The instantaneous FLOL was calculated based on a threshold corresponding to 50% of the knee point in the cross-axially integrated OH^* chemiluminescence measurement, based on a ±2.4 mm region from the central axis. Figure 2 shows a sample frame from the OH^* measurement, where the FLOL for the upper and lower half of the flame have been assessed separately. The FLOL used in the study is calculated as the average between the upper and lower FLOL. The threshold was determined by investigating several FLOL images and identifying the knee point value. Since the cross-axially integrated OH^* chemiluminescence signal raises quickly upstream of FLOL, the FLOL has a low sensitivity to the choice of the knee point value.

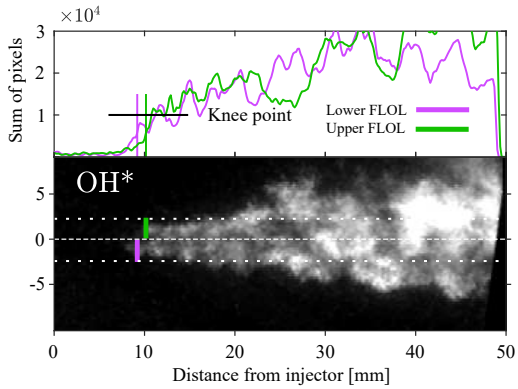

Figure 2: Sample image from an instantaneous OH^* chemiluminescence measurement showing the FLOL. Top: the cross-axially integrated OH^* for upper and lower half of the flame. Bottom: OH^* chemiluminescence image, where the upper and lower FLOL are indicated.

3. Results

3.1. Combustion Characteristics

3.1.1. Ignition Delay Time

As seen from Figure 3, HVO ignites first, followed by RME and diesel fuel. This behaviour is consistent with the cetane number rating of the fuels. RME shows a larger spread of IDT at the lower ambient gas temperatures than the other two fuels. The smallest spread in IDT was found for the high temperature cases for all fuels, indicating that the high gas temperatures yield a more stable ignition. Generally, the IDT asymptotically approaches infinity as the gas temperature decreases, resulting in having a high sensitivity to the gas temperature for lower gas temperature cases. The temporal development of the OH^* chemiluminescence is shown for the hottest condition for all fuels during the start of ignition period in Figure 4. As observed in Figure 3, ignition occurs in the order of HVO, RME and diesel.

The location of the initial ignition kernel is close to the injector hole for all fuels. This can be explained by the injection rate profile, obtained from momentum flux measurements, where the ramping up time was approximately 0.25 ms after start of injection (ASOI). During the ramping up time, the injected fuel has a lower velocity, causing the injected fuel to reside close to

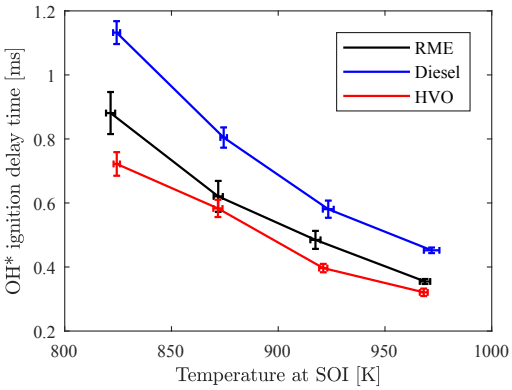

Figure 3: Ignition delay times based on OH* chemiluminescence for all fuels and conditions. The vertical bars show the 95% confidence interval of the true mean, while the horizontal bars show the ±1 sample standard deviation.

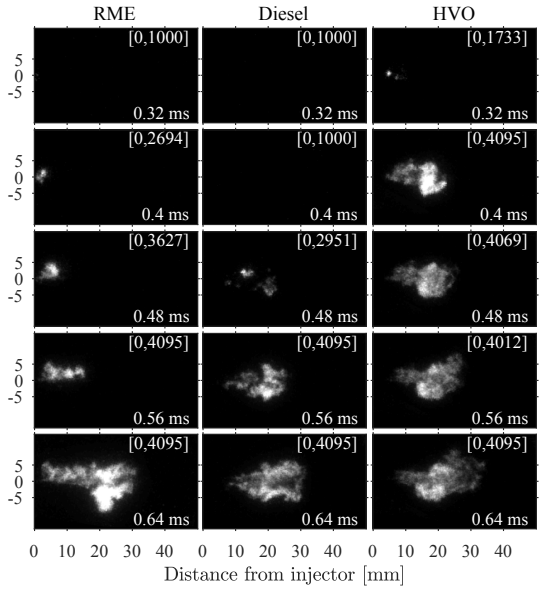

Figure 4: Temporal development of OH* during the premixed combustion phase for all fuels during condition 4 (hottest condition). The pixel count scale is given in brackets, where the upper bound is equal to the maximum pixel value in the image. The indicated time is time after SOI in milliseconds.

the nozzle hole, consequently igniting at this location. This was observed for all fuels and conditions in different degrees.

Other studies show that the initial ignition kernel is always located at or downstream of the stabilised FLOL location [31]. However, this is limited to a top hat injection rate profile in a quiescent chamber. Juneja et al. [32] found that the injection rate profile could influence the FLOL, and simulations of diesel-like sprays with a top hat and a slowly increasing injection rate profile were performed. For both of these cases, the FLOL stabilised after the premixed burn phase. The autoignition location of the top hat profile injection happened downstream of the stabilised FLOL, consistent with other spray combustion studies. For the slowly increasing injection rate case, the autoignition location occurred upstream of the FLOL, and stabilised at a distance closer to the nozzle than for the top hat case. The slowly increasing injection rate profile could be compared to the injection rate profile in the current study, where the initial injection period had a relatively low velocity.

3.1.2. Flame Lift-Off Length

Figure 5 shows the temporal development of the FLOL for all fuels and conditions, where the spread of the measured FLOL is indicated by the bands corresponding to ±1 sample standard deviation. For the lowest temperature case (condition 1), diesel fuel has a longer FLOL during the early stage, but stabilises after about 3 ms. For RME and HVO, the FLOL is relatively stable 1 ms ASOI. As ambient gas temperature rises, the FLOL shortens as expected. The FLOL of diesel fuel becomes less variable for elevated temperatures as well. For conditions 3 and 4, i.e. the two hottest conditions, diesel fuel and HVO have very similar FLOLs, while RME stabilises at a shorter distance from the injector. From these plots, the quasi-steady period is determined and indicated in the plots, i.e. between 3-4 ms ASOI. This period has a relatively stable FLOL and can be used to get representative ensemble-averaged values for the FLOL for all fuels.

Figure 6 shows the ensemble-averaged values of the FLOL for all fuels and conditions during the quasi-steady period (3-4 ms ASOI). The bars indicate the 95% confidence interval for the mean FLOL over the quasi-steady period, meaning that, based on the number of repetitions made during the measurement campaign (30 repetitions), there is a 95% probability that the true mean has a value within the error bars. The confidence interval is only based on random error of the FLOL, where systematic errors are not taken into account. Note that Figure 5 is displaying the sample standard deviation, indicating the actual spread of the FLOL during the measurements conducted. From Figure 6, RME is observed to have the shortest FLOL, while HVO and diesel have similar FLOLs. Comparing the FLOL to the IDTs, a clear difference can be observed. The IDT of HVO is clearly shorter than that of diesel, with RME in between diesel and HVO.

A correlation between IDT and FLOL for RME and diesel was observed, where RME had a shorter FLOL than diesel. However, the FLOL of HVO was found to be longer than that of RME, which does not follow the measured IDT trend. Following the ignition-based mechanism for FLOL stabilisation proposed by Pickett et al. [31], a shorter IDT is expected to result in a shorter FLOL. In a previous study [33], a correlation between the IDTs and the FLOLs was found for several fuels, however, some deviations were included. Manin et al. [34] also observed that the IDTs did not correlate directly to the FLOLs, where fuel-bound oxygen was hypothesised to be the explanation for the discrepancy. This indicates that the FLOL is also sensitive

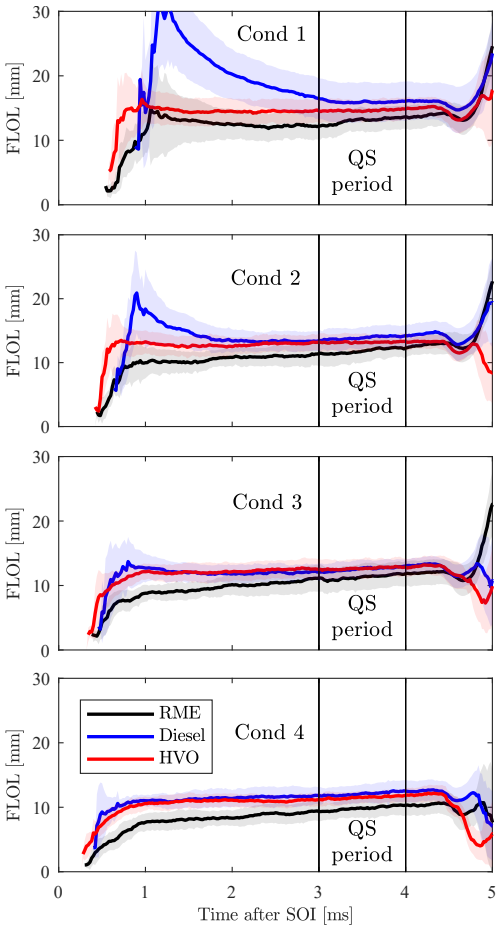

Figure 5: The ensemble-averaged flame lift-off length over time for all fuels and conditions, where the bands indicate the ±1 sample standard deviation.

to fuel chemical composition and test rig specifics.

Previous studies comparing HVO to diesel fuel show different results. For instance, Preuss et al. [35] found that HVO and diesel had similar FLOLs, where also their IDTs were similar. In the work of Pachiannan et al. [36], the FLOL of HVO and diesel fuel were measured for similar conditions as in the current study, resulting in HVO having a shorter IDT than diesel, but similar FLOLs. None of these studies presented a hypothesis on why this was observed.

Payri et al. [37] measured the FLOL of two Fischer-Tropsch fuels (FT1 and FT2). FT2 had a much lower boiling point at 90%, which resulted in a shorter liquid length compared to FT1. Comparing the IDT and FLOL of the two fuels, the IDTs were found to be similar. However, the FLOL of FT2, i.e. the lower boiling point fuel, was longer. An explanation for this could be the effect of cooling due to evaporation, where more liquid fuel evaporates upstream of FLOL for FT2 compared to FT1, consequently resulting in more cooling from evaporation, decreasing the temperature of the air-fuel mixture surrounding the liquid core. A lower temperature in the air-fuel mixture lengthens the stabilised FLOL. The same argument could also explain the unexpected longer FLOL of HVO compared to RME and diesel fuel, which will be discussed in the following section.

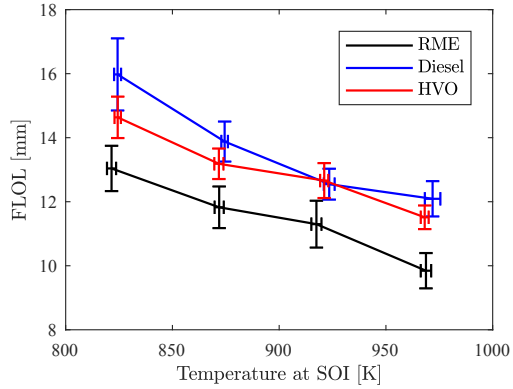

Figure 6: Ensemble-averaged flame lift-off length for all fuels and conditions. The vertical bars correspond to the 95% confidence interval of the true mean of FLOL, while horizontal error bars correspond to the ±1 sample standard deviation of the ambient gas temperature at SOI.

3.1.3. Liquid Evaporation

Continuing the previous hypothesis on why the FLOL of HVO is longer than expected, an analysis of the liquid evaporation for the three fuels is presented here. The ensemble-averaged liquid phase of the spray and the FLOL during the quasi-steady state were measured and are presented for all fuels and conditions in Figure 7. The images show the *KL* measurement overlaid by the OH^* measurement. The plots on the right hand side show the *KL* values along the central axis line. The liquid core is important since it reflects both evaporation and atomization properties of the fuel, which influences the air-fuel mixing taking place in the spray. It is important to note that the presented liquid penetration lengths overlap with the FLOLs, which therefore include heat release effects on the liquid lengths observed. The liquid length is not presented as a stand-alone result, but is used in the current analysis.

Diesel and HVO can be seen to have very similar liquid lengths, while RME has a longer liquid length. The peak value of *KL* associated with the liquid spray (not soot) is lowest for HVO, followed by diesel and RME. For conditions 1 and 2, diesel and RME have similar peak values, however, the peak values are close to the saturation limit of *KL*, making them false. The peak value of *KL* is hard to directly relate to the liquid volume fraction, because the droplet size distribution is unknown. However, with a few assumptions, some conclusions can be drawn.

According to Mie-scattering theory, the optical depth of a volume containing spherical particles (in this case liquid

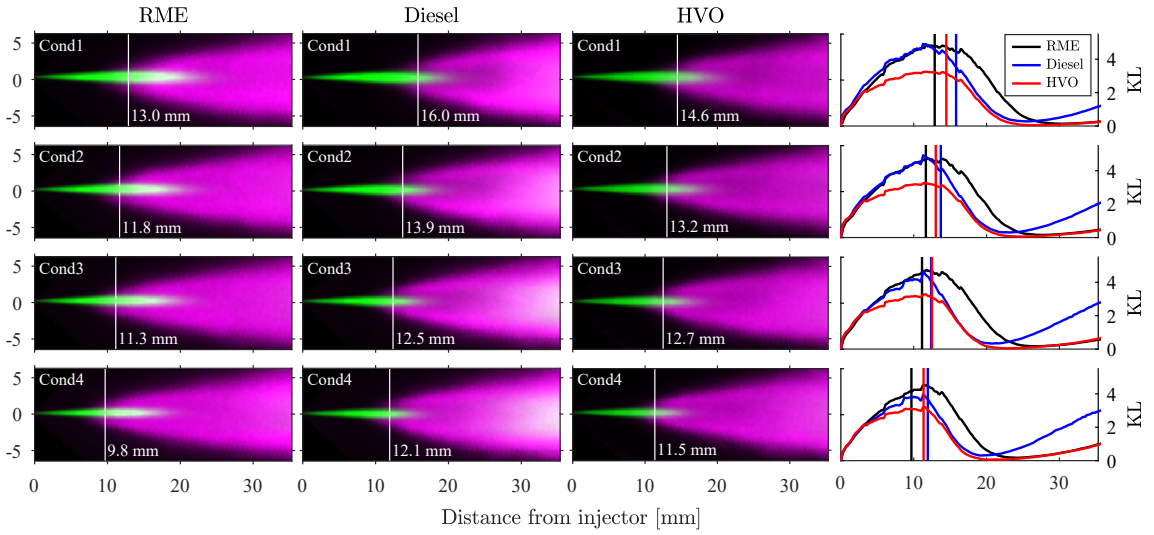

Figure 7: Ensemble-averaged KL measurement overlapped with the OH* measurement, where the green color map shows KL and magenta shows OH*. The plots on the right hand side show the values of KL along the central axis. The FLOL is shown as white vertical lines in the images and as colored vertical lines in the plots.

droplets), is a function of the extinction cross-section[2], the liquid volume fraction and the diameter of the droplets [38].

The droplet size in the liquid core can be expected to be larger than 1 μm, and Pickett et al. [38] computed the KL for droplets with diameters relevant for diesel sprays for two liquid volume fractions. The KL is directly proportional to the liquid volume fraction, but as mentioned varies according to the droplet size. For droplet diameters increasing above 1 μm, increasing values of liquid volume fraction result in increased KL. For a constant KL, the liquid volume fraction increases with increasing diameters.

The peak KL trend is proportional to the fuels' boiling points at 90% ($T_{b,90}$), i.e. HVO (563 K), diesel (615 K), RME (623 K), where RME has the highest peak KL and the highest $T_{b,90}$. In addition, the kinematic viscosity of the fuels has the order HVO (2.92 mm^2/s), diesel (3.21 mm^2/s), RME (4.43 mm^2/s), where higher kinematic viscosity generally leads to larger droplet diameters in the liquid core [39]. The combination of observing higher peak KL values and assuming larger droplet diameters for RME, results in higher liquid volume fractions. As an additional effect, the lower fuel density of HVO enhances air-fuel mixing, consequently contributing to increased evaporation rate, hence contributing to a decrease in the liquid volume fraction of HVO. This means that HVO can be expected to have the lowest liquid volume fraction, while RME has the highest.

For diesel and HVO, the liquid lengths and FLOLs are similar. Based on the former assumptions leading to HVO having a lower liquid volume fraction, and assuming that the heat release between them are similar, HVO would be expected to have a shorter liquid length than diesel. This suggests that HVO is evaporating at a lower rate than expected. The following argument could therefore be that HVO is evaporating under a lower temperature upstream of FLOL. The lower temperature in the air-fuel mixture of HVO could be due to the latent heat of vaporisation, where more fuel is evaporated for HVO compared to diesel, which reduces the temperature of the air-fuel mixture more than that of diesel.

The lower temperature in the air-fuel mixture could also explain why the FLOL of HVO and diesel are similar, where HVO is expected to have the shortest FLOL. A lower temperature upstream of the FLOL would decrease the reaction rates and consequently delay ignition for HVO, and thereby lengthening the FLOL. The same argument also fits to the observation of RME having a shorter FLOL than HVO, where less fuel has evaporated upstream of FLOL for RME, resulting in a higher temperature in the air-fuel mixture, hence a shorter FLOL. The ambient gas temperature has been shown to be exponentially proportional to the FLOL, having an exponent of -3.74 [40]. This illustrates that a difference in evaporation cooling in the air-fuel mixture upstream of FLOL can play an important role on the stabilisation of FLOL.

The evaporation cooling effect of the air-fuel mixture upstream of FLOL is expected to be more effective when the FLOL is shorter. For shorter FLOLs, there is less time for hot ambient air to mix in with fuel vapour in the spray, increasing the effect of evaporative cooling on FLOL stabilisation. The FLOLs observed in this study are considered relatively short.

[2]The local dimensional extinction coefficient $k(x)$ is the product of the extinction cross-section and the number density of droplets

3.2. Soot Characteristics

3.2.1. Premixed Combustion Period

The delay between the start of the first stage ignition and soot formation is the time needed for the entrained air to be consumed by low temperature reactions during the premixed combustion, consequently increasing the local temperature and resulting in a richer mixture consisting of fragmented fuel molecules, making the conditions ideal for soot formation.

Soot starts to form in the premixed phase approximately 0.25-0.35 ms after start of ignition. Figure 8 shows the start of ignition and start of soot formation ASOI, plotted against each other for conditions 2, 3 and 4. Condition 1 is not included in the plot since there was a relatively large spread for the start of soot formation due to the low ambient gas temperature. The start of soot formation is defined by the time from SOI to when soot production rate exceeded 30 μg/ms. A linear fit for each fuel shows that RME has the longest time between ignition and start of soot formation of 0.35 ms, HVO has 0.27 ms and diesel has 0.23 ms. The earlier formation of soot for diesel correlates with the expected high sooting tendency of diesel fuel, having aromatics and cycloalkanes which increase the production of soot precursors, yielding a higher probability of soot being formed earlier in the flame.

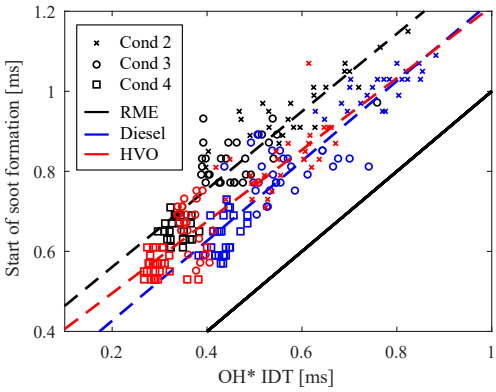

Figure 8: IDT from OH* chemiluminescence plotted against start of soot formation (both given as time ASOI), for condition 2, 3 and 4. The black line indicates the one-to-one combination of both quantities, and the dotted lines are linear fits of each individual fuel. The average time between ignition and start of soot formation was 0.23 ms (diesel), 0.27 ms (HVO) and 0.35 ms (RME).

Assuming that as the ambient gas temperature increases, the IDT accordingly decreases, resulting in less time for fuel to evaporate and mix with the ambient gas. A higher ambient gas temperature therefore results in reduction of the amount of premixed combustion, characterised with lower heat release rates. The shorter IDTs result in less air mixing with the fuel vapour, resulting in a richer flame, and more soot being produced at a higher rate during the premixed combustion phase. In Figure 8, the time between ignition and soot formation does not change much with varying ambient gas temperatures, as demonstrated by the slopes of the linear fits, except for HVO, were the soot formation delay slightly increases with decreasing IDTs. The stable soot formation time delay for changing ambient gas temperatures suggests that the initial soot formation rate is insensitive to changes in premixed air-fuel ratios. A richer premixed air-fuel mixture along with higher temperatures should increase the soot formation rate, reducing the time between ignition and soot mass production rate reaching 30 μg/ms. A possible explanation for this could be that the air-fuel mixture is only partially premixed, and therefore has local equivalence ratios ranging from very lean to very rich, for all conditions. This results in always having the optimal condition needed for rapid soot formation.

During the premixed combustion period, soot is formed mainly downstream of the liquid length. The total soot mass in the flame was calculated for each frame measured during the premixed period. This was done by masking the KL measurement regions not containing soot, such as the liquid core and the chamber walls. This can be seen in Figure 9 for all fuels combusting under condition 4, where each frame shown are ensemble-averaged over 30 injections. The white line in Figure 9 indicates where the FLOL is located, while the red line indicates the liquid length. The time after start of ignition together with the instantaneous soot mass production rate are indicated for each frame.

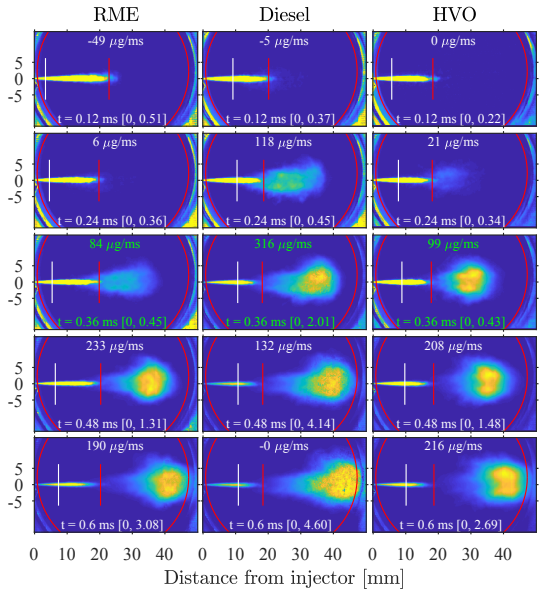

Figure 9: Ensemble-averaged temporal development of KL for all fuels during condition 4. The white line represents the FLOL, the red line represents the end of the liquid core and the red circle represents the valid domain for the KL measurement. The indicated time is time after ignition, where the selected time after ignition (0.36 ms) is shown in green.

The instantaneous soot mass production rate was calculated based on the frame-to-frame change in total sum of KL, including the liquid core. For the ensemble-averaged frames, the liq-

uid core remains nearly unchanged from frame to frame since it has reached stable liquid penetration length, resulting in a negligible effect on the calculation of the soot mass production rate. The total soot mass was calculated based on the region limited to downstream of the liquid length line and the inside the red circle.

The calculation of the total soot mass and the soot mass production rate are limited by two factors. The first limiting factor occurs when the amount of soot present in the line-of-sight becomes large and saturates the DBIEI measurement. The transmitted light is attenuated to a level below the camera's noise level, and the calculated quantity KL reaches the saturation limit. For the current system, this level was measured to be $KL \approx 4.6$. For values close to the saturation limit (in soot dense regions), errors from the flame luminosity estimation combined with random noise generated by the camera result in a large impact on the calculated KL. This is observed in Figure 9 for diesel fuel in the bottom row, where the high sooting region has a noisy KL plateau for values close to the saturation limit of 4.6. This was mainly a problem for diesel fuel, limiting the measurement to 0.36 ms after start of ignition. In order to be able to compare all fuels at the same time after start of ignition, the saturation of KL for diesel fuel became a limiting factor. The second limitation occurred when the flame exited the measurement domain before soot started to form, not including the entire soot mass cloud in the calculation. This happened earlier than 0.36 ms after start of ignition for all fuels for condition 1 and 2, resulting in only condition 3 and 4 providing the soot mass production in that time period. Figure 10 shows the total soot mass in μg and the corresponding soot mass production rate in μg/ms, where 0.36 ms after ignition is indicated as circles.

The values for the total soot mass and soot mass production rate at 0.36 ms after ignition are plotted against the IDTs for condition 3 and 4 in Figure 11. The plots show a similar trend for all fuels. An increase in total soot mass and soot mass production rate is observed for all fuels going from condition 3 to 4, i.e. more soot is produced with increasing ambient gas temperatures (except for the total soot mass of HVO). However, the 95% confidence intervals between the conditions for some of the fuels are overlapping, making the increase in soot between the conditions not significant. The difference between diesel and HVO/RME is however very clear, where diesel produces much more soot for the same IDTs.

3.2.2. Mixing-Controlled Combustion Period

During the mixing-controlled combustion period, the spray flame approaches a quasi-steady state where the FLOL stabilises, yielding a stable air-fuel mixture prior to ignition. This results in a spatially stable production of soot in the spray. The spatial development of in-flame soot production in the axial direction is therefore analogous to a measure of soot production over time. The spatial development of total soot mass can be calculated by integrating the two-dimensional KL measurement along the cross-axial direction, i.e. perpendicular to the spray axis. Since the KL measurement is a line-of-sight measurement, the total amount of soot in a cross-axial slice is captured.

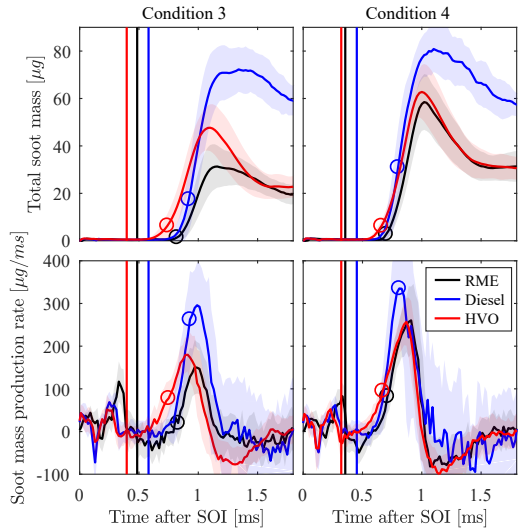

Figure 10: Total soot mass (first row) and soot mass production rate (second row) over time ASOI for condition 3 and 4. The graphs are ensemble-averaged based on 30 injections each and the bands indicate the ±1 sample standard deviation. The vertical lines indicate start of ignition for all fuels and the circles indicate the corresponding values 0.36 ms after start of ignition.

The axial development of the soot mass is then obtained for each captured frame, giving a measure for instantaneous soot mass production. Figure 12 shows the definition of the soot gradient, which provides a single quantity of the soot mass production rate during the mixing-controlled period. The bottom image shows a single frame of KL for HVO combusting under condition 4. The top graph shows the cross-axially integrated KL (ΣKL). The soot gradient is based on the slope of ΣKL 20.2 mm downstream of the FLOL, where the soot gradient calculation is based on Equation 3. The soot gradient is given as soot mass per length, and is analogous to the soot mass production rate during the premixed period defined earlier, since an axial variation of the soot mass is the result of a temporal variation. Choosing to use a fixed distance from the FLOL results in similar residence times for each fuel and condition between the point of ignition and the chosen point of soot production.

The choice of 20.2 mm downstream of the FLOL was made due to restrictions from the highest sooting case, i.e. diesel during condition 4. As mentioned, the KL saturates for a value of approximately 4.6, making the higher sooting parts of the flame invalid. In order to include reasonable values from the lower sooting cases, the distance should be as long as possible. The distance of 20.2 mm for diesel at condition 4 was invalid, since it overlaps with the saturated parts of the flame, however, it provided reasonable values for all other cases.

Figure 13 shows the axial distribution of the soot mass in a 0.1 mm wide slice along the central axis. This was calculated by scaling the soot mass in each pixel-wide slice. The solid line shows the ensemble-averaged soot mass during the quasi-steady period, where the bands indicate the 95% confi-

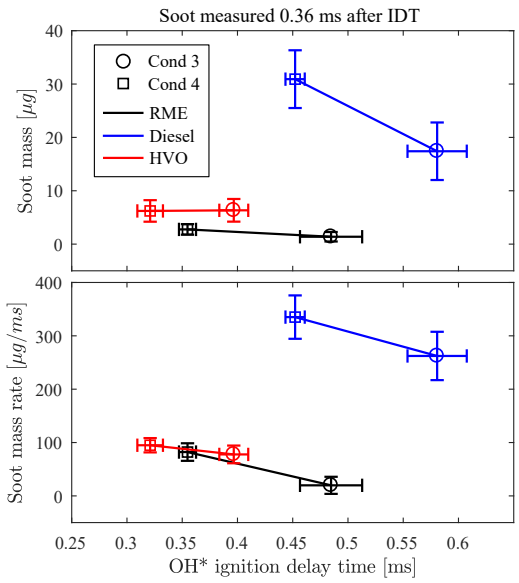

Figure 11: The upper graph shows the total soot mass produced in μg and the lower graph shows the soot mass production rate in μg/ms. The values are taken 0.36 ms after start of ignition for condition 3 and 4. The bars show the 95% confidence interval for the true mean.

dence interval. The circles indicate the soot mass in a 0.1 mm wide slice 20.2 mm downstream of the FLOL, which was also the point where the soot gradient was measured. The soot mass and soot gradient 20.2 mm downstream of FLOL are shown in Figure 14 as function of FLOL. Note that for diesel at condition 4, the value is invalid due to saturation of KL.

A clear trend is found for all fuels, as the FLOL decreases, due to increased ambient gas temperature, the soot gradient increases accordingly. The increase in soot gradient is due to a higher equivalence ratio at FLOL, caused by less time for air to entrain and mix with fuel vapour in the spray. Figure 14 shows the FLOL plotted against the soot gradient and the soot mass, where the bands indicate the 95% confidence interval of the true mean. For a constant FLOL, RME produces the least soot, closely followed by HVO, and diesel produces the most.

The soot mass production rate and the soot mass gradient shown in Figure 11 and Figure 14 show very similar trends in sooting tendencies of the fuels. The same trend was found for the total soot mass during the premixed phase and the soot mass during the mixing-controlled phase. The trends are consistent with reported soot measurements found in literature, where diesel is sooting substantially more than RME and HVO. This is mainly connected to the aromatic content in diesel fuels. From these measurements, RME is observed to have a lower sooting tendency than HVO, which can be explained by the fuel-bound oxygen present in RME. The number of carbon-carbon bonds is also an important parameter controlling the sooting tendency, were a higher number of carbon-carbon bonds results in a higher sooting tendency. However, RME has an aver-

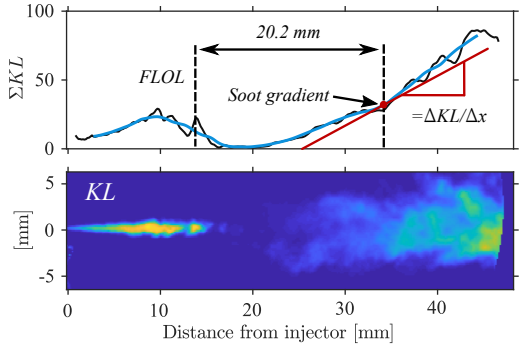

Figure 12: Bottom image shows KL measured 2.94 ms ASOI for HVO combusting under condition 4. The top image shows the cross-axially integrated KL (ΣKL), i.e. the sum of KL for each pixel column. The black line is ΣKL, the blue line is the corresponding filtered ΣKL. The soot gradient is calculated based on the slope of ΣKL at a point 20.2 mm downstream of the FLOL.

age number of carbon-carbon bonds of 16.9, while HVO has approximately 16-17, resulting in similar sooting tendencies based on this.

The soot production during the mixing-controlled period is possibly affected by other factors than the fuels' sooting tendencies and the equivalence ratio at FLOL. The soot production rate has previously shown to increase for increasing ambient gas temperatures under similar air-fuel mixing conditions [41, 20]. Following individual fuels with increasing ambient temperatures in Figure 14, the soot production is expected to be higher than for the case with constant ambient gas temperature and increasing equivalence ratios.

Another effect that could affect the soot production in the current study is the effect of liquid/flame overlap. This results in liquid droplets being vaporised in the flame, consequently having short time to mix with air before ignition occurs. Hence, the combusting air-fuel mixture becomes richer and has a higher tendency to produce soot. When comparing RME to HVO and diesel, the liquid part of RME is observed to overlap more with the flame. Consequently, more soot could be produced for RME relative to HVO and diesel due to the larger overlap.

4. Conclusions

The two-dimensional distribution of OH* chemiluminescence and the optical depth of soot (KL) have been measured temporally at high speed (50 kHz) in a CI chamber for HVO, diesel and RME. From this, detailed quantitative data of in-flame soot mass are produced, enabling validation of simulations. The thermodynamic conditions used in the chamber were representative of that in a CI engine.

- The IDT based on OH* chemiluminescence was ordered as HVO, RME and diesel, where HVO had the shortest IDT. The IDT trend matched the cetane number rating of the fuels.

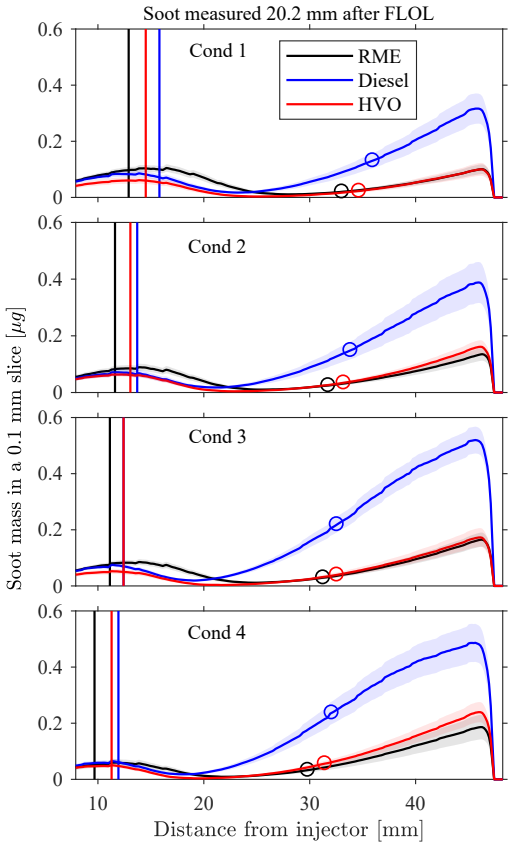

Figure 13: Soot mass in a 0.1 mm slice as function of distance from injector, where the liquid core is included on the right hand side. The FLOLs are indicated as vertical lines. The bands indicate the 95% confidence interval of the true mean.

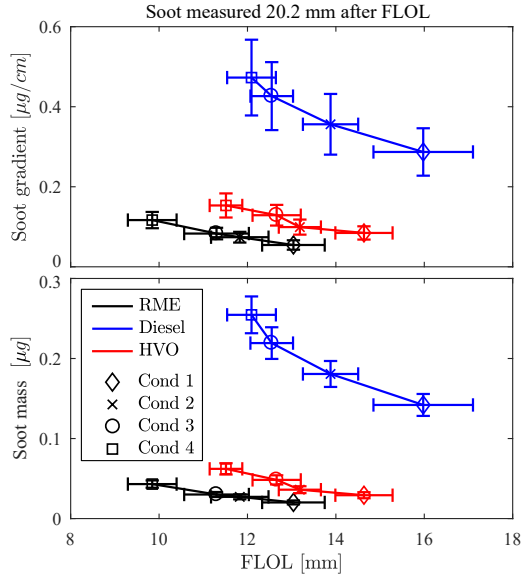

Figure 14: Top: the soot gradient as function of FLOL. Bottom: soot mass in a 0.1 mm slice as function of FLOL. Soot quantities were measured 20.2 mm downstream of FLOL. The bands indicate the 95% confidence interval of the true mean.

- The FLOLs during the quasi-steady period was ordered as RME, HVO and diesel, where RME had the shortest, and HVO and diesel had similar FLOLs. The FLOL did not match the IDT trend. A possible reason for the mismatch could be due to differences in air-fuel mixture temperature upstream of the FLOL, which might be caused by differences in evaporative cooling between the fuels. A higher rate of evaporation cools the air-fuel mixture, consequently lengthening the FLOL. This is expected to have a stronger effect for shorter FLOLs, where less time is available for mixing in hot ambient air.

- The time between autoignition and start of soot formation was found to be stable regardless of the ambient gas temperature for the individual fuels, even though the percentage of fuel vapour mixed in with air in the premixed portion varied between the conditions. Between the fuels, diesel had the shortest time delay, followed by HVO and RME, which follow their respective sooting tendencies.

- The soot mass production rate and the total soot mass during the premixed phase was measured 0.36 ms after start of ignition, where RME and HVO produced the lowest amount of the soot, while diesel had 3-6 times higher soot mass production rate and total soot mass.

- During the quasi-steady period, i.e. 3-4 ms ASOI, the soot mass production and the soot mass in a 0.1 mm slice was measured 20.2 mm downstream of the FLOL. The soot production versus FLOL trends during the quasi-steady period was very similar to the soot production versus IDT trends found during the premixed phase, supporting that the change in FLOL and IDT results in similar relative changes in equivalence ratio at FLOL and in the premixed plume.

- The order of soot mass production during the mixing-controlled and premixed combustion period, from lowest to highest, was RME, HVO and diesel. This is consistent to the sooting tendencies of the fuels. The high sooting tendency of diesel is attributed to the aromatic content. Comparing RME and HVO, the lower sooting tendency of RME can be explained by the oxygen content, since the number of carbon-carbon bonds between the two fuels are similar.

Acknowledgement

The experiments were conducted in the Motorlab at the Norwegian University of Science and Technology in Trondheim,

Norway. The laboratory is supported by the research center Bio4fuels, which is part of Centers for Environment-friendly Energy Research (FME) funded by the Norwegian Research Council.

Appendix A. Non-Ideal Camera Characteristics

As the camera is exposed to a sudden change in light intensity from one frame to the next, e.g. from a dark frame to a bright frame, the measured raw intensity is higher than the actual exposed intensity. The overcompensation is called image lag and is due to leftover charge in the complementary metal-oxide semiconductor (CMOS) sensor, affecting the subsequent frame.

The effect of the image lag on a frame can be view on as a change in the background noise level, which is used as the reference level of the measurement. This means that the static background noise level can no longer be used as the reference level, since it changes depending on the frame-to-frame change in exposed intensity. A dynamic background noise level must therefore be considered when calculating the quantities needed for calculation of the optical depth of soot.

In the following section, the raw intensity is referring to the actual output in counts from a pixel on a CMOS sensor, which includes the background noise level of the camera, denoted as primed quantities. The exposed/real/actual intensity is referring to the intensity resulting solely from the light source, excluding the background noise level, denoted as non-primed quantities.

Appendix A.1. Image Lag Without Flame

The left hand side of Figure A.15 shows the light intensity read by a single pixel for three subsequent frames where no extinction or flame luminosity is present in the optical path (I_0). The three bars show the raw pixel intensity levels denoted as $I'_{0,n-1}$, $I'_{0,n}$ and $I'_{0,n+1}$, where n is the frame number exposed to the LED light, referred to as the bright image, while $n-1$ and $n+1$ are the frame numbers of the dark image before and after the bright image, respectively. The static background noise level is indicated by BGs, which is measured by capturing a dark frame that is followed by several dark frames[3].

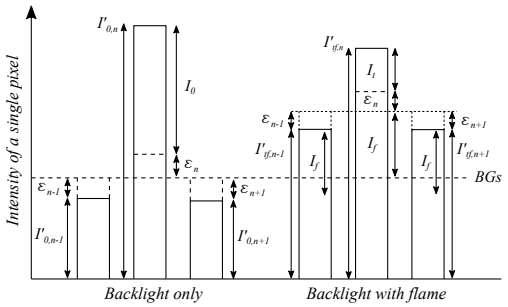

Figure A.15: The effect of image lag on a single pixel in three subsequent frames, which are exposed to an alternating light source. The three bars to the left are not affected by flame luminosity, while the three bars on the right are. Primed quantities (e.g. $I'_{0,n}$) are raw intensity values, while non-primed quantities are real intensity values (e.g. I_f), BGs is the static background level and ε is the image lag.

[3]Equivalent to "shading correction" on a Photron camera and "black reference correction" on a Phantom camera

$I'_{0,n+1}$ has a lower value than BGs, which is a direct effect of the image lag, where the static background can no longer be used as the reference level. This indicates that a reduction in the background noise level has occurred, since $I'_{0,n+1}$ is not exposed to light at all. The difference between BGs and $I'_{0,n+1}$ gives the change from the static background noise level, i.e. the image lag ε_{n+1}. Measurements show that the current camera responds to this effect locally, i.e. single pixels are directly affected. A global effect is also observed, but is relatively small in comparison. Therefore, only the local effects are considered and described here.

As seen on the left hand side of Figure A.15, an image lag occurs for all images experiencing a frame-to-frame change in light intensity. For the bright image, the measured raw intensity consequently consists of $I'_{0,n} = BGs + \varepsilon_n + I_0$. If the measurement is referred to the static background noise level BGs, the intensity of the incident light is given as $I_0+\varepsilon_n$, where the image lag is included as an error to the measurement.

As mentioned, ε_n is affected by the difference in light intensity from one frame to the next. The difference in exposed intensity from the dark frame (I_{n-1}) to the bright frame (I_n) is in this case $\Delta I_n = I_0 - 0$, where I_0 is the actual incident light intensity. The magnitude of the image lag ε_n is assumed to be proportional to the absolute difference in exposed intensity:

$$\varepsilon_n = C|I_n - I_{n-1}| = C|\Delta I_n|,$$

where,

$$C = \alpha > 0, \quad \text{when } \Delta I_n > 0,$$
$$C = \beta < 0, \quad \text{when } \Delta I_n < 0,$$

where α and β are constants specific to the camera. The proportionality constant C changes depending on the direction of change in intensity. If the camera is exposed to a dark image and a following bright image, the change in intensity is positive, resulting in positive image lag, i.e. $C = \alpha > 0$. The image lag of the bright image can now be written as $\varepsilon_n = \alpha I_0$, since $\Delta I_n > 0$.

If the camera is exposed to a bright image and a following dark image, a similar effect occurs, but in the opposite direction since $\Delta I_{n+1} = 0 - I_0 < 0$, hence $\varepsilon_{n+1} = \beta I_0$. The image lag of $I'_{0,n+1}$ is now given as $\varepsilon_{n+1} = \beta I_0$, where β has a negative value.

Based on this, the value of I_0 can be calculated from the difference between the measured raw intensities, i.e. $I'_{0,n} - I'_{0,n-1}$, and the camera specific constants α and β:

$$I_0 = \frac{I'_{0,n} - I'_{0,n-1}}{1 + \alpha + \beta}. \tag{A.1}$$

Appendix A.2. Image Lag with Flame

Same methodology can be applied to the case of a sooty flame being present in the optical path. The right hand side of Figure A.15 shows the pixel raw intensity value of a bright frame and a following dark frame, i.e. $I'_{tf,n}$ and $I'_{tf,n+1}$, respectively, where both are affected by flame luminosity. The total

radiation received by the sensor during the bright frame can be split into two parts, $I_{tf} = I_t + I_f$, i.e. the transmitted backlight (I_t) and the flame luminosity (I_f), respectively. The total radiation read by the dark frame is only I_f.

Similar to the former case, the difference in exposed intensity between the frames will alter the background noise level of each frame. The difference in exposed intensity between frame $n-1$ and frame n is $\Delta I_n = I_{tf} - I_f = I_t$. Similar for frame n and frame $n+1$, $\Delta I_{n+1} = I_f - I_{tf} = -I_t$. This results in having an image lag of $\varepsilon_n = \alpha I_t$ and $\varepsilon_{n+1} = \beta I_t$ for the bright and the dark frame, respectively. Hence, the corrected reference level for the bright and dark frame is $(BGs + \alpha I_t)$ and $(BGs + \beta I_t)$, respectively. As for the former case of I_0, I_t can be determined based on the difference between the measured raw intensities $(I'_{tf,n} - I'_{tf,n-1})$ and the camera specific constants α and β:

$$I_t = \frac{I'_{tf,n} - I'_{tf,n-1}}{1 + \alpha + \beta} \tag{A.2}$$

Since it is the optical depth that we are interested in, the ratio between the transmitted intensity and the incident intensity for frame n is given by,

$$\frac{I_t}{I_0} = \frac{I'_{tf,n} - I'_{tf,n-1}}{I'_{0,n} - I'_{0,n-1}}, \tag{A.3}$$

where all quantities needed are measured raw intensities. An important assumption made here is that the flame luminosity have small frame-to-frame changes.

Appendix A.3. Measurement of α and β

In order to investigate the camera specific coefficients α and β, a measurement of I'_0 was performed with an alternating light source. The entire dynamic range of the camera was investigated by placing a shaded gradient in the line of sight, also containing a pattern in order to determine that the image lag was local. Measurements of the static background noise level BGs, static bright image $(BGs + I_0)$, dynamic bright image $(I'_{0,n} = BGs + \varepsilon_n + I_0)$ and dynamic dark image $(I'_{0,n+1} = BGs - \varepsilon_{n+1})$ were performed. The values of α and β based on the ensemble-averaged images of the mentioned quantities were calculated from,

$$\alpha = \frac{\varepsilon_n}{I_0} = \frac{I'_{0,n} - (BGs + I_0)}{I_0}, \quad \beta = \frac{\varepsilon_{n+1}}{I_0} = \frac{I'_{0,n+1} - BGs}{I_0} \tag{A.4}$$

The pixel distribution of α and β are displayed in Figure A.16, showing that the two are similar in magnitude, and have opposite signs, i.e., ± 0.015. Most importantly, they are not varying much over the I_0 intensity range, supporting the assumption of the image lag being proportional to the exposed intensity difference. This verifies Equation A.3, and can be used for a DBIEI setup where the backlight is alternating between camera exposures.

The values of α and β for pixel values below 750 counts resulted in ε_n having a value below the random noise level of the camera ($\varepsilon_n = \alpha I_0 < 10$ counts), which means that the image lag is not observed since it can not be distinguished from the random noise of the camera. The valid interval for α and β is therefore between 750 and 4095 counts for the current camera.

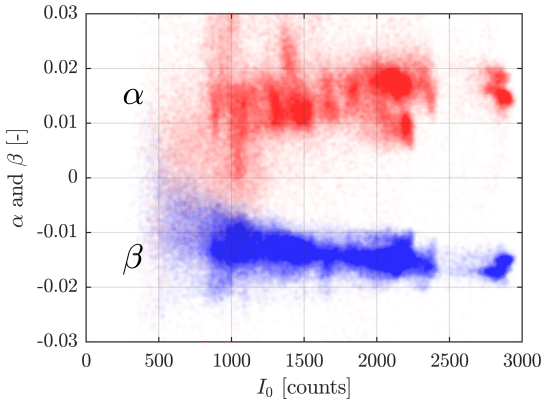

Figure A.16: Measurement of α and β, represented in red and blue respectively.

References

[1] G. W. Huber, P. O'Connor, A. Corma, Processing biomass in conventional oil refineries: Production of high quality diesel by hydrotreating vegetable oils in heavy vacuum oil mixtures, Applied Catalysis A: General 329 (2007) 120–129.

[2] A. Engman, T. Hartikka, M. Honkanen, U. Kiiski, Neste Renewable Diesel Handbook, Tech. rep., Neste Oyj (2016).

[3] T. Murtonen, P. Aakko-Saksa, M. Kuronen, S. Mikkonen, K. Lehtoranta, Emissions with Heavy-duty Diesel Engines and Vehicles using FAME, HVO and GTL Fuels with and without DOC+POC Aftertreatment, SAE International Journal of Fuels and Lubricants 2 (2) (2009) 147–166.

[4] H. Aatola, M. Larmi, T. Sarjovaara, S. Mikkonen, Hydrotreated Vegetable Oil (HVO) as a Renewable Diesel Fuel: Trade-off between NOx, Particulate Emission, and Fuel Consumption of a Heavy Duty Engine, SAE International Journal of Engines 1 (1) (2008) 1251–1262.

[5] D. Kim, S. Kim, S. Oh, S.-Y. No, Engine performance and emission characteristics of hydrotreated vegetable oil in light duty diesel engines, Fuel 125 (2014) 36–43.

[6] Y. Wu, J. Ferns, H. Li, G. Andrews, Investigation of Combustion and Emission Performance of Hydrogenated Vegetable Oil (HVO) Diesel, SAE International Journal of Fuels and Lubricants 10 (3).

[7] T. Bohl, A. Smallbone, G. Tian, A. P. Roskilly, Particulate number and NOx trade-off comparisons between HVO and mineral diesel in HD applications, Fuel 215 (2018) 90–101.

[8] T. Bohl, G. Tian, A. Smallbone, A. P. Roskilly, Macroscopic spray characteristics of next-generation bio-derived diesel fuels in comparison to mineral diesel, Applied Energy 186 (2017) 562–573.

[9] Q. Cheng, H. Tuomo, O. T. Kaario, L. Martti, Spray dynamics of HVO and EN590 diesel fuels, Fuel 245 (2019) 198–211.

[10] T. Zhang, M. Andersson, K. Munch, I. Denbratt, Optical Diagnostics of Spray Characteristics and Soot Volume Fractions of *n* -Butanol, *n* -Octanol, Diesel, and Hydrotreated Vegetable Oil Blends in a Constant Volume Combustion Chamber, in: SAE Technical Paper Series, 2019.

[11] T. Xuan, J. Cao, Z. He, Q. Wang, W. Zhong, X. Leng, D. Li, W. Shang, A study of soot quantification in diesel flame with hydrogenated catalytic biodiesel in a constant volume combustion chamber, Energy 145 (2018) 691–699.

[12] A. Gómez, J. A. Soriano, O. Armas, Evaluation of sooting tendency of different oxygenated and paraffinic fuels blended with diesel fuel, Fuel 184 (2016) 536–543.

[13] M. Lapuerta, M. Villajos, J. R. Agudelo, A. L. Boehman, Key properties and blending strategies of hydrotreated vegetable oil as biofuel for diesel engines, Fuel Processing Technology 92 (12) (2011) 2406–2411.

[14] W. Zhong, P. Tamilselvan, Q. Wang, Z. He, H. Feng, X. Yu, Experimental study of spray characteristics of diesel/hydrogenated catalytic biodiesel blended fuels under inert and reacting conditions, Energy 153 (2018) 349–358.

[15] D. L. Siebers, Liquid-Phase Fuel Penetration in Diesel Sprays, in: SAE Technical Paper Series, 1998.

[16] R. E. Canaan, J. E. Dec, R. M. Green, D. T. Daly, The Influence of Fuel Volatility on the Liquid-Phase Fuel Penetration in a Heavy-Duty D.I. Diesel Engine, 1998, p. 980510.

[17] J. Naber, D. L. Siebers, Effects of Gas Density and Vaporization on Penetration and Dispersion of Diesel Sprays, in: SAE Technical Paper Series, 1996.

[18] C. J. Mueller, W. J. Pitz, L. M. Pickett, G. C. Martin, D. L. Siebers, C. K. Westbrook, Effects of Oxygenates on Soot Processes in DI Diesel Engines: Experiments and Numerical Simulations, in: SAE Technical Paper Series, 2003.

[19] V. Krivopolianskii, K. O. P. Bjørgen, D. Emberson, S. Ushakov, V. Æsøy, T. Løvås, Experimental Study of Ignition Delay, Combustion, and NO Emission Characteristics of Hydrogenated Vegetable Oil, SAE International Journal of Fuels and Lubricants 12 (1) (2019) 29–42.

[20] K. O. P. Bjørgen, D. R. Emberson, T. Løvås, Optical Measurements of In-Flame Soot in Compression-Ignited Methyl Ester Flames, Energy & Fuels (2019) acs.energyfuels.9b01467.

[21] H. Zhao, N. Ladommatos, Optical Diagnostics for Soot and Temperature Measurement in Diesel Engines, Progress in Energy and Combustion Science 24 (3) (1998) 221–255.

[22] S. Skeen, K. Yasutomi, E. Cenker, B. Adamson, N. Hansen, L. Pickett, Standardized Optical Constants for Soot Quantification in High-Pressure Sprays, SAE International Journal of Engines 11 (6) (2018) 805–816.

[23] T. S. Totton, D. Chakrabarti, A. J. Misquitta, M. Sander, D. J. Wales, M. Kraft, Modelling the Internal Structure of Nascent Soot Particles, Combustion and Flame 157 (5) (2010) 909–914.

[24] M. Y. Choi, G. W. Mulholland, A. Hamins, T. Kashiwagi, Comparisons of the Soot Volume Fraction Using Gravimetric and Light Extinction Techniques, Combustion and Flame 102 (1) (1995) 161–169.

[25] K. O. P. Bjørgen, D. R. Emberson, T. Lovas, Diffuse Back-Illuminated Extinction Imaging of Soot: Effects of Beam Steering and Flame Luminosity, in: SAE Technical Paper Series, 2019.

[26] F. R. Westlye, K. Penney, A. Ivarsson, L. M. Pickett, J. Manin, S. A. Skeen, Diffuse Back-Illumination Setup for High Temporally Resolved Extinction Imaging, Applied Optics 56 (17) (2017) 5028.

[27] J. Manin, S. A. Skeen, L. M. Pickett, Performance comparison of state-of-the-art high-speed video cameras for scientific applications, Optical Engineering 57 (12) (2018) 1.

[28] A. G. Gaydon, The Spectroscopy of Flames., 2nd Edition, Springer Verlag, 1974, oCLC: 864087852.

[29] B. Higgins, D. Siebers, Measurement of the Flame Lift-Off Location on DI Diesel Sprays Using OH Chemiluminescence, in: SAE Technical Paper Series, 2001.

[30] P. M. Lillo, L. M. Pickett, H. Persson, O. Andersson, S. Kook, Diesel Spray Ignition Detection and Spatial/Temporal Correction, SAE International Journal of Engines 5 (3) (2012) 1330–1346.

[31] L. M. Pickett, D. L. Siebers, C. A. Idicheria, Relationship Between Ignition Processes and the Lift-Off Length of Diesel Fuel Jets, in: SAE Technical Paper Series, 2005.

[32] H. Juneja, Y. Ra, R. D. Reitz, Optimization of Injection Rate Shape Using Active Control of Fuel Injection, 2004, pp. 2004–01–0530.

[33] S. Kook, L. M. Pickett, Soot Volume Fraction and Morphology of Conventional, Fischer-Tropsch, Coal-Derived, and Surrogate Fuel at Diesel Conditions, SAE International Journal of Fuels and Lubricants 5 (2) (2012) 647–664.

[34] J. Manin, S. Skeen, L. Pickett, E. Kurtz, J. E. Anderson, Effects of Oxygenated Fuels on Combustion and Soot Formation/Oxidation Processes, SAE International Journal of Fuels and Lubricants 7 (3) (2014) 704–717.

[35] J. K. Preuss, K. Munch, M. Andersson, I. Denbratt, Comparison of Long-Chain Alcohol Blends, HVO and Diesel on Spray Characteristics, Ignition and Soot Formation, in: SAE Technical Paper Series, 2019.

[36] T. Pachiannan, W. Zhong, T. Xuan, B. Li, Z. He, Q. Wang, X. Yu, Simultaneous study on spray liquid length, ignition and combustion characteristics of diesel and hydrogenated catalytic biodiesel in a constant volume combustion chamber, Renewable Energy 140 (2019) 761–771.

[37] F. Payri, J. V. Pastor, J.-G. Nerva, J. M. Garcia-Oliver, Lift-Off Length and KL Extinction Measurements of Biodiesel and Fischer-Tropsch Fuels under Quasi-Steady Diesel Engine Conditions, SAE International Journal of Engines 4 (2) (2011) 2278–2297.

[38] L. M. Pickett, C. L. Genzale, J. Manin, C.-M. Térmicos, L.-M. Malbec, L. Hermant, Measurement Uncertainty of Liquid Penetration in Evaporating Diesel Sprays, 2011, p. 13.

[39] P.-C. Chen, W.-C. Wang, W. L. Roberts, T. Fang, Spray and atomization of diesel fuel and its alternatives from a single-hole injector using a common rail fuel injection system, Fuel 103 (2013) 850–861.

[40] D. L. Siebers, B. Higgins, Flame Lift-Off on Direct-Injection Diesel Sprays Under Quiescent Conditions, 2001, pp. 2001–01–0530.

[41] S. Kook, L. M. Pickett, Effect of Fuel Volatility and Ignition Quality on Combustion and Soot Formation at Fixed Premixing Conditions, SAE International Journal of Engines 2 (2) (2009) 11–23.

Article IV

David Robert Emberson, Jan Wyndorps, Ahfaz Ahmed, Karl Oskar Pires Bjørgen and Terese Løvås

Detailed Examination of the Combustion of Diesel/Glycerol Emulsions in a Compression Ignition Engine

Submitted to Fuel 24.3.2020

The final article is published in Fuel 2021
https://doi.org/10.1016/j.fuel.2021.120147

Detailed examination of the combustion of diesel/glycerol emulsions in a compression ignition engine

David Robert Emberson[a,*], Jan Wyndorps[b], Ahfaz Ahmed[a], Karl Oskar Pires Bjørgen[a], Terese Løvås[a]

[a] *Department of Energy and Process Engineering, Norwegian University of Science and Technology, Trondheim, Norway*
[b] *Department of Mechanical Engineering, RWTH Aachen University, Aachen, Germany*

Abstract

Diesel engines are one of the most efficient engine technologies, yet their usage is often discouraged due to harmful emissions of nitrogen oxides (NO_x) and particulate matter (PM). In this study, glycerol, which is a by-product from the biodiesel industry, is examined as an oxygenated fuel additive to diesel to advance its combustion applications and also to examine its ability to suppress harmful pollutants, specifically PM. The combustion investigations conducted in this study include engine tests of a diesel/glycerol emulsion to observe the potential to reduce PM emissions. Further, ignition delay times (IDT), flame lift-off lengths (FLOL) and in-flame soot measurements were made inside an optical engine setup, followed by fundamental chemical kinetic investigations, conducted to understand the chemical role of glycerol in exhaust emissions and soot formation. The use of the glycerol as a fuel additive did lead to a reduction in the number of particles emitted above 25 nm but resulted in an extremely large number of particles emitted below 25 nm. Initial analysis of a single sample, using thermogravimetric analysis suggests that the soot emitted from a diesel/glycerol emulsion contained a higher fraction of volatile organic compounds (VOCs) which may account for this increase in smaller particles. The IDTs of the emulsion were slightly longer, the FLOL was slightly longer but the in-flame soot, as characterised by the spatial soot gradient, was reduced at all ambient temperatures. The chemical kinetic investigation revealed that glycerol addition resulted in a reduction in the concentration of soot precursors, eventually reducing the engine out PM emissions.

Keywords: glycerol, diesel-engine, combustion, soot, fuel-additives,

[*] Corresponding author
Email address: david.r.emberson@ntnu.no (David Robert Emberson)

1. Introduction

Particulate matter (PM) emissions from compression ignition (CI) engines pose a considerable environmental and public health problem. While PM emissions from the latest CI equipped vehicles are controlled using diesel particulate filters (DPF), there is concern about increased ultra-fine (below 100 nm) particulate emissions from DPF-equipped vehicles [1]. European pump diesel, meeting the standard EN590, allows for up to 7% biodiesel (often referred to as B7), in the form of a fatty acid methyl ester (FAME) which is an oxygen containing fuel, referred to as an oxygenated fuel. The use of oxygenated fuels in CI engines has been studied extensively and shows a general trend of reducing PM emissions, usually attributed to the oxygen content in the fuel [2]. This effect has been observed in studies examining in-flame soot production [3–5] and engine out emissions [2, 6], though size distribution of the PM in the exhaust is not commonly reported. There is some evidence that the use of an oxygenate may reduce PM mass but lead to a change in the size distribution [7]. If there is an increase in the smaller sizes of PM, which are more harmful to human health, the perceived benefit of PM mass reduction may be negated.

With the increase in the volume of FAME production over the last decade, the production of glycerol (a by-product of FAME production) has also significantly increased and now exceeds demand [8]. Glycerol has several industrial uses but its use as a diesel fuel additive, given its high oxygen content and the advantage of a short closed product cycle, is being considered. Glycerol has been shown to be usable as a combustion fuel directly [9] but in its pure form it is immiscible with diesel and has much higher viscosity. There are studies examining upgraded, lower viscosity and miscible products of glycerol; glycerol carbonate, solketal and triacetin, to use in fuel blends [10–12]. Another methodology is to utilise the glycerol in an emulsion, rather than a blend. Sighu et al. [13] found that CI engine tests running on biodiesel/glycerol emulsions increased the brake specific fuel consumption (BSFC), lowered NO_x and lead to higher CO and unburned hydrocarbon production, postulated to be due to lower reactivity of glycerol as a fuel. Eaton et al. [14] conducted tests with a diesel/glycerol emulsion and observed higher thermal efficiency with lower NO_x and PM in the engine exhaust. McNeal et al. [15] conducted tests with pure glycerol fueling a CI engine and found that a heated air intake at 90°C was required to promote ignition, due to glycerol's high ignition energy. Increased quantities of CO were also emitted compared with diesel, due to incomplete combustion, resulting in a lower combustion efficiency. While there are some indications that diesel/glycerol emulsions may have positive effects, there is a lack of work examining their combustion in a CI engine and their emissions, especially the size distribution of the PM and the in-cylinder soot production.

This study aims to explore: the combustion characteristics of diesel/glycerol emulsions using an instrumented engine fitted with a gaseous emissions analyzer and differential mobility spectrometer (DMS); the in-cylinder soot formation in an optically accessible compression ignition combustion chamber (OACIC); and a chemical kinetic study using LogeResearch to examine the effect of glycerol addition on soot precursors. The work stems from the postulation that glycerol could be an oxygenated fuel additive which reduces soot, is low cost, is environmentally benign, and finds a use for the over-supply of glycerol from biodiesel production.

2. Methods

Diesel/glycerol emulsions were prepared using a surfactant mixture of Span 80 and Tween 80 with a lipophilic-hydrophilic balance of HLB = 6.4, as suggested by Eaton et al. [14]. A 15 w% glycerol emulsion (G15 hereafter) with a surfactant amount of 1.14 w% was produced. An EN590 reference diesel was used for emulsion diesel fuel and also the baseline fuel for comparison, DRef hereafter. The cetane number of the fuels are 60.4 and 52 for DRef and G15 respectively.

The engine used for experimentation is detailed in [7, 16]. The engine gaseous emissions were measured with a Horiba Mexa and the particulate was measured with a Cambustion DMS 500. The engine was operated at a fixed speed of 1800 rpm and 5 loads, specified by the brake torque: 20, 50, 80, 110 and 140 Nm. Fuel injection pressure was maintained at 650 bar with one single injection. The injection timing for each condition and fuel was changed so as to maintain a 50% cumulative heat release (CA50) at 1 CAD ATDC.

Details of the OACIC and measuring techniques are reported in [17]. The OACIC is based on a single cylinder CI engine, with the head redesigned to provide 50 mm of line-of-sight optical access. The OACIC is driven by an electrical motor at a constant speed of 500 rpm. The intake air is compressed by a Roots compressor and heated by an electrical heater. Fuel was injected at 1000 bar, with the start of injection 4 CAD BTDC, which resulted in ignition occurring around TDC.

The thermodynamic conditions in the OACIC were chosen such that the ambient gas density at TDC was

constant for all conditions by varying the inlet air temperature and pressure. A first law model was used to determine the inlet temperature and pressure required to have a varying TDC gas pressure and temperature, with a constant density of ~16.7 kg/m^3. TDC pressures were 38.6, 41.67, 44.63 (bar), TDC temperatures were 808, 872 and 934 (K) for condition 1, 2 and 3 respectively (C1, C2 and C3).

In-flame soot is determined using diffuse back-illuminated extinction imaging (DBIEI). The technique is defined by the Beer-Lambert law, $\tau = \frac{I_t}{I_0} = exp(-KL)$, where τ is the transmittance, I_t is transmitted light intensity, I_0 is incident light intensity, L is the path length through the soot particle cloud and K is the path averaged dimensional extinction coefficient; KL is the optical depth. Using optical and physical properties of soot, the soot volume fraction and the soot mass can be determined; full details of this calculation are included in [17].

The DBIEI optical setup is shown in Fig. 1 and described in more detail, along with the techniques used in [17, 18]. Chemiluminescence from short-lived OH*, was measured using a gated intensifier coupled with a high speed camera.

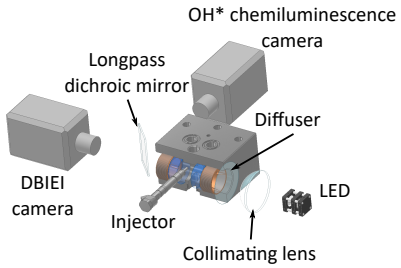

Figure 1: Experimental optical arrangement around the OACIC.

A fundamental approach to elucidate diesel engine combustion, as earlier implemented by Westbrook et al. [19], utilizing homogeneous constant pressure ignition calculations was adopted. Homogeneous constant pressure reactor cases were conducted with both fuels to observe the evolution of soot precursors such as ethene (C2H4), ethyne (C2H2), propene (C3H6) and propyne (PC3H4) during the combustion process and the concentrations of these species long after the ignition event. N-heptane was chosen as the diesel surrogate and for cases with diesel/glycerol emulsions, 15 w% glycerol was added to the n-heptane. The soot precursor concentrations were analyzed for cases with and without glycerol. The approach is intended to simulate the chemical processes leading to ignition, starting from the point where the gas phase reactions start, i.e. after the evaporation and mixing of fuel and air, and then observe the suite of species which promote soot inception. The condition at which the simulations were conducted are representative of TDC conditions in the OACIC flame, i.e 40 bar, 770 K, and equivalence ratio of 4. The mechanism used for the study is generated by merging the glycerol mechanism from Hemings et al. [20] with the n-heptane mechanism from Curran et al. [21].

3. Results and Discussion

3.1. Engine Results

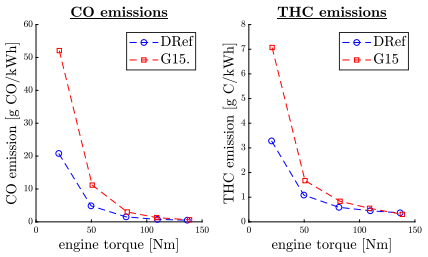

Figure 2: CO and THC emissions from the instrumented engine for diesel and G15.

There was found to be no discernible difference in engine performance when fueled with G15 compared to DRef. The brake thermal efficiency between the fuels were almost identical and there was only a small difference in the NO_x emissions at 20 Nm, otherwise the NO_x concentration was very similar between the fuels. The main difference in engine related measurements between the fuels was the observed CO, THC (see Fig. 2) and the PM emissions. The G15 increased both CO and THC, which matches the behaviour that is observed in previous studies [13, 14]. There was twice as much CO emission at the lowest load, but the ratio between CO emitted between the fuels decreased with increasing load. The increase in these emissions associated with incomplete combustion is attributed to the low reactivity of glycerol, which has a more profound impact at the lower load conditions where temperatures during the combustion were lower.

The PM size distribution, Fig. 3a, includes a very narrow, large peak in the diameter range of 5 to 10 nm for the G15. No such peak was observed with DRef. The height of the G15 peak increases with engine load. Further investigation of the PM was conducted. PM was

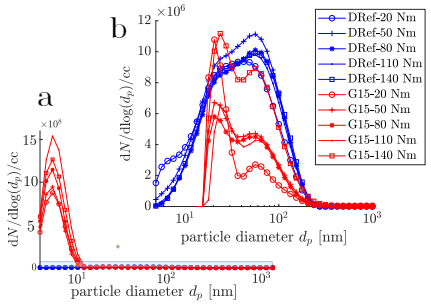

Figure 3: Particle size distribution a) scaled to show peak at small d_p, b) scaled to show accumulation mode peak with all PM from G15 small peak removed.

sampled onto glass fibre filters at the same location in the exhaust as the DMS was sampled with the engine operating at 50 Nm load. For each fuel only one sample was collected. The DRef soot collected on the filter was the usual black colour associated with soot, where as the G15 sample was a mixture of black and brown. This was an early, visual indication that the G15 PM contained a fraction that was not the usual soot. Both samples were subjected to a thermogravimetric analysis.

The samples were initially heated under an inert atmosphere (devolatilisation), followed by a cool-down phase, then heated in an oxidant atmosphere (oxidation). Full details of the procedure are in the work of Emberson et al. [16].During devolatilisation the G15 sample mass decreased faster than the DRef sample, leading to a difference in mass loss during the stationary phase at 550°C. This is indicative of a higher VOC content in the G15 sample. With the oxidant atmosphere, the G15 sample lost mass faster, meaning the soot present oxidised at a faster rate than the DRef soot, suggesting it is more reactive. To compare the samples regarding their VOC, the ratio between the devolatilisation percentage mass loss (100°C to 550°C) and oxidation percentage mass loss was determined resulting in 0.56 and 0.79 for DRef and G15 respectively. The higher value for G15 is interpreted as a larger volatile to soot ratio. It is stressed that this presented result is of a single sample hence reproducibility has not been addressed here. It is hypothesised that the large peak of small diameter particles observed by the DMS (Fig. 3a) for G15 are partly or entirely caused by condensing VOCs. Another hypothesis is that the small particles may be a result of impurities in the glycerol. In the work of Steinmetz et al. [9], crude glycerol was utilised as a boiler fuel with considerable PM emission observed, where the small amount of soluble catalyst left from production was thought to be responsible. The increase in height of the peak, i.e. the increase in the number of the small particles observed with increasing engine load, indicates they increase with increasing fuel mass injected and the higher temperatures present during combustion do not reduce the number. If the particles are not condensing VOCs but small solid soot particles, they are especially harmful due to their penetration ability [22].

By changing the scale of the y-axis (number of particles) of the DMS plot, the particle numbers in the accumulation mode can be compared as shown in Fig. 3b. The accumulation diameter range for G15 was separated from the small peak, with no particles detected between them. This is highly indicative that the peaks are from a different origin. To further simplify Fig. 3b, the small particle peak shown in Fig. 3a have been removed. G15 emits a much smaller number of particles with diameters greater than 25 nm, with a significant drop in the number of particles at around 60 nm. This results in a very different size profile of the accumulation mode G15 compared to the DRef. The reduction in 60 nm PM is largest at low engine loads. The number of particles with diameters greater than 25 nm is reduced by 61% at 20 Nm, by 56% at 80 Nm, and by 11% at 140 Nm. The DMS results, the soot filters and the TGA results show that the G15 has drastically changed the exhaust out PM and soot, in quantity, character and size profile. This is most definitely a result of the oxygen content, the low reactivity and the physical fluid properties of the glycerol in the G15.

Brake specific CO and PM emissions are highest at the lowest load condition and decrease with increasing engine torque. Comparing the emissions for each condition, the diesel/glycerol emulsion yields a reduction in PM while increasing CO emissions. While the $PM_{dp>25nm}$ reduction is most effective at low load conditions, the CO increase is likewise. This trade-off is thought to be due to glycerols low reactivity. As the engine torque is increased and temperatures during combustion increase, the lower reactivity of the glycerol has less of an impact on CO formation. The higher temperatures during the higher torque conditions will also lead to higher rates of soot oxidation in the combustion chamber. If glycerol is reducing soot through its oxygen content, this would be expected to be most evident at the lowest loads where later cycle soot oxidation will be lower. The difference in the size distribution in the accumulation mode with glycerol present suggests there is some fundamental change to the soot formation process

when the glycerol is present, not just an overall reduction in the soot produced. The increase of CO emissions of around 20% at the higher load conditions may be regarded as a minor concern as the absolute value of CO concentrations is very low. In contrast, the increase in CO concentration at the low load condition is critical as the CO concentration is much higher, hence the large $PM_{dp>25nm}$ reduction has to be put into perspective to the significant CO increase.

3.2. OACIC Results

The ignition delay time (IDT) in the OACIC was determined from the time between the start of injection (SOI) and initial OH* emission. The SOI was determined from DBIEI to eliminate trigger and hydraulic delay in the injection system. Figure 4 shows the ignition delay time for both fuels. The error bars represent the 95% confidence interval of the true mean. In all the cases the ignition delay of G15 was longer than DRef and this difference did not decrease with rising ambient temperature.

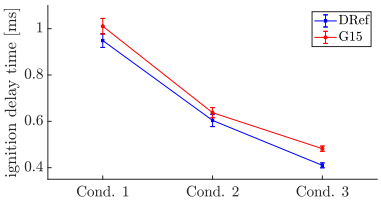

Figure 4: Ignition delay times measured in the OACIC from OH* for DRef and G15 at each condition.

While the ignition delay indicates the time available for the fuel and air to mix prior to combustion during the premixed combustion phase; the flame lift-off length (FLOL) is an indicator of fuel and air mixing during the mixing-controlled combustion phase. The instantaneous FLOL has been determined from the integrated OH* intensity in each pixel column. The integrated intensity is calculated in an area close to the centre-line as represented by the two white lines in Fig. 5.

Figure 6 shows the temporal FLOL averaged over all injections with the coloured shade indicating the 95% confidence interval. After ignition and the premixed period, the FLOL stabilises at a constant position before the end of the injection period. While fuel ignites downstream of the stable position for Condition 1, ignition is slightly upstream for Condition 3. Increasing ambient temperature results in a decrease of the FLOL for both fuels, with differences in FLOL between the fuels becoming very small. Based on this FLOL interpretation,

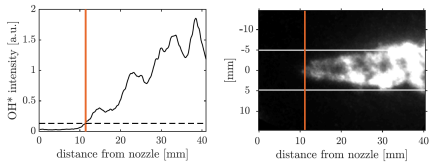

Figure 5: Example determination of the FLOL (red line) using integrated OH* intensity (solid black line) passing a threshold value (dashed line), example OH* image on the right side.

the quasi-steady period is identified, beginning at 2.5 ms and ending at 3.8 ms after SOI. Compared to the DRef, the G15 has a 2.5 mm longer (very small difference) FLOL at the low temperature condition; at the high temperature condition both fuels show a very similar FLOL. Pickett et al. [23] showed that the ignition quality of a fuel affects FLOL. In the case of fuels with a big difference in cetane number, fuels with shorter IDT generally produced shorter FLOL. The shorter IDT of the DRef does trend with the shorter FLOL but differences observed between the DRef and the G15 is very small, while the difference in cetane number is around 8.4. Fuels with a small difference in cetane number and/or containing oxygen do not necessarily show the same FLOL and IDT trend, as shown in [5] and [3], with the difference depending on fuel properties resulting from the components of fuel blends, mixture ratios or injection velocities.

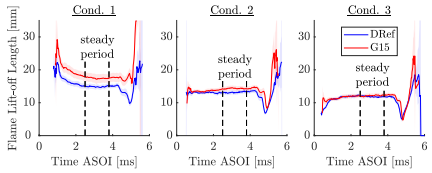

Figure 6: FLOL with time ASOI for each fuel at each condition with the quasi-steady period bracketed by the dashed black lines.

Soot behaviour is assessed as a spatial soot gradient (SSG) during the quasi-steady combustion period at a fixed distance from the FLOL position. A similar technique was previously used by the authors in [17], with the single value metric, the SSG, defined as the maximum increase of soot mass between the FLOL and 19 mm downstream of the FLOL. By relating the SSG to the FLOL instead of the injector nozzle, the variation of the flame location is taken into account. To determine the SSG, KL is integrated in each pixel column and plotted over the distance from the injector nozzle. Figure 7 illustrates an example case at Condition 2, with

the average over all 30 injections of the cross-sectional integrated KL value as a solid line, the shaded area representing the 95% confidence interval for both fuels, the FLOL marked with a star and the location of 19 mm after the FLOL indicated by the vertical line. The initial increase in KL is the light extinction caused by the spray liquid fuel core, which is increasing in the beginning because of the divergence of the spray and decreasing further downstream due to fuel evaporation.

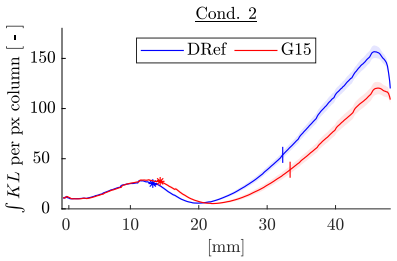

Figure 7: Integrated KL (solid line), saturated KL values per column (dashed line) during the quasi-steady phase for condition 2, the star represents the FLOL and the vertical line shows 19 mm after FLOL.

The increase after the minimum indicates the increasing soot concentration with increasing distance from the injector nozzle. The drop of the cross-sectional integrated KL at the end is caused by the circular chamber wall reducing the observable area. Comparing the two fuels, the G15 shows an increased liquid penetration length, with the effect most significant at Condition 1. With rising temperatures, soot is observed closer to the injector and the spatial gradient increases for both fuels. For all conditions the DRef had the biggest SSG. Figure 8 shows the averaged KL images from the quasi-steady period used to determine the SSG.

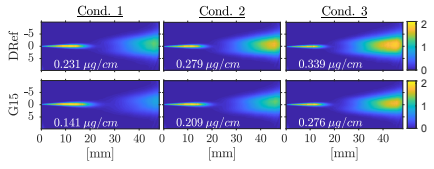

Figure 8: Averaged KL plots during the quasi-steady period with the bottom value indicating the spatial soot gradient.

Figure 9 shows SSG with FLOL. The bars represent the 95% confidence interval of each quantity. A more significant difference between the G15 and the DRef is observed. The G15 has an increased FLOL and a significantly lower SSG. The increase in SSG with increasing temperature at SOI is consistent with previous findings [3]. As the temperature at SOI increases, FLOL decreases and soot (SSG) increases but while the difference in FLOL between the fuels becomes smaller with increasing temperature, the difference between the SSG remains quite consistent, so even at the higher temperature condition, when the FLOL for the two fuels is similar, the G15 SSG is smaller. Cond.2- G15 and Cond.1-DRef have a similar FLOL, and similar SSG (repeated for the following conditions). As Cond.2-G15 is higher temperature than Cond1.-DRef, it would be expected that it would have a higher SSG, the fact that it does not (but the FLOL are similar) is due to the oxygen content.

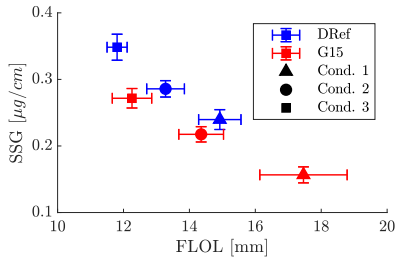

Figure 9: Spatial soot gradient plotted over flame lift-off length; the bars represent the 95% confidence interval.

3.3. Chemical Kinetic Results

Ignition calculations were performed at constant pressure for n-heptane and blend of n-heptane and glycerol, and concentration of species CO, CO2, C2H2, C2H4, PC3H4, C3H6 were compared for the two cases. The comparison of CO, CO2 and temperature are presented in Fig. 10a. Both the mixtures exhibit onset of ignition at the same time (0.7 ms) and attain roughly the same final temperature. Since the simulations were at such rich conditions the burnt gases' final temperature is much below the adiabatic flame temperature. The concentrations of CO and CO2 emanating from these cases are shown in Fig. 10a, where the concentration of CO emission is higher in the cases with glycerol present in the fuel, which is consistent with experimental observation shown in Fig. 2. The higher presence of CO indicates towards incomplete combustion, due to lower reactivity of the glycerol blend, due to lower cetane number of glycerol.

The concentration of soot precursor species are also observed during the ignition process and is presented in Fig. 10b. The species presented in Fig. 10b are ethene (C2H4), ethyne (C2H2), propyne (PC3H4) and propene (C3H6). These species are shown to be critical to PAH

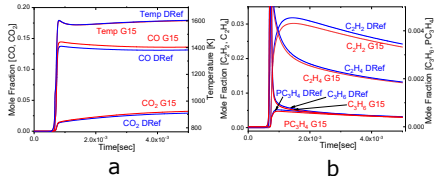

Figure 10: Results from chemical kinetic simulations a) CO and CO2 concentrations with time, b) soot precursor concentrations with time.

growth and hence contribute significantly towards soot inception. Among these species ethyne is known to be highest contributor towards soot growth [24, 25]. Figure 10b shows that the species' evolution start with the onset of ignition and peak shortly after the ignition event. The concentration of these species then reduce slowly with time. In this study we have taken the concentrations at the end of the simulation time to be final concentration of these precursors. The results of the simulations indicate that the reduction in concentration of C2H2 and C2H4 is attained due to glycerol addition to diesel, however the concentration of C3H6 and PC3H4 were not significantly affected. Acetylene is known to be the most significant growth species for soot chemistry and reduction in its concentration with glycerol addition could be a possible explanation for reduction in soot formation.

As earlier explained by Westbrook et al. [19], the oxygenated additives reduce soot by introducing species containing carbon atoms bonded to the oxygen atom into the system, which do not contribute to PAH chemistry; secondly, they also introduce additional oxygen atoms, which increase the oxidation of the species pool, including the soot precursors.

4. Summary and Conclusions

This study explores the combustion of diesel and a diesel/glycerol emulsion in various combustion systems with multiple diagnostic techniques. Initial testing took place with an instrumented CI engine. The PM/soot was measured and analyzed using a DMS 500 and TGA to gather understanding of the size distribution with glycerol addition. The fuels were also tested in an optically accessible compression ignition combustion chamber to study in-flame soot formation, FLOL and ignition delay. To develop further understanding of the combustion kinetics of diesel/glycerol emulsions, a fundamental chemical kinetic study of soot precursor formation was conducted. The collective conclusions from these studies include: 1) Due to its poor ignition character and low reactivity (longer IDT), glycerol addition resulted in higher CO emissions from the engine at low load conditions suggesting its use in an engine would require intake air treatment or higher compression ratios. 2) Glycerol as a fuel additive is found to have a beneficial effect on PM emissions with diameters greater than 25 nm but features a significant increase in particles smaller than 25 nm in diameter. Initial TGA results indicated a higher VOC fraction for the glycerol soot. 3) An inverse correlation between CO and $PM_{dp>25nm}$ is observed in the engine. 4) Optically observed ignition delay time is slightly longer with the addition of glycerol, FLOL was longer and in-flame soot as identified by the spatial soot gradient was reduced. FLOL between the two fuels become similar with increasing ambient temperatures, while soot remained lower for the glycerol containing fuel. 5) Glycerol addition did reduce soot formation during combustion, primarily due to presence of carbon atoms bonded to oxygen in the molecule, which do not take part in soot chemistry. The kinetic simulations also displayed some reduction in ethyne and propyne concentrations, which is known to be the most important soot growth species.

5. Acknowledgements

The research work reported in this work was supported by Bio4Fuels (FME) of the Research Council of Norway, Project Number 257622.

References

[1] P. K. Saha, A. Khlystov, M. G. Snyder, A. P. Grieshop, Characterization of air pollutant concentrations, fleet emission factors, and dispersion near a north carolina interstate freeway across two seasons, Atmos. Env. 177 (2018) 143 – 153.

[2] C. Guan, C. Cheung, X. Li, Z. Huang, Effects of oxygenated fuels on the particle-phase compounds emitted from a diesel engine, Atmos. Pollution Res. 8 (2) (2017) 209 – 220.

[3] J. Manin, S. Skeen, L. Pickett, E. Kurtz, J. E. Anderson, Effects of oxygenated fuels on combustion and soot formation/oxidation processes, SAE Tech. Paper (2014-01-2657).

[4] C. J. Mueller, W. J. Pitz, L. M. Pickett, G. C. Martin, D. L. Siebers, C. K. Westbrook, Effects of oxygenates on soot processes in di diesel engines: experiments and numerical simulations, SAE Transactions (2003) 964–982.

[5] W. Park, S. Park, R. D. Reitz, E. Kurtz, The effect of oxygenated fuel properties on diesel spray combustion and soot formation, Combust. Flame 180 (2017) 276 – 283.

[6] J. Song, K. Cheenkachorn, J. Wang, J. Perez, A. L. Boehman, P. J. Young, F. J. Waller, Effect of oxygenated fuel on combustion and emissions in a light-duty turbo diesel engine, Energy Fuels 16 (2) (2002) 294–301.

[7] D. R. Emberson, K. O. Bjorgen, T. Lovas, Arctic biodiesel performance and pm number emissions, COMODIA 9 (2017) 205.

[8] C. R. Coronado, J. A. Carvalho, C. A. Quispe, C. R. Sotomonte, Ecological efficiency in glycerol combustion, App. Thermal Eng. 63 (1) (2014) 97 – 104.

[9] S. A. Steinmetz, J. S. Herrington, C. K. Winterrowd, W. L. Roberts, J. O. Wendt, W. P. Linak, Crude glycerol combustion: Particulate, acrolein, and other volatile organic emissions, Proc. Combust. Inst. 34 (2) (2013) 2749 – 2757.

[10] J. A. Melero, G. Vicente, G. Morales, M. Paniagua, J. Bustamante, Oxygenated compounds derived from glycerol for biodiesel formulation: Influence on en 14214 quality parameters, Fuel 89 (8) (2010) 2011 – 2018.

[11] A. Cornejo, I. Barrio, M. Campoy, J. Lzaro, B. Navarrete, Oxygenated fuel additives from glycerol valorization. main production pathways and effects on fuel properties and engine performance: A critical review, Ren. and Sust. Energy Rev. 79 (2017) 1400 – 1413.

[12] M. Szoeri, B. R. Giri, Z. Wang, A. E. Dawood, B. Viskolcz, A. Farooq, Glycerol carbonate as a fuel additive for a sustainable future, Sust. Energy Fuels 2 (2018) 2171–2178.

[13] M. S. Sidhu, M. M. Roy, W. Wang, Glycerine emulsions of diesel-biodiesel blends and their performance and emissions in a diesel engine, App. Energy 230 (2018) 148–159.

[14] S. J. Eaton, G. N. Harakas, R. W. Kimball, J. A. Smith, K. A. Pilot, M. T. Kuflik, J. M. Bullard, Formulation and combustion of glycerol–diesel fuel emulsions, Energy Fuels 28 (6) (2014) 3940–3947.

[15] J. McNeil, P. Day, F. Sirovski, Glycerine from biodiesel: The perfect diesel fuel, Proc. Safety and Env. Prot. 90 (3) (2012) 180 – 188.

[16] D. R. Emberson, B. Rohani, L. Wang, S. Ragnhild, T. Lovas, On soot sampling: Considerations when sampling for tem imaging and differential mobility spectrometer, SAE Tech. Paper (2019-24-0159).

[17] K. O. Bjorgen, D. R. Emberson, T. Lovas, Optical measurements of in-flame soot in compression-ignited methyl ester flames, Energy Fuels 33 (8) (2019) 7886–7900.

[18] K. O. Bjorgen, D. R. Emberson, T. Lovas, Diffuse Back-Illuminated Extinction Imaging of Soot: Effects of Beam Steering and Flame Luminosity, SAE Tech. Paper (2019-01-0011).

[19] C. K. Westbrook, W. J. Pitz, H. J. Curran, Chemical kinetic modeling study of the effects of oxygenated hydrocarbons on soot emissions from diesel engines, J. Phys. Chem. A 110 (21) (2006) 6912–6922.

[20] E. B. Hemings, C. Cavallotti, A. Cuoci, T. Faravelli, E. Ranzi, A detailed kinetic study of pyrolysis and oxidation of glycerol (propane-1,2,3-triol), Combust. Sci. Tech. 184 (7-8) (2012) 1164–1178.

[21] H. Curran, P. Gaffuri, W. Pitz, C. Westbrook, A comprehensive modeling study of n-heptane oxidation, Combust. Flame 114 (1) (1998) 149 – 177.

[22] S. Steiner, C. Bisig, A. Petri-Fink, B. Rothen-Rutishauser, Diesel exhaust: current knowledge of adverse effects and underlying cellular mechanisms., Archives of toxicology 90 (2016) 1541–53.

[23] L. M. Pickett, D. L. Siebers, C. A. Idicheria, Relationship between ignition processes and the lift-off length of diesel fuel jets, SAE Tech. Paper (2005-01-3843).

[24] B. Haynes, H. Wagner, Soot formation, Prog. in Energy and Comb. Sci 7 (4) (1981) 229 – 273.

[25] H. Wagner, Soot formation in combustion, Symp. (Int.) Combust. 17 (1) (1979) 3 – 19.

Doctoral theses at NTNU, 2020:117

Karl Oskar Pires Bjørgen

Optical Study of Soot Characteristics of Biofuel Spray Combustion

Doctoral Thesis

Karl Oskar Pires Bjørgen

ISBN 978-82-326-4582-4 (printed version)
ISBN 978-82-326-4583-1 (electronic version)
ISSN 1503-8181

NTNU
Norwegian University of
Science and Technology
Department of Energy and Process Engineering
Faculty of Engineering
Science and Technology
Norwegian University of
NTNU

Doctoral theses at NTNU, 2020:117

NTNU
Norwegian University of
Science and Technology